IDŐJÁRÁS

QUARTERLY JOURNAL OF THE HUNGAROMET
HUNGARIAN METEOROLOGICAL SERVICE

CONTENTS

VOL. 128 * NO. 3 * JULY – SEPTEMBER 2024

IDŐJÁRÁS

Quarterly Journal of the HungaroMet Hungarian Meteorological Service

Editorial Office: Kitaibel P.u. 1, H-1024 Budapest, Hungary
P.O. Box 38, H-1525 Budapest, Hungary
E-mail: journal.idojaras@met.hu

Indexed and abstracted in Science Citation Index Expanded™ and Journal Citation Reports/Science Edition
Covered in the abstract and citation database SCOPUS®
Included in EBSCO's database

Subscription by mail:
IDŐJÁRÁS, P.O. Box 38, H-1525 Budapest, Hungary
E-mail: journal.idojaras@met.hu

DOI:10.28974/idojaras.2024.3.1

IDŐJÁRÁS

Quarterly Journal of the HungaroMet Hungarian Meteorological Service
Vol. 128, No. 3, July – September, 2024, pp. 287–308

Standardized precipitation index analysis and drought frequency tendencies in lower eastern counties of Kenya

Peter K. Musyimi[1,2,*], **Balázs Székely**[1], **Arun Gandhi**,[3] and **Tamás Weidinger**[3]

[1] *ELTE Eötvös Loránd University,*
Faculty of Sciences Institute of Geography and Earth Sciences,
Department of Geophysics and Space Science
Budapest, Pázmány Péter sétány 1/C, Hungary

[2]*Karatina University, School of Education and Social Sciences,*
Department of Humanities and Languages
P.O.BOX 1957-10101, Karatina, Kenya

[3] *ELTE Eötvös Loránd University,*
Faculty of Sciences Institute of Geography and Earth Sciences,
Department of Meteorology, Budapest, Pázmány Péter prom 1/A, Hungary

** Corresponding Author E-mail: musyimipeter@student.elte.hu*

(Manuscript received in final form October 9, 2023)

Abstract— The standardized precipitation index (SPI) is a fundamental indicator of meteorological, hydrological, and agricultural droughts in the world. This study aims to evaluate different timescales, 3 months (SPI-3), 6 months (SPI-6), 9 months (SPI-9), and 12 months (SPI-12) indices from meteorological data in quantifying drought characterization in lower eastern counties of Kenya from 1990 to 2018 for observed data and from 1986 to 2018 for Climatic Research Unit Time Series (CRU) data. Precipitation in-situ data (annual) and high-resolution (0.5 × 0.5 degree grid) monthly-scale precipitation data were sought from Kenya Meteorological Department and CRU TS, respectively. Z-Score (SPI) was computed for each year (in-situ data) and month (CRU TS data) using the SPI algorithm, expressed as the departure from the mean in standard deviation units. Quality control of CRU TS data was done by checking outlier values and comparing the data with precipitation data obtained from the meteorological department as well as ERA5 reanalysis data. Results showed that extreme to mild drought was experienced across the Kenyan counties for both annual in-situ and monthly gridded data. Machakos county experienced a year of extreme drought, while Makueni and Taita-Taveta have had 2 and 4 years of severe droughts, respectively. The monthly SPI indices of 3, 6, 9, and 12 months showed a remarkably consistent behavioral pattern detecting extreme droughts across the counties. Considering the uncertainties, unpredictability, and shifting of the long and short rainy seasons in Kenya, results were obtained related to dry and wet episodes and to their relationship with agricultural production as well as water availability and environmental management.

Key-words: drought, Kenya, monthly scale, precipitation, SPI, CRU TS, ERA5.

1. Introduction

Drought is a complex, dynamic climatic extreme brought about by the departure of monthly to annual long-term rainfall averages (*Naumann et al*., 2018; *AghaKouchak et al*., 2021). It threatens a wide range of sectors from agriculture, transport, industrialization, and water resources, among others. It varies in its inception, intensity, duration, and frequency (*Masih et al.,* 2014; *Vicente-Serrano et al.,* 2014; *Azmi et al.,* 2016; *Cammalleri et al*., 2017). Droughts have become a recurrent global phenomenon (*Sheffield* and *Wood*, 2011) with expected increased trends coupled with aridity. It has threatened humanity's livelihood, for instance, causing deaths, poor crop production, food insecurity, exacerbating famine in various regions, fueling malnutrition, health-related issues, and rural migration (*Masih et al*., 2014; *Dalu et al*., 2018; *Ault*, 2020).

Africa has experienced prolonged, widespread droughts of different magnitudes of severity, for instance, in the Sahel region in the 1970s and 1980s. The continent will be affected more severely by drought than other global regions (*Yanda* and *Mubaya*, 2011; *Niang et al*., 2014; *IPCC*, 2021). For a period of over 100 years (1900–2013), 291 drought events were reported in Africa which led to the death of approximately 850,000 people, affected approximately 362.5 million people, and resulted in a continental economic loss of an estimated USD 2 billion (*Masih et al*., 2014). On a regional scale, in East Africa, the severe drought of 2016 exposed 16 million inhabitants across Somalia, Ethiopia, and Kenya to hunger, food insecurity, and water scarcity (*Nicholson,* 2016; *Von Grebmer et al*., 2016; *Yang* and *Huntingford*, 2018; *Kalisa et al*., 2020). These droughts vary depending on anomalies in the amount of precipitation received in a region. In addition, a wide meteorological phenomena range influences its occurrence and variability in East Africa. They include monsoons, the Inter-Tropical Convergence Zone (ITCZ), subtropical anticyclones, African jet streams, easterly/westerly wave perturbations, global scale systems like the El Niño /Southern Oscillation (ENSO), and regional systems in East Africa (*Alusa* and *Mushi*, 1974; *Ogallo* and *Anyamba*, 1983). These droughts have threatened the livelihood of approximately 1.4 billion people for the last two decades and led to approximately 25,000 deaths in East Africa (*CRED*, 2020).

In Kenya, drought has remained a dominant devastating extreme climate phenomenon and recurrent hazard affecting the country's population livelihoods (*Opiyo et al*., 2015; *Musyimi et al*., 2018). This has a wide range of severe effects specifically in arid and semi-arid lands (ASALs). It further causes water scarcity due to hydrological imbalances, a situation exacerbated by extreme temperatures and evapotranspiration (*Shilenje et al*., 2019). Previous studies have projected that by the year 2100, climate change is expected to increase temperatures in Kenya by approximately a maximum of 4 °C and will lead to rainfall variability by about 20% (*Awuor et al*., 2008; *Kabubo-Mariara*, 2008; *Downing, et al*., 2009; *Ajuang et. al.*, 2016; *Maingey et al*., 2020) having negative impact on agricultural

production, water accessibility among households in volatile ecosystems in these regions. The studies above have outlined the global, continental, and regional status and the effects of droughts. For present and future preparedness, adaptation, and mitigation of drought characterization in arid regions of Kenya is fundamental. Even though many previous studies have been carried out in Kenyan counties, few studies have compared drought tendencies among counties based on annual and different SPI scales. Thus, the present study focused on analyzing SPI as well as spatio-temporal variability of annual rainfall and drought tendencies in arid and semi-arid lands and counties of Kenya. This was done by examining the annual in-situ precipitation data as well as CRU data across lower eastern counties. This is because most uncertainties in drought characterization are driven by precipitation variation rather than temperature variation (*Borona et al*., 2021). The study provides the basis for further research on other counties, since 89% of Kenya's total land mass (29 out of 47 counties) are classified as arid and semi-arid (*Akuja* and *Kandagor*, 2019) and characterized by recurring drought events.

Ayugi et al. (2018) examined factors influencing March-May rainfall variability using monthly observed and CRU TS reanalysis rainfall datasets for the period 1971–2010. *Mutsotso et al*. (2018) investigated CRU temperature data together with Climate Hazards Group InfraRed Precipitation with Station data (CHIRPS), which is a rainfall data set from 50°S to 50°N ranging from 1981 to near-present, incorporating climatology, CHPclim, 0.05° resolution satellite imagery, and in-situ station data to create gridded rainfall time series for trend analysis and seasonal drought monitoring. *Funk et al*. (2014) merged a product composed of five satellite-based and ground weather station data to compute drought characterization. CRU TS data is gridded and based on angular distance weighting of ground weather station data from national meteorological services around the world (*Harris et al*., 2020). *Sahoo et al.* (2015) applied the Tropical Rainfall Measuring Mission (TRMM) and CRU to characterize meteorological droughts at a large scale and established that CRU data indicated severe drought for SPI-6 for the year 2006. *Assamnew* and *Mengistu* (2022) also applied CRU-TS as a reference observed data when they assess ERA5 performance in East Africa with European Center for Medium-Range Weather Forecasting (ECMWF). This indicates the wide use of various climate datasets for various climatological investigations in Kenya and East Africa at large. There has been growing interest in the recent developments of drought events in Kenyan counties. Kenya has had extreme drought events, whose spatial and temporal variability has not been understood, especially at regional and sub-regional scales. None of the studies compared various annual drought severity frequencies on a monthly scale and annual scale using different datasets hence this study. Therefore, besides examining the uncertainty of drought characterization using different datasets, our investigations fill the gap of differences experienced from various drought severity frequencies on monthly and annual scales for different datasets, which are imperative for long-term and short-term agricultural activities and associated effects.

2. Material and methods

2.1. Climate characterisation within the selected counties

The investigated area was the lower part of Eastern Kenya. It comprises Machakos, Taita-Taveta, and Makueni counties (*Fig. 1*). Machakos county falls under arid and semi-arid climates. It has an elevation range from 400 m to 2100 m above sea level (*Huho*, 2017). Taita-Taveta county is semi-humid to semi-arid with a mean annual rainfall of 650 mm and average temperature of 23 °C. Makueni county is arid and semi-arid, characterized by severe water scarcity, food insecurity, and low adaptive capacity and resilience to climate change and variability (*Muema et al*., 2018). Rainfall ranges from 800 mm to 1200 mm, while the low-lying areas receive a range of 150 mm to 650 mm per year. The data set used by this study comprised of in-situ annual precipitation amount for a period of 29 years (1990–2018) and monthly precipitation data for the three counties from the Climatic Research Unit Time-series (CRU TS), CRU TS 3.25 datasets for the period 1986–2016 (31 years) (*Harris* and *Jones*, 2017). It was sought from Machakos, Voi, and Makindu meteorological stations of the said counties, respectively. The CRU TS dataset was quality controlled by checking various annual precipitation amounts and comparing the values with observed measured datasets from the weather stations obtained from the Kenya Meteorological Department.

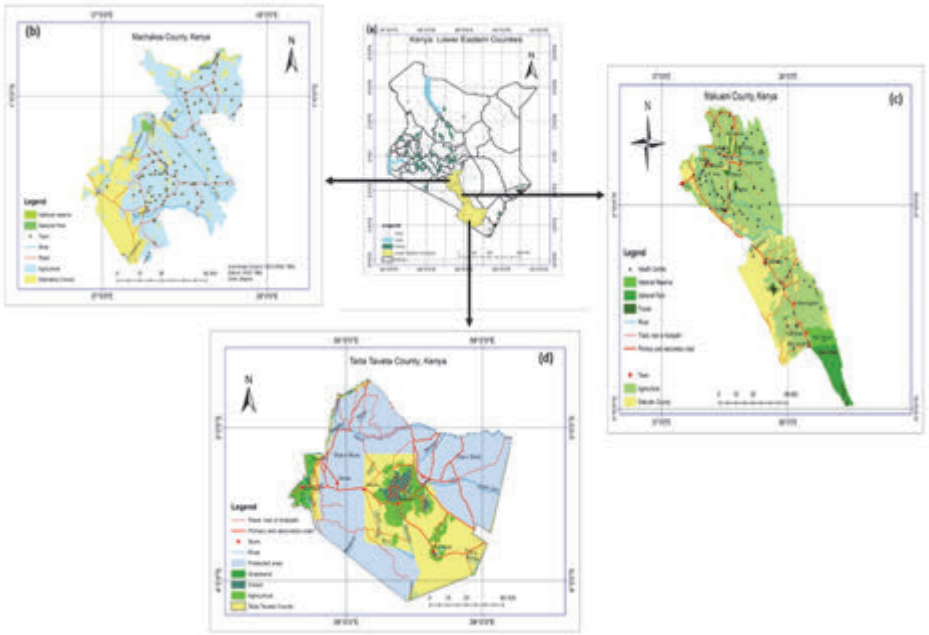

Fig. 1. Map of Kenya with the lower eastern counties under study (a), Machakos County (b), Makueni County (c), Taita-Taveta county (d).

2.2. Quality control, normality, and significance tests of the datasets

Quality control of CRU TS data (*Harris et al*., 2020) and ERA5 reanalysis data (climate reanalysis produced by ECMWF, *Hersbach et al*. (2020) was done by checking and comparing their consistency with observed in-situ data from the meteorological stations operated in Kenya. This is because most weather station time series data is quality controlled by the Kenya Meteorological Department. Few outlier (<5%) cases observed in the CRU TS dataset were harmonized based on the observed value from the meteorological station. This was to exclude their abnormality and the impacts associated with it. The quality control of gridded data differed from that of in-situ data, and therefore, CRU TS datasets underwent extensive manual quality control measures for consistency. We repeated the quality control on the ERA5 reanalysis dataset, even though there were no outlier values observed from the three stations, and compared the normality with other datasets using Shapiro and Anderson tests (*Ghasemi* and *Zahediasl,* 2012). Similar comparisons were done by *Vanella et al.* (2022) in Italy between ERA5 and ground-based agrometeorological observations and demonstrated the potential of using ERA5 reanalysis data. Further, the precipitation time series (*Fig. 2*) of the data sets were done for comparison purposes and depicted similarity in the patterns throughout the period for the three stations with an insignificant variation. The year 2005 was a drought year in Kenya as shown in Figure 2. The peak of rainfall amount in the year 2006 was as a result of 2006/2007 El Niño events which occured through out Kenya evethough low amount of rain was recieved in Makindu meteorological station as compared to ther other stations. Machakos weather station had annual mean precipitation of 679 ±198 mm, 823 ±169 mm, and 674 ±175 mm for in-situ, ERA5, and CRU TS gridded data, respectively, while Voi weather station showed annual precipitation mean of 568 ±190 mm, 590 ±140 mm, 742 ±192 mm for in-situ, ERA5, and CRU TS gridded data, respectively. Makindu weather station recorded mean annual precipitation of 521 ±192 mm, 631±162 mm, and 654 ±177 mm for in-situ, ERA5, and CRU TS gridded data, respectively. ERA5 and reanalysis datasets were obtained freely from the Climate Change Service Copernicus platform (https://cds.climate.copernicus.eu/cdsapp#!/search?type=dataset). In addition to the quality control, we carried out a normality test using Shapiro and Anderson tests of each dataset, which demonstrated that the datasets from the three stations were normal, since all the p-values from the three datasets and the three stations were $p>0.05$. An analysis of variance (ANOVA) on these datasets again yielded significant variation between datasets, for example in the Machakos weather station the F-value (variation between means/variation within the data sets) was 6.24 and the p-value was 0.003. In the Makindu weather station, the F-value was 4.56 with and p-value of 0.013 while the Voi weather station's F value was 8.15 and the p-value was 0.006. All the three p-values from the three datasets and three stations were less than 0.05, hence we concluded that there were statistical differences between the means of the three datasets.

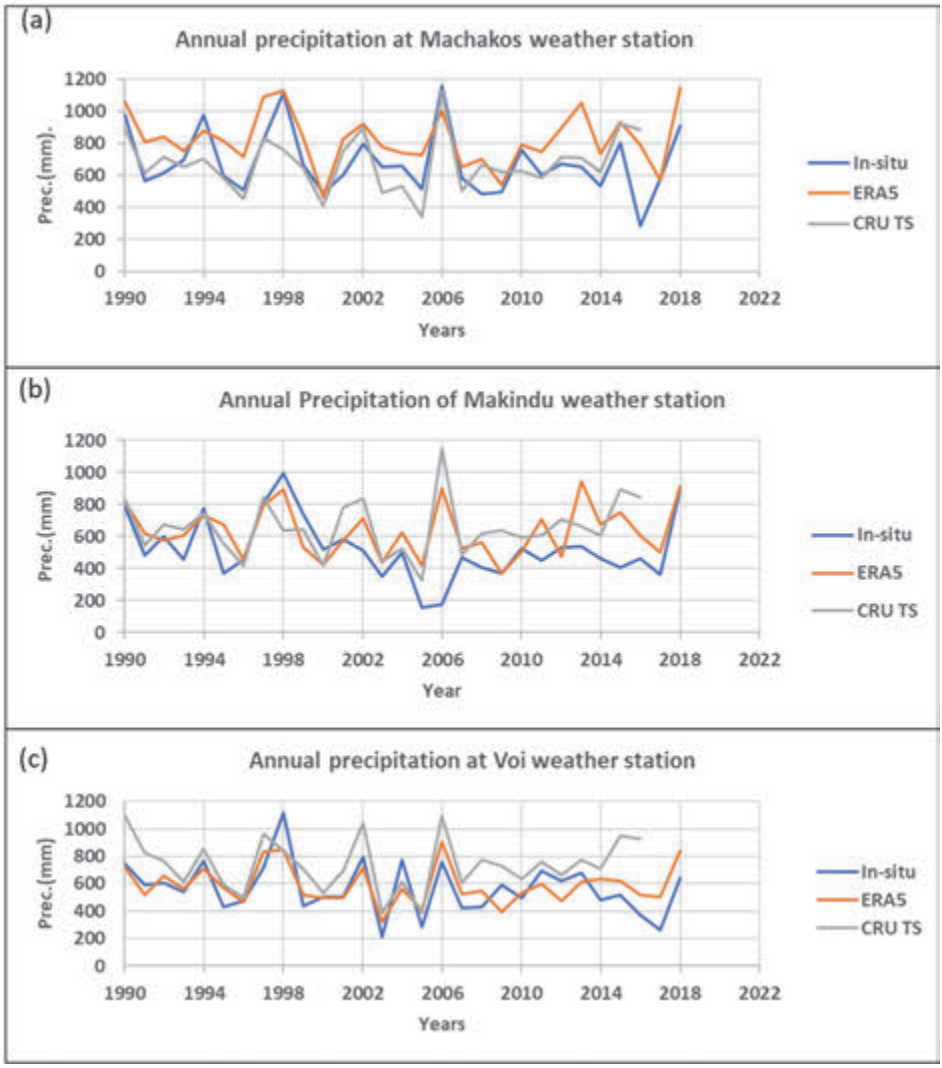

Fig. 2. Precipitation time series of in-situ, ERA5, CRU TS for (a) Machakos weather station, (b) Makindu weather station, (c) Voi weather station.

3. Methodology

The climatic parameter used for the study was the annual rainfall amount. The first set of data was obtained from three meteorological stations namely Machakos, Voi, and Makindu from three counties namely Machakos, Taita-Taveta, and Makueni, respectively. The three sets of observed rainfall data were for a period of 29 years (1990–2018), as it was the available data at the time of

acquisition from the Kenya Meteorological Department. The data was used to compute annual distribution and annual variations among the counties for the different years. Further, a time series analysis was done to show the trend among different years in the counties. Ranking of the rainfall data per station was done and a serialised rank number (r) ranging from 1 to n (number of observations) given (*WMO*,1983). Rainfall data were used to compute annual totals and variations among the stations as well as probability exceedance (Eq.(1)) (*WMO,* 1983; *Raes*, 2004; *Huho,* 2017) and return period (Eq.(2)) (*Weibull*, 1939; *Olatunde* and *Adejoh*, 2017; *Kalisa et al*., 2020). The coefficient of variation (*CV*) (Eq.(3)) (*Huho*, 2017) was also applied to establish variations in annual rainfall among years and counties. It is obtained by dividing the standard deviation by the long-term mean, and it is expressed as a percentage. The second source of data was monthly-scale precipitation data for the three counties from the CRU TS, CRU TS 3.25 datasets for the period 1986–2016 (31 years) *(Harris et al*., 2020; https://catalogue.ceda.ac.uk/uuid/c311c7948e8a47b299f8f9c7ae6cb9af) which has a high spatial resolution of 0.5° and covers the period 1901−2016. Our study used 31 years to compute drought characterization as the time period recommended by *WMO* (2012) and deemed applicable in comparison with investigation from in-situ available data (1990–2018). In the present study, computation of *SPI* indices on monthly scales from the three counties was done using codes developed from the R program which was a suitable statistical analysis.

$$P_x = \frac{r-0.44}{n+0.12} * 100\ , \tag{1}$$

where P_x is the probability exceedance, n is the number of years, while r is a rank.

$$T = \frac{n+1}{m}, \tag{2}$$

where T refers to the return period in years, n is the total number of the values, and m is the rank value assigned to rainfall amount in an order from 1 to n (number of observation) (*Olatunde and Adejoh*, 2017).

$$CV = \frac{\sigma}{\bar{x}} * 100\ , \tag{3}$$

where *CV* is the coefficient of Variation, $\overline{x}$ and σ refer to the mean and standard deviation of precipitation, respectively.

$$SPI = \frac{x-\bar{x}}{\sigma}, \tag{4}$$

where x is precipitation for the period under study.

An *SPI* formula (Eq.(4)) for drought computation based on the precipitation probability was developed by *McKee et al.* (1993) and *Edwards* and *McKee* (1997) to study departures of precipitation from the long-term mean. It has received a wide range of applications globally (*Vicente-Serrano*, 2006; *Vicente-Serrano et al.*, 2010, 2012; *Guenang* and *Kamga*, 2014; *Karanja et al.,* 2017). It was used to analyze and characterize droughts of various severities in the study area. This *SPI* (*Tables 1* and *2*) drought index has been widely used and recommended over recent years to characterize and compare droughts spatio-temporarily (*Kumar et al.*, 2010; *Vicente-Serrano et al.,* 2010; *Karanja et al.,* 2017). From *Tables 1* and *2*, dry spells and meteorological drought were considered to have occurred when the *SPI* value was negative, and their absence was indicated by positive values. Droughts and dry spells were categorized as mild when the *SPI* value ranged from 0 to –0.99; moderate when values were from –1.0 to –1.49; severe when the value range was from –1.5 to –1.99; and extreme when the value range was from –2.00 and below. The index is usually negative for drought presence and positive for wet conditions. As the dry or wet conditions become more severe, the index becomes more negative or positive (https://climate.copernicus.eu/about-data-and-analysis).

Table 1. SPI values

≥2.00	Extremely wet
1.50 to 1.99	Very wet
1.00 to 1.49	Moderately wet
–0.99 to 0.99	Near normal
–1.00 to –1.49	Moderately dry
–1.50 to –1.99	Severely dry
≤–2.00	Extremely dry

Sources: *Lloyd-Hughes* and *Saunders* (2002), *WMO* (2012).

3.1. Importance and preference of SPI analysis in Kenya

SPI is one of the most mentioned drought indicators in many previous studies in the world (*Kchouk, et al*., 2021), especially so in East Africa and the Horn of Africa. In Australia-Oceania, the Middle East, the North Africa (MENA), and the Sub-Saharan Africa (SSA), there are fewer studies which have used hydrological indices. As indicated by *WMO* (2012), *SPI* is a widely applied index for drought detection on a different scale (i.e., 1, 3, 6, 9, 12 months) mostly due to its versatility to space and time as well as climatic conditions. This study used total annual precipitation data (12 months) to compute *SPI* and gridded monthly scale data from CRU TS. Various studies have used combined drought index (CDI) (*Mutua* and *Balint*, 2009; *Sepulcre-*

Canto et al., 2012; *WMO*, 2012; *Shilenje et al.,* 2019), because more variables are available (temperature and vegetation). *SPI* is also widely used in India due to its adaptability, conformity to various time scales (*Shah et al.,* 2015; *Nandargi* and *Aman*, 2017), and different climatic conditions, and in Australia (*Abawi et al*., 2003) and Mexico (*Giddings et al.,* 2005) to characterize drought of various magnitudes and intensities. It has been intensely used in Kenya for drought characterization in Laikipia county and Tana River county (*Huho* and *Mugalavai*, 2010; *Ngaina et al*., 2014); Turkana county, *Opiyo, et al*. (2014) ; Laikipia county *Karanja et al*. (2017); and Makueni County *Musyimi et al*. (2018). The index is reliable to address droughts at multiple time durations for a wide range of climatic regions over the world (*Zhai et al*., 2010; *Stricevic et al*., 2011).

3.2. Limitations of SPI

SPI computation has various limitations, for instance its inability to consider and account for water deficit triggered by other processes such as evapotranspiration, deep infiltration, soil moisture content availability, and recharging abilities as well as surface runoff (*Onyango,* 2014). Better performance of the indices requires a couple of factors that influence water availability and deficiency such as the Palmer drought index. Data unavailability renders the use of other indices futile. Based on this, *Ntale* and *Gan* (2003) established that *SPI* is the most appropriate after comparing it with the Palmer drought severity index (PDSI) and Bhalme–Mooley drought index (BDI) in monitoring drought over East Africa. The probabilistic nature of the *SPI* is also a noted limitation as stated by *Agnew* (2000). Though *SPI* computation considers rainfall as the only attribute for drought characterizing, droughts need a couple of other climate parameters. They include but are not limited to soil moisture, surface runoff, and evapotranspiration. Further, in relation to different data sources, it is a challenge to compute *SPI* from long-term in-situ data from Kenya, because most weather stations do not have reliable data and so available data as well as other gridded data sources are hardly available.

4. Results and discussion

4.1. Precipitation coefficient variation (in-situ data)

The amount of precipitation received in each area varies in space and time in different climatic regions across the world (*Huho,* 2017; *Kalisa et al*., 2020). According to *Achite et al.* (2021), the coefficient of variation (*CV*) statistically measures the difference between the data values and the long-term mean value of a certain series of data. High values of *CV* indicate higher variability. In Kenya, the variation occurs mostly in the arid and semi-arid counties, which cover 89% of Kenya's total land mass (29 out of 47 counties are classified as arid or semi-arid) (*Akuja* and *Kandagor*, 2019). The lower eastern counties form part of the

arid and semi-arid counties in Kenya hence the study. Purposively, *CV* was computed to establish annual precipitation variations in the lower eastern counties. Machakos station had a computed *CV* of 29%. This implies that annual precipitation varied by ±29% from its long-term average of 679 mm. Voi meteorological station had a *CV* of 34% an implication of ±34% from the long-term average of 568 mm. Makindu station recorded a *CV* of 37% indicating that precipitation varied by ±37% from the long-term average of 521 mm of the period under study. This implies that the annual precipitation reliability agriculturally was more suited for farmers in Machakos which had the smallest value of *CV* compared to the other stations in the other counties. Similar *CV* values have been recorded in previous studies in India, Africa, and Kenya (*Kisaka et al.,* 2015; *Arvind et al.,* 2017; *Muthoni et al.,* 2019; *Achite, et al*., 2021). This is fundamental in guiding farmers in agricultural decision-making on the nature and variety of crops to plant each year. In addition to this, analysis of the spatial distribution of the *CV* is vital for early warning, preparedness, and understanding of the likelihood of extreme events occurrence (*Achite et al.,* 2021). Regions that experience higher interannual variability in precipitation are highly likely to face extreme floods and severe droughts (*Halifa-Martin et al*., 2021).

4.2. Drought characterization and dry spell analysis from annual (in-situ) data

Drought is a recurrent phenomenon in most arid and semi-arid counties of Kenya as suggested by previous studies (*Huho* and *Mugalavai,* 2010; *Opiyo et al*., 2015; *Karanja et al*., 2017). Increased temperatures and precipitation variability are expected to worsen droughts as stated by *Schilling et al*. (2014) in their study from Turkana county. From this study, analysis shows that droughts ranging from mild, to severe and extreme, were experienced between 1991 and 2018 in the studied counties. Extreme drought was experienced in 2016 in Machakos county. Severe droughts occurred in 2003 and 2005 in Taita-Taveta county running from the year 2016 to 2017 (2 years). Makueni county experienced a 2-year run of severe drought from the year 2005 to 2006. Similar extreme droughts occurred in 2000, 2008, and 2009 in several counties of Kenya (*Opiyo et al*., 2015). Droughts of varied frequencies were experienced across the counties, where moderate/mild droughts were predominant for the whole period, 1990–2018 (*Table 2*). Mild droughts of varying duration and frequencies were observed from the dataset of the Kenya Meteorological Department, for instance, in Machakos county, where a 1-year drought was experienced in 2017, and 2-year droughts were experienced from 1991 to 1992 and 1995 to 1996. 3-year droughts occurred in runs from 1999 to 2001, 2003 to 2005, 2007 to 2009, and a 4-year drought period from 2011 to 2014. Similar mild drought occurrence was evident in Taita-Taveta county (Voi station) a 3-year drought that occurred from 1999 to 2001 and Makueni County (Makindu station) from the year 2002 to 2003. More than 52% (15 years) of the droughts that occurred in the counties were spatially widespread. Similar

observations were made in Hungary by *Mohammed* and *Harsányi* (2019), who noted that Békéscsaba, Budapest, and Miskolc stations experienced 3-year drought events while Pápa and Siófok experienced 2-year and 5-year drought events, respectively, from 1985 to 2015.

Table 2. Frequencies (weighting by the length) of drought events in extreme, severe, and moderate /mild categories for SPI (1990–2018) (Annual droughts) Data source: Kenya Meterological Department.

County	Station	Drought category	Number of droughts	Total
Machakos	Machakos	Extreme	1	
		Severe	0	
		Moderate/mild	18	19
Makueni	Makindu	Extreme	0	
		Severe	2	
		Moderate/mild	16	18
Taita Taveta	Voi	Extreme	0	
		Severe	4	
		Moderate/mild	11	15

4.3. Probability of exceedance and return period for precipitation (in-situ data)

Probability of exceedance refers to the likelihood that the actual rainfall during a period will be equal to the estimated expected rainfall amount each year or might exceed in each period with a specific probability (*Raes*, 2004). The maximum annual amounts observed in the three stations were 1155 mm in 2006 at Machakos, 1118 mm in 1998 at Voi, and 991 mm in 1998 at Makindu. The probability of exceedance of precipitation for the three stations was 0.02. This result implies that it has a probability of 2% of occurrence in any given year for the three stations from the three counties of the available in-situ data. This also means that the amount of precipitation is likely to occur 2 times every 98 years, and it has a probability to re-occur (return period) once every 30 years. These observations are in tandem with *Olatunde* and *Adejoh* (2017), who indicated a return period of annual rainfall amount in 36 years in Lokoja, central North Nigeria. The lowest precipitation amount was received in the year 2016 with an amount of 281 mm from Machakos. Voi station recorded its lowest amount of precipitation in the year 2003 amounting to 210 mm, while Makindu had the lowest precipitation amount of 155 mm in the year 2005. The annual probability exceedance was 0.98, which meant it has a 98% probability to be equal to or exceeding in any year for the three counties. The computed values (return periods

and exceedance probabilities) for precipitation amount indicated that 19 years (66%) of 29 years under study had precipitation amounts below the long-term mean of 679 mm at Machakos station, Machakos county. From Voi station, Taita-Taveta county, 15 years (52%) had precipitation below the long-term mean of 568 mm, while at Makindu station, Makueni county, 18 years (62%) had precipitation below the long-term mean of 521 mm. These results imply droughts of varied frequencies and severities, whereby moderate /mild droughts were predominant for the whole period, 1990–2018 across the three counties (*Table 2*).

4.4. Drought characterization based on different time scales of SPI from CRU dataset, 1986–2016

Based on a 3-month scale, the results indicate high drought frequency oscillations (*Fig. 3a*). This is attributed to the shortest time of analysis in which precipitation, the analyzed parameter, depicted changes at a higher speed (*Kimaru et al*., 2019; *Rascón et al*., 2021; *Wang et al*., 2022). The behavioral pattern of the 3-month *SPI* indices followed a similar pattern. The 3-month *SPI* represents short- and medium-term moisture conditions, as well as seasonal precipitation estimates and implies the accumulation of consecutive periods of three months of drought indication (*WMO*, 2012). The values ranged from –3.3 in Taita-Taveta to 3.1 in both Machakos and Makueni counties (*Table 3*). Mild to moderate drought events were more frequent in the three counties, but severe and extreme droughts interspersed throughout 31 years across the counties. The 3-month *SPI* indicates immediate effects of soil moisture reduction as stated by the *WMO* (2012) and Copernicus European Drought Observatory (*EDO*, 2020).

Table 3. Statistical summary of the *SPI* indices at different time scales from the three counties

County	Index-time scale	Mean ($\bar{x}$)	SD(σ)	Minimum	Maximum
Machakos	SPI-3 months	0.003	0.99	–3.1	3.0
Makueni		0.004	0.99	–3.3	3.1
Taita Taveta		0.005	0.99	–3.1	2.8
Machakos	SPI-6 months	0.005	0.98	–2.6	2.5
Makueni		0.007	0.97	–2.4	2.1
Taita taveta		0.004	0.98	–2.8	2.7
Machakos	SPI-9 months	0.006	0.97	–2.5	2.7
Makueni		0.008	0.95	–2.2	2.3
Taita Taveta		0.004	0.98	–2.9	2.9
Machakos	SPI-12 months	0.005	0.97	–2.5	2.7
Makueni		0.007	0.96	–2.2	2.3
Taita taveta		0.003	0.98	–2.6	2.6

The *SPI* values computed on a 6-month time scale oscillated between –2.6 and 2.5 in Machakos county, –2.4 and 2.1 in Makueni county, and –2.8 and 2.7 in Taita-Taveta county (*Fig. 3b*). 6-month *SPI* can be quite useful for displaying precipitation over several seasons. From the 6-month time scale, the severities were less compared to the 3-month time scale. Results also indicated that drought frequency in the 3- and 6-month time scales was high, and the durations were shorter conforming with a study by *Kalisa et al.,* (2020) who noted similar observations in East Africa. More variability was observed from the analysis across the counties, depicting short duration and higher frequency of droughts over years. Contrary to this, on longer time scales, a decrease in variability is observed and the frequency of droughts is less but the drought duration becomes long (*Avilés et al*., 2015). This was the observation for the 9- and 12-month *SPI* indices and longer duration as well as stability (*Figs. 3c-d*). This is caused by slowering variation of index values.

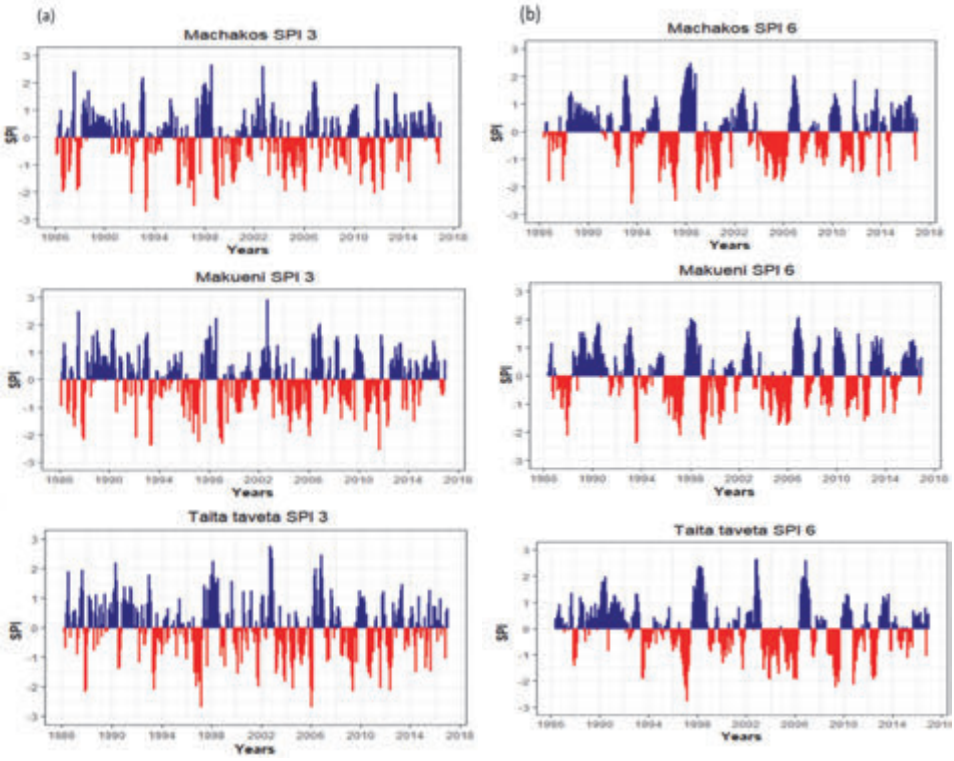

Fig. 3. 3-month *SPI* (a) and 6-month *SPI* (b) for the 1986–2016 period with mild, moderate, severe, and extreme drought severity bands as well as wet events.

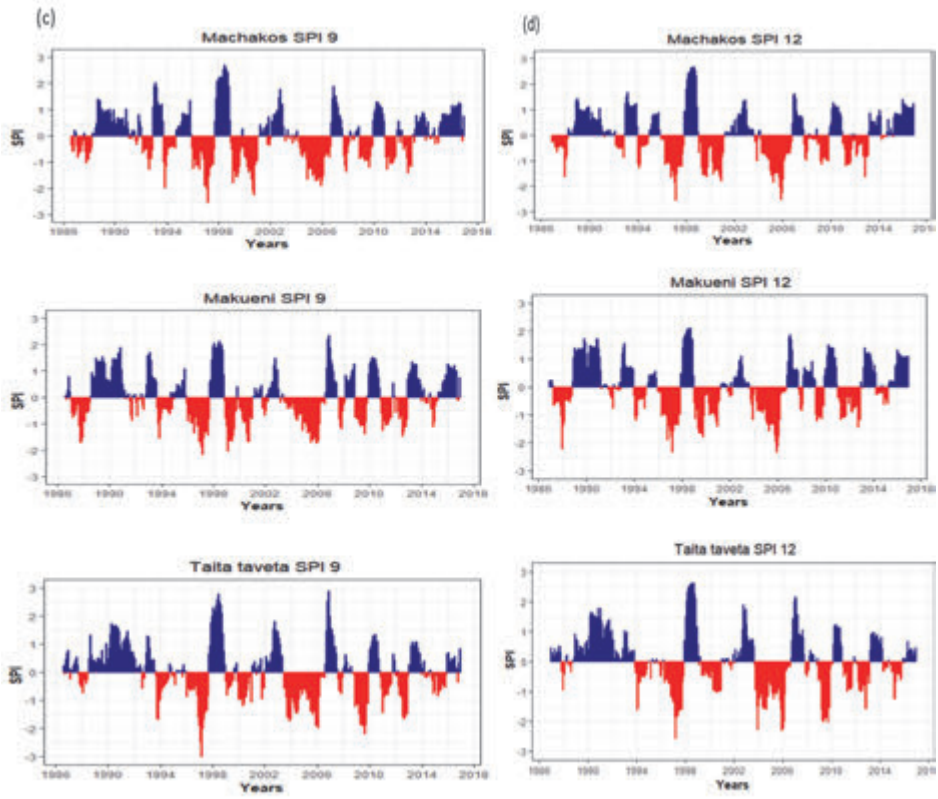

Fig. 3 (continued). 9-month *SPI* (c) and 12-month *SPI* (d) for the 1986–2016 period with mild, moderate, severe, and extreme drought severity bands as well as wet events.

The 9-month *SPI* values ranged between –2.5 and 2.7 in Machakos county, –2.2 and 2.3 in Makueni county, and –2.9 and 2.9 in Taita Taveta county. From these time scales, the *SPI* represents long-term precipitation trends. The 12-month indices were similar to the 9-month time scales for Machakos and Makueni counties, while Taita Taveta county *SPI* values ranged from –2.6 to 2.6 (*Table 3*). Droughts were more intense for the three counties between 2004 and 2005 on 9-month and 12-month time scales (*Fig. 3*). This was because as indicated earlier when the timescales are longer (9 and/or 12 months), the *SPI* values respond very slowly to changes in climate variables making the drought events less frequent but more long-lasting and, in some cases, more intense according to *Castillo-Castillo et al*., (2017). A study by *WMO* (2012) and *EDO* (2020) indicated that

SPI analysis for a longer duration, e.g., 12 months and above is a good measure for observing reduced water levels in reservoirs as well as recharging of groundwater. There existed noticeable and considerable variation in the intensity, duration, and occurrence of drought and wet episodes among the three counties (*Fig. 3*). A study by *Ahmad et al*. (2016) indicated that the variation in intensity is caused by seasonal rainfall data, and *SPI* is influenced by the amount of rainfall received in an area. In our study, the three counties experience two rainy seasons, a long-term (MAM) and a short-term (OND). This corroborates with *Kalisa et al.* (2021), who indicated that droughts vary in duration, severity, and magnitude from one region to another and through various decades.

4.5. Comparison of the annual and the 12-month SPI from the two datasets

SPI computation using annual precipitation and monthly scale precipitation data exhibited a major difference in quantifying drought and dry spell characteristics in seasonal intensity, seasonal frequency, and seasonal duration as observed. This depicts seasonal precipitation variation and identifies the driest and wettest seasons (*Hänsel et al.,* 2019), which is essential for water and agricultural planning. Results from *Fig. 3d* indicated the frequency, duration, and intensity of droughts on a 12-month scale, which was difficult to realize when annual precipitation data was used to compute *SPI* (*Fig. 4*). However, annual *SPI* computation can depict annual drought severity and year runs of brought consecutive droughts, 3-year droughts, and 4-year drought events (*Fig. 4*). This can be achieved using a 12-month time scale as well as by observing the intensity of consecutive months across the years as depicted in *Fig. 3d*. The intensities of alternating droughts, dry spells, and wet episodes are higher on minimal and shortened monthly scales. As it is indicated by *Liu* and *Liu* (2019) and *Rascón et al.* (2021), *SPI* computation uses precipitation, which is the reason behind the intensity of such alternating dry and wet episodes.

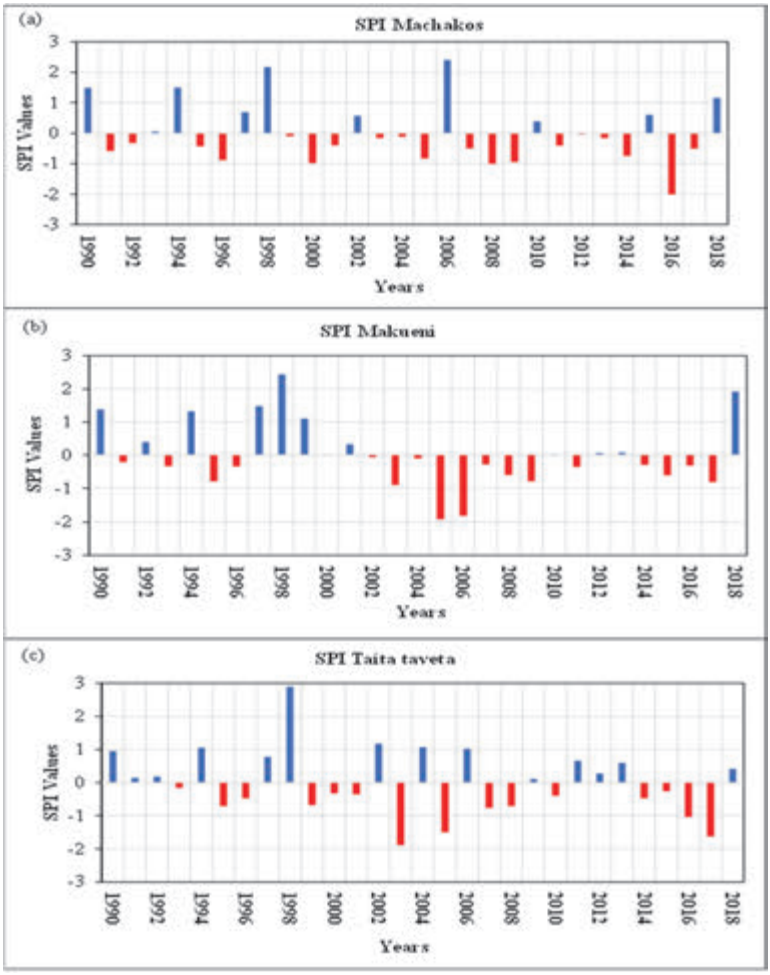

Fig. 4. Annual *SPI* values for Machakos (a), Makueni (b), and Taita-Taveta (c) counties for in-situ data from 1990 to 2018 with mild, moderate, severe, and extreme drought severity bands as well as wet episodes among years. Source of dataset: Kenya Meteorological Department.

5. Conclusions

This study analyzed monthly (3, 6, 9, and 12) *SPI* values using Climatic Research Unit Time-series (CRU TS), CRU TS 3.25 datasets for the period 1986–2016 (31 years) as well as annual *SPI* values using in-situ data for the period 1990–2018 in arid and semi-arid counties of Kenya. The results demonstrate the ability to use precipitation as a climate parameter to compare dry spells and events as well as to characterize droughts in cases of limited and /or scarcity of data. The

intensity, duration, and frequency of droughts varied in different counties and regions due to the variation of precipitation received. From the results and figures of the two datasets, it can be stated that droughts of varying intensities and severities were more predominant than wet events across the three counties. From the in-situ data, an extreme drought took place in Machakos county in 2016, Makueni county experienced a 2-year run of severe drought from 2005 to 2006, while Taita-Taveta county experienced 2-year runs of severe droughts from 2016 to 2017. From the Climatic Research Unit Time-series (CRU TS), the frequency and intensity of droughts were observed and became more noticeable on the 9-month and 12-month time scales. Given the highly enormous impact of droughts in the agricultural and water sectors in Kenya and the Horn of Africa, which are fundamental for the bulging population, *SPI* analysis proves a crucial decision-making tool for the counties and the central government, agricultural and water organizations to ensure timely monitoring and adoption of mitigation measures as well as formulation of short-term (seasonal, 1-, 3-, 6-, 9-month-long) and long-time (more than 12 months) management procedures. Due to the flexibility of *SPI*, it is crucial in applications related to both short-term agricultural planning using monthly-based *SPI* frequency and long-term hydrological management using annual-based *SPI* frequency. This is fundamental for future climate variability preparedness in prone and drought risk counties, and for resilience planning in Kenya.

Acknowledgements: The authors are grateful to anonymous reviewers for useful, constructive comments and suggestions which contributed to the improvement of the quality of this scientific article. The corresponding author is also grateful to the Stipendium Hungaricum Doctoral Research Scholarship, Tempus Public Foundation of the Hungarian Government which financially supports his Ph.D. research.

References

Abawi, Y., Dutta, S., and *Ritchie, J.,* 2003: Potential use of climate forecasts in water resources management. In (eds. *Stone, R*., and *Partridge, I.*) Science for drought: Proceedings of the National Drought Forum at Brisbane, Australia, Department of Primary Industries, Queensland, 78–81. http://doi.org/10.13140/RG.2.1.2623.1201

Achite, M., Caloiero, T., Wałęga, A., Krakauer, N., and *Hartani, T*., 2021: Analysis of the Spatiotemporal Annual Rainfall Variability in the Wadi Cheliff Basin (Algeria) over the Period 1970 to 2018. *Water 13*(11), 1477. https://doi.org/10.3390/w13111477

AghaKouchak, A., Mirchi, A., Madani, K., Di Baldassarre, G., Nazemi, A., Alborzi, A., Anjileli, H., Azarderakhsh, M., Chiang, F., Hassanzadeh, E., Huning, L.S., Mallakpour, I., Martinez, A., Mazdiyasni, O., Moftakhari, H., Norouzi, H., Sadegh, M., Sadeqi, D., Van Loon, A.F., and *Wanders, N.,* 2021: Anthropogenic drought: Definition, challenges, and opportunities. *Rev.Geophys. 59*, e2019RG000683. https://doi.org/10.1029/2019RG000683

Agnew, C.T., 2000: Using the SPI to identify drought. *Drought Network News 12*, 6–12. https://www.researchgate.net/publication/280075154_Using_the_SPI_to_Identify_Drought

Ahmad, L., Parvaze, S., Majid, M., and *Kanth, R.H.,* 2016: Analysis of historical rainfall data for drought investigation using standard precipitation index (SPI) under temperate conditions of Srinagar Kashmir. *Pakistan J. Meteorol. 13,* 29–38. https://www.researchgate.net/publication/319058816_Analysis_of_Historical_Rainfall_Data_for_Drought_Investigation_Using_Standard_Precipitation_Index_SPI_Under_Temperate_Conditions_of_Srinagar_Kashmir

Ajuang, C.O., Abuom, P.O., Bosire, E.K., Dida, G.O., and *Anyona, D.N.,* 2016: Determinants of climate change awareness level in upper Nyakach Division, Kisumu County, Kenya. *Springer Plus 5*(1), 1015. https://doi.org/10.1186/s40064-016-2699-y

Akuja, T.E. and *Kandagor, J.,* 2019: A review of policies and agricultural productivity in the arid and semi-arid lands (ASALS), Kenya: the case of Turkana County. *J. Appl. Biosci. 140*, 14304–14315. https://doi.org/10.4314/jab.v140i1.9

Alusa, L.A. and *Mushi, M.T.*, 1974: A study of the Onset, Duration, and Cessation of the Rains in East Africa. Proceedings of the International Tropical Meteorology meeting in Nairobi, Kenya. American Meteorological Society, Boston, Massachusetts, USA, 133–140.

Avilés, A., Célleri, R., Paredes, J., and *Solera, A.,* 2015: Evaluation of Markov chain-based drought forecasts in an Andean regulated river basin using the skill scores RPS and GMSS. *Water Resour. Manage. 29*, 1949–1963. https://doi.org/10.1007/s11269-015-0921-2

Arvind, G., Ashok Kumar, P., Girish Karthi, S., and *Suribabu, C.R.*, 2017: Statistical analysis of 30 years rainfall data: a case study. IOP Conference Series: *Earth Environ. Sci. 80*, 12067. https://doi.org/10.1088/1755-1315/80/1/012067

Assamnew, A.D. and *Mengistu Tsidu, G.*, 2022: Assessing improvement in the fifth-generation ECMWF atmospheric reanalysis precipitation over East Africa. *Int. J. Climatol. 43*, 17–37. https://doi.org/10.1002/joc.7697

Ault, T.R., 2020: On the essentials of drought in a changing climate. *Science*, 368.6488: 256–260. https://doi.org/10.1126/science.aaz5492

Awuor, C.B., Orindi, V.A., and *Ochieng, A*. 2008: Climate change and coastal cities: the case of Mombasa, Kenya. *Environ. Urbanizat. 20*(1), 231–242. https://doi.org/10.1177/0956247808089158

Ayugi, B.O., Tan, G., Ongoma, V., and *Mafuru, K.B.*, 2018: Circulations associated with variations in boreal spring rainfall over Kenya. *Earth Syst. Environ. 2*, 421–434. https://doi.org/10.1007/s41748-018-0074-6

Azmi, M., Rüdiger, C., and *Walker, J.P.,* 2016: A data fusion-based drought index. *Water Resour. Res. 52*, 2222–2239. https://doi.org/10.1002/2015WR017834

Borona, P., Busch, F., Krueger, T., and *Rufin, P.,* 2021: Uncertainty in Drought Identification Due to Data Choices, and the Value of Triangulation. *Water 13*, 3611. https://doi.org/10.3390/w13243611

Cammalleri, C., Vogt, J.V., Bisselink, B., and *de Roo, A.,* 2017: Comparing soil moisture anomalies from multiple independent sources over different regions across the globe. *Hydrol. Earth Syst. Sci. 21,* 6329–6343. https://doi.org/10.5194/hess-21-6329-2017

Castillo-Castillo, M., Ibáñez-Castillo, L.A., Valdés, J.B., Arteaga-Ramírez, R., and *Vázquez-Peña, M.A.,* 2017: Analysis of meteorological droughts in the Fuerte river basin, Mexico. *Water Sci. Technol. 8*(1), 35–52. https://doi.org/10.24850/j-tyca-2017-01-03

CRED, 2020: The human cost of disasters – an overview of the last 20 years 2000–2019. Technical Report. Centre for Research on the Epidemiology of Disasters (CRED) United Nations Office for Disaster Risk Reduction. https://www.undrr.org/publication/human-cost-disasters-overview-last-20-years-2000-2019

Dalu, M.T., Shackleton, C.M., and *Dalu, T.,* 2018: Influence of land cover, proximity to streams and household topographical location on flooding impact in informal settlements in the Eastern Cape, South Africa. *Int. J. Disaster Risk Reduct. 28*, 481–490. https://doi.org/10.1016/j.ijdrr.2017.12.009

Downing, T., Watkiss, P., Dyszynski, J., Butterfield, R., Devisscher, T., Pye, S., and *Sang, J.,* 2009: The economics of climate change in Kenya: Final report submitted in advance of COP15. 81 pp. SEI Stockholm Environment Institute. Project Report. Available at: https://mediamanager.sei.org/documents/Publications/SEI-ProjectReport-Downing EconomicsOfClimateChangeKenya-2009.pdf

EDO, 2020: Copernicus European Drought Observatory, 2020. EDO Indicator Factsheet, Standardized Precipitation Index (SPI), European Commission, 2020. https://drought.emergency.copernicus.eu/

Edwards, D.C. and *McKee, T.B.,* 1997: Characteristics of 20th Century Drought in the United States at Multiple Times Scales. *Atmos. Sci. Paper 634*, 1–30. http://hdl.handle.net/10217/170176

Ghasemi, A. and *Zahediasl, S.,* 2012: Normality tests for statistical analysis: a guide for non-statisticians. *Int. J. Endocrinol. Metabolism, 10*(2), 486. https://doi.org/10.5812%2Fijem.3505

Giddings, L., Soto, M., Rutherford, B.M., and *Maarouf,* A., 2005: Standardized precipitation index for Mexico. *Atmósfera 18*(1), 33–56. https://www.researchgate.net/publication/26433871_Standardized_Precipitation_Index_Zones_for_Mexico

Guenang, G.M. and *Kamga, F.M.,* 2014: Computation of the Standardized Precipitation Index (SPI) and Its Use to Assess Drought Occurrences in Cameroon over Recent Decades. *J. Appl. Meteorol. Climatol. 53*, 2310–2324. https://doi.org/10.1175/JAMC-D-14-0032.1

Hänsel, S., Ustrnul, Z., Łupikasza, E., and *Skalak, P.,* 2019. Assessing seasonal drought variations and trends over Central Europe. *Adv. Water Resour. 127,* 53–75. https://doi.org/10.1016/j.advwatres.2019.03.005

Halifa-Martin, A., Lorente-Plazas, R., Pravia-Sarabia, E., Montavez, J.P., and *Jimenez-Guerrero, P.,* 2021: Atlantic and Mediterranean influence promoting an abrupt change in winter precipitation over the southern Iberian Peninsula. *Atmos. Res. 253*, 105485. https://doi.org/10.1016/j.atmosres.2021.105485

Harris, I., Osborn, T.J., Jones, P., and *Lister, D.,* 2020: Version 4 of the CRU TS Monthly High-Resolution Gridded Multivariate Climate Dataset. *Science Data 7*, 1–18. https://doi.org/10.1038/s41597-020-0453-3

Harris, I.C. and *Jones, P.D.,* 2017: CRU TS3.25: Climatic Research Unit (CRU) Time-Series (TS) Version 3.25 of High-Resolution Gridded Data of Month-by-month Variation in Climate (Jan. 1901–Dec. 2016), Centre for Environmental Data Analysis, 05 December 2017. http://doi.org/10.5285/c311c7948e8a47b299f8f9c7ae6cb9af

Hersbach, H., Bell, B., Berrisford, P., Hirahara, S., Horányi, A., Muñoz-Sabater, J., Nicolas, J., Peubey, C., Radu, R., Schepers, D., Simmons, A., Soci, C., Abdalla, S., Abellan, X., Balsamo, G., Bechtold, P., Biavati, G., Bidlot, J., Bonavita, M., De Chiara, G., Dahlgren, P., Dee, D., Diamantakis, M., Dragani, R., Flemming, J., Forbes, R., Fuentes, M., Geer, A., Haimberger, L., Healy, S., Hogan, R.J., Hólm, E., Janisková, M., Keeley, S., Laloyaux, P., Lopez, P., Lupu, C., Radnoti, G., de Rosnay, P., Rozum, I., Vamborg, F., Villaume, S., and *Thépaut, J.-N.*, 2020: The ERA5 global reanalysis. *Quart. J. Roy. Meteorol. Soc. 146*(730), 1999–2049. https://doi.org/10.1002/qj.3803

Huho, J.M., 2017: An Analysis of Rainfall Characteristics in Machakos County, Kenya. IOSR *J. Environ. Sci. Toxicol. Food Technol. 11*, 64–72. http://doi.org/10.9790/2402-1104026472

Huho, J.M. and *Mugalavai, M.E.*, 2010: The Effects of Droughts on Food Security in Kenya. *Int. J. Climate Change 2*(2), 61–72. https://doi.org/10.18848/1835-7156/CGP/v02i02/37312

Funk, C.C., Peterson, P.J., Landsfeld, M.F., Pedreros, D.H., Verdin, J.P., Rowland, J.D., Romero, B.E., Husak, G.J., Michaelsen, J.C., and *Verdin, A.P.,* 2014: A Quasi-Global Precipitation Time Series for Drought Monitoring; U.S. Geological Survey: Reston, VA, USA. *Data Series 382*, https://doi.org/10.3133/ds832

IPCC, 2021: Climate Change 2021: The Physical Science Basis. Contribution of Working Group I to the Sixth Assessment Report of the Intergovernmental Panel on Climate Change. [*Masson-Delmotte, V., Zhai, P., Pirani, A., Connors, S.L., Péan, C., Berger, S., Caud, N., Chen, Y., Goldfarb, L., Gomis, M.I., Huang, M., Leitzell, K., Lonnoy, E., Matthews, J.B.R., Maycock, T., Waterfield, T.K., Yelekçi, O., Yu, R.,* and *Zhou, B.* (eds.)]. Cambridge University Press, Cambridge, United Kingdom and New York, NY, USA. https://doi:10.1017/9781009157896

Kabubo-Mariara, J., 2008: Climate change adaptation and livestock activity choices in Kenya: An economic analysis. *Nat. Resour. Forum 32*(1), 131–141. https://doi.org/10.1111/j.1477-8947.2008.00178.x

Kalisa, W., Igbawua, T., Ujoh, F., Aondoakaa, I.S., Namugize, J.N., and *Zhang, J.,* 2021: Spatio-temporal variability of dry and wet conditions over East Africa from 1982 to 2015 using quantile regression model. *Nat. Hazards*, *106*(3), 2047–2076. https://doi.org/10.1007/s11069-021-04530-1

Kalisa, W., Zhang, J., Igbawua, T., Ujoh, F., Ebohon, O.J., Namugize, N.J., and *Yao, F.,* 2020: Spatio-temporal analysis of drought and return periods over the East African region using Standardized Precipitation Index from 1920 to 2016. *Agric. Water Manage. 237*, 106195. https://doi.org/10.1016/j.agwat.2020.106195

Karanja, A., Ondimu, K., and *Recha, C*., 2017: Analysis of Temporal Drought Characteristic Using SPI Drought Index Based on Rainfall Data in Laikipia West Sub-County, Kenya. *Open Access Libr. J. 4*, e3765. https://doi.org/10.4236/oalib.1103765

Kimaru, A.N., Gathenya, J.M., and *Cheruiyot, C.K.,* 2019: The temporal variability of rainfall and streamflow into lake Nakuru, Kenya, assessed using SWAT and hydrometeorological indices. *Hydrology 6*, 88. https://doi.org/10.3390/hydrology6040088

Kisaka, M.O., Ngetich, F.K., Mugwe, J.N., Mugendi, D., and *Mairura, F.,* 2015. Rainfall variability, drought characterization and efficacy of rainfall data reconstruction: case of Eastern Kenya. *Adv. Meteorol. 2015,* 380404, 1–16. https://doi.org/10.1155/2015/380404

Kchouk, S., Melsen, L.A., Walker, D.W., and *van Oel, P.R*., 2021: A review of drought indices: predominance of drivers over impacts and the importance of local context. *Nat. Hazards Earth Syst. Sci. Discuss*. https://doi.org/10.5194/nhess-2021-152

Kumar, M.N., Murthy, C.S., Sesha, M.V.R., and *Roy, P.S.,* 2010: The Use of Standardized Precipitation Index (SPI) for Drought Intensity Assessment. National Remote Sensing Centre, Hyderabad, 500–625. https://doi.org/10.1002/MET.136

Liu, W. and *Liu, L.,* 2019: Analysis of dry/wet variations in the Poyang Lake basin using standardized precipitation evapotranspiration index based on two potential evapotranspiration algorithms. *Water* (Switzerland) *11*, 1380. https://doi.org/10.3390/w11071380

Lloyd-Hughes, B. and *Saunders, M.A.,* 2002: A drought climatology for Europe*. Int. J. Climatol. 22,* 1571–1592. https://doi.org/10.1002/joc.846

Maingey, Y., Ouma, G., Olago, D., and *Opondo, M.,* 2020: Trends in Climate Variables (Temperature and Rainfall) and Local Perceptions of Climate Change in Lamu, Kenya. *Geogr. Environ. Sustainab. 13*(3), 102–109. https://doi.org/10.24057/2071-9388-2020-24

Masih, I., Maskey, S., Mussá, F.E.F., and *Trambauer, P*., 2014: A review of droughts on the African continent: a geospatial and long-term perspective, *Hydrol. Earth Syst. Sci. 18*, 3635–3649. https://doi.org/10.5194/hess-18-3635-2014

McKee, T.B., Doesken, N.J., and *Kleist, J.,* 1993: The relationship of drought frequency and duration to time scale. In: Proceedings of the Eighth Conference on Applied Climatology, Anaheim, California, 17–22 January 1993. Boston, American Meteorological Society, 179–184. https://asset-pdf.scinapse.io/prod/2153179024/2153179024.pdf

Mohammed, S.A. and *Harsányi, E*. 2019: Drought cycle tracking in Hungary using Standardized Precipitation Index (SPI). *Acta Agrar. Debr. 2*, 97–101. https://doi.org/10.34101/actaagrar/2/3685

Muema, E., Mburu, J., Coulibaly, J., and *Mutune, J.,* 2018: Determinants of access and utilisation of seasonal climate information services among smallholder farmers in Makueni County, Kenya. *Heliyon 4*, 19. https://doi.org/10.1016/j.heliyon. 2018.e00889

Mutsotso, R.B., Sichangi, A.W., and *Makokha, G.O*., 2018: Spatio-Temporal Drought Characterization in Kenya from 1987 to 2016. *Advances in Remote Sensin*, *7*, 125–143. http://41.89.227.156:8080/xmlui/handle/123456789/765

Musyimi, P.K, Huho, J.M., and *Opiyo, F.E.,* 2018: Understanding Drought Characteristics and Perceived Effects on Water Sources in Kenya's Drylands: A Case Study of Makindu Sub-County. In (eds. *Fymat, A.L.* and *Kapalanga, J*) Advancing Africa's Sustainable Development: Proceedings of the 4th Conference on Science Advancement. Cambridge Scholars Publishing, Newcastle upon Tyne, NE6 2PA, UK, 324–349. ISBN: 1-5275-0655-X.

Muthoni, F.K., Odongo, V.O., Ochieng, J., Mugalavai, E.M., Mourice, S.K., Hoesche-Zeledon, I., Mwila, M., and *Bekunda, M.*, 2019: Long-term spatial-temporal trends and variability of rainfall over Eastern and Southern Africa. *Theor. Appl. Climatol. 137*, 1869–1882. https://doi.org/10.1007/s00704-018-2712-1

Mutua, F.M. and *Balint, Z.,* 2009: Analysis of the general climatic conditions to support drought monitoring in Somalia. Technical Report No.W-14, FAO-SWALIM Nairobi, Kenya. https://www.faoswalim.org/resources/site_files/W14%20Analysis%20of%20General%20Climatic%20Conditions%20in%20Somalia%20in%20Support%20of%20Drought%20Monitoring.pdf

Nandargi, S.S. and *Aman, K.,* 2017: Computation of the Standardized Precipitation Index (SPI) for Assessing Droughts Over India. *Int. J. Curr. Adv. Res. 6*(12), 8545–8557. http://doi.org/10.24327/ijcar.2017.8557.1383

Ngaina, J.N., Mutua, F.M., Muthama, N.J., Kirui, J.W., Sabiiti, G., Mukhala, E., Maingi, N.W., and *Mutai, B.K*., 2014: Drought monitoring in Kenya: a case of Tana River County. *Int. J. Agricult. Sci. Res. 3*(7), 126–135. http://academeresearchjournals.org/journal/ijasr

Naumann, G., Alfieri, L., Wyser, K., Mentaschi, L., Betts, R.A., Carrao, H., Spinoni, J., Vogt, J., and *Feyen, L.,* 2018: Global changes in drought conditions under different levels of warming. *Geophys. Res. Lett. 45*, 3285–3296. https://doi.org/10.1002/2017GL076521

Nicholson, S.E., 2016: An analysis of recent rainfall conditions in eastern Africa. *Int. J. Climatol. 36*(1), 526–532. https://doi.org/10.1002/joc.4358

Niang, I., Ruppel, O.C., Abdrabo, M.A., Essel, A., Lennard, C., Padgham, J., and *Urquhart*, *P.,* 2014: *Africa*. In: Climate Change 2014: Impacts, Adaptation, and Vulnerability. Part B: Regional Aspects. Contribution of Working Group II to the Fifth Assessment Report of the Intergovernmental Panel on Climate Change. (eds. *Barros, V.R., Field, C.B., Dokken, D.J., Mastrandrea, M.D., Mach, K.J., Bilir, T.E., Chatterjee, M., Ebi, K.L., Estrada, Y.O., Genova, R.C., Girma, B., Kissel, E.S., Levy, A.N., MacCracken, S., Mastrandrea, P.R.,* and *White, L.L.*) Cambridge University Press, Cambridge, United Kingdom, and New York, NY, USA,1199-1265. ISBN 978-1-107-05816-3.

Ntale, H.K. and *Gan, T.Y.,* 2003: Drought indices and their application to East Africa. *Int. J. Climatol. 23*, 1335–1357. https://doi.org/10.1002/joc.931

Ogallo, L.O. and *Anyamba, E.K.,* 1983: Drought of tropical, central, and eastern Africa, July-Nov, and Northern springs of 1983–84. First WMO Workshop on Medium and Long-range forecast, Maryland USA. https://doi.org/10.4172/2157-7617.1000219

Onyango, O.A., 2014: Analysis of Meteorological Drought in Northeastern Province of Kenya. *J. Earth Sci. Climat. Change 5*, 219. https://doi.org/10.4172/2157-7617.1000219

Olatunde, A.F. and *Adejoh, I*., 2017: Annual exceedance probability and return periods of rainstorms in Lokoja. *Int. J. Soc. Sci. 11*, 40–46. https://www.researchgate.net/publication/323572900

Opiyo, F.E., Wasonga, O.V., and *Nyangito, M.M*., 2014: Measuring household vulnerability to climate-induced stresses in pastoral rangelands of Kenya: Implications for resilience programming. *Pastoralism 4*, 10. https://doi.org/10.1186/s13570-014-0010-9

Opiyo, F.E., Wasonga, O.V., Nyangito, M., Schilling, J., and *Munang, R.,* 2015: Drought Adaptation and Coping Strategies Among the Turkana Pastoralists of Northern Kenya. *Int. J. Disaster Risk Sci. 6*, 295–309. https://doi.org/10.1007/s13753-015-0063-4

Raes, D., 2004: Frequency analysis of rainfall data. International Centre for Theoretical Physics, Katholieke Universiteit Leuven, Department of Earth and Environmental Sciences Leuven. https://indico.ictp.it/event/a12165/session/21/contribution/16/material/0/0.pdf

Rascón, J., Gosgot, A.W., Quiñones, H.L., Oliva, M., and *Barrena, G.M.Á.,* 2021: Dry and Wet Events in Andean Populations of Northern Peru: A Case Study of Chachapoyas, Peru. *Frontiers Environ. Sci. 9*, 614438. https://doi.org/10.3389/fenvs.2021.614438

Sahoo, A.K., Sheffield, J., Pan, M., and *Wood, E.F.,* 2015. Evaluation of the tropical rainfall measuring mission multi-satellite precipitation analysis (TMPA) for assessment of large-scale meteorological drought. *Remote Sens. Environ. 159*, 181–193. https://doi.org/10.1016/j.rse.2014.11.032

Sepulcre-Canto, G., Horion, S., Singleton, A., Carrao H., and *Vogt, J*., 2012: Development of a combined drought indicator to detect agricultural drought in Europe. *Nat. Hazards Earth Syst. Sci. 12,* 3519–3531. https://doi.org/10.5194/nhess-12-3519-2012

Shah, R., Bharadiya, N., and *Manekar, V.,* 2015: Drought index computation using standardized precipitation index (SPI) method for Surat District, Gujarat. *Aquatic Procedia 4*, 1243–1249. https://doi.org/10.1016/j.aqpro.2015.02.162

Schilling, J., Akuno, M., Scheffran, J., and *Weinzierl, T.,* 2014: On raids and relations: Climate change, pastoral conflict, and adaptation in northwestern Kenya. In (eds. *Bronkhorst, S.* and *Bob, U*.) Conflict-sensitive adaptation to climate change in Africa? Climate Diplomacy, Berliner Wissenschafts-Verlag, Berlin 241–268. ISBN 978-3-8305-2010-8.

Sheffield, J. and *Wood, E.F*., 2011: Drought: past problems and future scenarios. London, Washington, DC, Earthscan, Routledge, 210. ISBN 978-184971-082-4.

Stricevic, R., Djurovic, N., and *Djurovic, Z., 2011*: Drought classification in Northern Serbia based on SPI and statistical pattern recognition. *Meteorol. Appl. 18*(1), 60–69. https://doi.org/10.1002/met.207

Shilenje, Z.W., Ongoma, V., and *Njagi, M*., 2019: Applicability of Combined Drought Index in drought analysis over North Eastern Kenya. *Nat. Hazards 99*(1), 379–389. https://doi.org/10.1007/s11069-019-03745-7

Vanella, D., Longo-Minnolo, G., Belfiore, O.R., Ramírez-Cuesta, J.M., Pappalardo, S., Consoli, S., D'Urso, G., Chirico, G.B., Coppola, A., Comegna, A., and *Toscano, A*., 2022. Comparing the use of ERA5 reanalysis dataset and ground-based agrometeorological data under different climates and topography in Italy. *J. Hydrology*: Regional Studies *42*, 101182. https://doi.org/10.1016/j.ejrh.2022.101182

Vicente-Serrano, S.M., 2006: Differences in Spatial Patterns of Drought on Different Time Scales: An Analysis of the Iberian Peninsula. *Water Res. Manage. 20*, 37–60. https://doi.org/10.1007/s11269-006-2974-8

Vicente-Serrano, S.M., Beguería, S., and *López-Moreno, J.I.*, 2010: A multiscalar drought index sensitive to global warming: the standardized precipitation evapotranspiration index. *J. Climate 23,* 1696–1718. https://doi.org/10.1175/2009JCLI2909.1

Vicente-Serrano, S.M., Beguería, S., Gimeno, L., Eklundh, L., Giuliani, G., Weston, D., El Kenawy, A., López-Moreno, J.I., Nieto, R., Ayenew, T., Konte, D., Ardö, J., and *Pegram, G.G.S*., 2012: Challenges for drought mitigation in Africa: The potential use of geospatial data and drought information systems. *Appl. Geography 34*, 471–486. https://doi.org/10.1016/j.apgeog.2012.02.001

Vicente-Serrano, S.M., Lopez-Moreno, J.-I., Beguería, S., Lorenzo-Lacruz, J., Sanchez-Lorenzo, A., García-Ruiz, J.M., Azorin-Molina, C., Morán-Tejeda, E., Revuelto, and *J., Trigo, R.*, 2014: Evidence of increasing drought severity caused by temperature rise in southern Europe, *Environ. Res. Lett. 9*(4), 9 044001. https://doi.org/10.1088/1748-9326/9/4/044001

Von Grebmer, K., Bernstein, J., Nabarro, D., Prasai, N., Amin, S., Yohannes, Y., Sonntag, A., Patterson, F., Towey, O., and *Thompson, J.*, 2016: Global Hunger Index: Getting to Zero Hunger. Welthungerhilfe, International Food Policy Research Institute, and Concern Worldwide, Bonn, Washington, DC, and Dublin. http://doi.org/10.2499/9780896292260

Wang, Q., Zhang, R., Qi, J., Zeng, J., Wu, J., Shui, W., Wu, X., and *Li, J.,* 2022: An improved daily standardized precipitation index dataset for mainland China from 1961 to 2018. *Scientific Data 9*, 124. https://doi.org/10.1038/s41597-022-01201-z

Weibull, W., 1939: A Statistical Theory of the Strength of Materials. *Generalstabens Litografiska Anstalts Förlag*, Stockholm. No. 151. https://www.worldcat.org/title/statistical-theory-of-the-strength-of-materials/oclc/873844617

WMO, 1983: Guide to climatological practices. World Meteorological Organization, *WMO – No. 100. Geneva*, Switzerland. https://www.posmet.ufv.br/wp-content/uploads/2016/09/MET-474-WMO-Guide.pdf

WMO, 2012: Standardized precipitation index user guide. No. 1090, © World Meteorological Organization, https://library.wmo.int/index.php?lvl=notice_display&id=13682#.Ykr2muhBzIU

Yanda, P.Z. and *Mubaya, C.P.* 2011: Managing a Changing Climate in Africa; Local Level Vulnerabilities and Adaptation Experiences. Dares Salaam, Mkuki wa Nyota Publishers Ltd. https://www.scirp.org/(S(351jmbntvnsjt1aadkozje))/reference/referencespapers.aspx?referenceid=2923178

Yang, H. and *Huntingford, C*., 2018: Brief communication: Drought likelihood for East Africa. *Nat. Hazards Earth Syst. Sci. 18,* 491–497. https://doi.org/10.5194/nhess-18-491-2018

Zhai, J., Su, B., Krysanova, V., Vetter, T., Gao, C., and *Jiang, T.,* 2010: Spatial variation and trends in PDSI and SPI indices and their relation to streamflow in 10 large regions of China. *J. Climatol. 23*(3), 649–663. https://doi.org/10.1175/2009JCLI2968.1

DOI:10.28974/idojaras.2024.3.2

IDŐJÁRÁS

Quarterly Journal of the HungaroMet Hungarian Meteorological Service
Vol. 128, No. 3, July – September, 2024, pp. 309–325

Climatic and bioclimatic conditions at high-altitude meteorological stations in the Carpathian Mountains and the Sudetes in years 2005–2022

Filip Miś

Adam Mickiewicz University
Doctoral School of Natural Sciences
Department of Meteorology and Climatology
Bogumiła Krygowskiego 10,
61-680 Poznań, Poland

**Author E-mail: filmis@amu.edu.pl*

(Manuscript received in final form October 5, 2023)

Abstract— The subject of the analysis were the climatic and bioclimatic conditions of the mountainous areas in Central Europe from 2005 to 2022. The study was conducted based on meteorological data from 4 stations located in 2 mountain ranges in Central Europe, which were obtained from the Ogimet database. The analysis examined the course of mean air temperature, winter days, precipitation, snow cover, wind speed, horizontal visibility, as well as the number of days with thunderstorms and fog. Subsequently, bioclimatic indices were analyzed based on the wind chill index (WCI) and the climate severity index by Osokin (So). The results confirm an increase in mean air temperature and a decrease in the number of winter days. The most significant change in mean annual air temperature was recorded at the Carphatian stations: Varful Omu (0.59 °C/10 years) and Łomnica (0.49 °C/10 years). The largest change in the WCI value was recorded at the Carpathian station Varful Omu (51 W/m^2/10 years), while the So index was 1.4/10 years.

Key-words: bioclimate, mountain areas, Europe, climate changes

1. Introduction

Contemporary climate changes, characterized by a significant increase in air temperatures resulting from human activities, no doubts are raised (*IPCC*, 2021). These changes are observed both on global and regional scales. Mountainous areas are particularly sensitive ecosystems in the context of climate change. Many

scientists (*Giorgi et al*., 1997; *Westerling et al*., 2006) believe that the alterations occurring in mountain ecosystems can serve as early warning systems for recognizing future changes in lowland environments. Climate changes in mountainous regions have been the subject of numerous studies (*Beniston*, 2006; *Żmudzka*, 2009; *Negi* and *Mukherjee*, 2020). In his work, *Beniston* (2006) demonstrated a rising trend in air temperatures at selected alpine meteorological stations. The most significant increase in the analyzed stations was observed in the 1990s, especially at the high-altitude Saentis station. *Żmudzka* (2009) showed an increase in the average air temperature and a rise in the number of hot days, along with a decrease in the number of cold days in the Polish Tatra Mountains between 1966 and 2006. *Negi* and *Mukherjee* (2020), in their study on the impact of climate change on Himalayan mountain ecosystems, confirmed an increase in the average air temperature, resulting in an extended growing season at the foot of the mountainous region. The subject of climate change in mountainous areas has also been addressed by *Głowicki* (2008). In his work on extreme thermal phenomena in the Sudetes, the author conducted a detailed analysis of extreme air temperature values at four selected Sudeten meteorological stations. The results showed an increase in air temperature in almost all months of the year. The highest changes in maximum air temperature occurred in May (0.6 °C/10 years). Additionally, the author demonstrated a decrease in the number of frosty and very frosty days, along with an increase in the number of hot and very hot days. It is a fact that mountainous areas are characterized by a harsh, challenging climate that impacts human comfort and well-being.

The scientific discipline concerned with the impact of weather and climatic conditions on living organisms, including humans, is known as bioclimatology. The primary goal of bioclimatic research is to determine the direct influence of atmospheric factors on living organisms and to assess living conditions from a climate perspective (*Kozłowska-Szczęsna et al*., 2004). This field of study is gaining increasing interest among researchers. A very popular focus of bioclimatic studies is the identification of conditions leading to heat stress in living organisms. To achieve this, researchers employ various bioclimatic indices to assess the degree of thermal discomfort experienced by humans. One such index is the Humidex, which was applied in the study by *Charalampopoulos et al*. (2006). It gauges the perceived heat by considering the combined effects of fundamental elements such as temperature and humidity. Another commonly used index in bioclimatic research is the UTCI (universal thermal climate index). It evaluates human thermal loads by taking into account several meteorological parameters, including wind speed, humidity, and solar radiation. The UTCI index has been employed in numerous bioclimatic studies, including those by *Błażejczyk et al.* (2021) and *Miszuk* (2021). In colder regions, the wind chill index (WCI) is often utilized, which incorporates wind speed and air temperature values. This index was adopted in the research conducted by *Coronato* (1993), *Przybylak* and *Araźny* (2005), and *Dogan et al*. (2020). In the work of *Przybylak* and *Araźny* (2005) concerning bioclimatic conditions on the Svalbard

archipelago, conditions at three meteorological stations were compared. The most severe conditions in terms of the WCI index were observed at the northernmost station, Ny-Alesund, where the average annual value was 1028 W/m^2, whereas at Svalbard Lufthavn, it was 937 W/m^2, and at the Hornsund station, it was 942 W/m^2. When analyzed by months, the most severe conditions were recorded in January, while the mildest conditions were in July.

The objective of this study was to characterize and assess the climatic and bioclimatic conditions at high-altitude meteorological stations in Central Europe, specifically in the Sudetes and the Carpathian Mountains. Additionally, the study aimed to determine the direction and rate of climatic changes over the investigated multi-year period.

2. Study area, source material, and study methods

The analysis utilized data from four high-altitude meteorological stations located in two mountain ranges in Central Europe (*Fig. 1, Table 1*). These stations are situated in the Sudetes, a mountain range on the border of southern Poland and northern Czech Republic. Two stations were used for the study, one at Śnieżka, the highest peak in the Sudetes and the entire Czech Republic, and another station at Serak in the Eastern Sudetes. The study also considered the Carpathian Mountains, one of the longest and northernmost mountain ranges in Europe associated with the Alpine orogenesis. Two meteorological stations were selected for analysis, one at the summit of Łomnica in the Tatras and another in the Southern Carpathians at Varful Omu (*Makowski*, 2006).

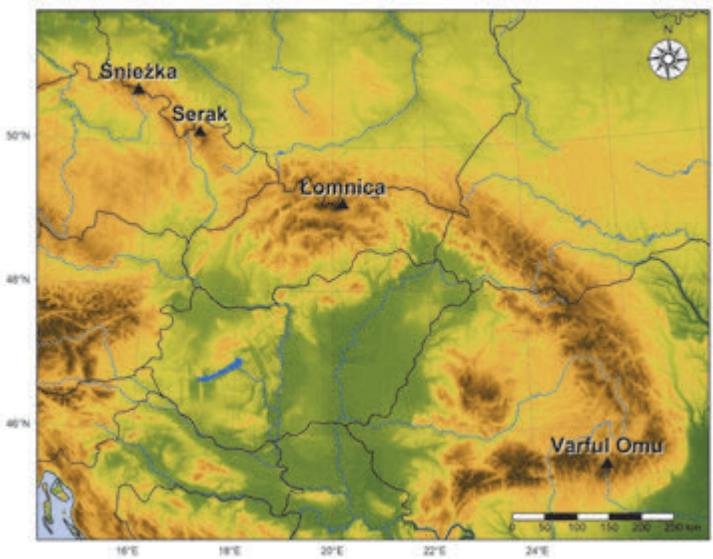

Fig. 1. Location of the stations.

Tab. 1. List of meteorological stations

Station name	Mountain range	Altitude [m a.s.l.]	Coordinates
Łomnica	Carphatians	2632	49°20N 20°21E
Serak	Sudetes	1370	50°18N 17°11E
Śnieżka	Sudetes	1602	50°73N 15°73E
Varful Omu	Carphatians	2503	44°81N 14°98E

In this study, daily meteorological data were acquired from the OGIMET dataset (https://www.ogimet.com/home.phtml.en). The research encompasses a multi-year period spanning from 2005 to 2022, with a rigorous station selection process based on data completeness criteria. The analysis hinged on daily data, encompassing parameters such as air temperature (average, minimum, maximum), mean wind speed, relative humidity, total precipitation, snow cover depth, horizontal visibility, and the count of days with thunderstorms and fog. From these datasets, fundamental climatic characteristics were computed, including the annual mean air temperature, winter mean air temperature, number of winter days (cold and very cold), annual precipitation totals, count of snow-covered days, and maximum snow depth during the season. Additionally, for each examined year, the average wind speed, horizontal visibility, and the annual count of days with thunderstorms and fog were determined. The winter period was defined as a three-month interval from December of the previous year to February of the following year, with winter days categorized as cold (tmax ≤ -10.0 °C) or very cold (tmax < -10.0 °C). Subsequently, bioclimatic conditions were analyzed using selected indices on both annual and winter scales. Two indices were considered: the wind chill index (*WCI*) (*Table 2*) and the Osokin climate severity index (*So*) (*Table 3*), the latter being exclusively applied during the winter period (*Kozłowska-Szczęsna et al*., 1997, from *Gregorczuk*, 1976; *Osokin*, 1968). The calculation of the WCI utilized the following formula:

$$WCI = (10\ v^{-2} + 10.45 - v) * (33 - t)\ 1.163, \quad (1)$$

where: is the – air temperature (°C) and v is the wind speed (m/s). The resulting value of the *WCI* indicates the sensation experienced by a person dressed in clothing with a thermal insulation value of 4.0 clo (clo is the unit of thermal insulation that is comfortable for a person).

Table 2. WCI scale

WCI **(Wm^{-2})**	**Thermal sensation**
≤ 58.2	extremely hot
58.3–116.3	hot
116.4–232.6	excessively warm
232.7–581,5	comfortably
581.6–930.4	cool
930.5–1628.2	cold
1628.3–2326.0	frosty
> 2326.0	extremely frosty

Source: *Gregorczuk* (1976) and *Kozłowska-Szczęsna et al.* (1997).

The Osokin climate severity index (*So*) is computed using the following formula:

$$S_o = (1 - 0.06\ t)\ (1 + 0.20\ v)\ (1 + 0.0006\ H_k)\ F\ A_t\,, \tag{2}$$

where t is the air temperature (°C), v is the wind speed (m/s), H_k is the absolute elevation of the measurement station, F is the coefficient characterizing the humidity of the air, and A_t is the daily air temperature amplitude. The values for the humidity coefficient (F) are assigned as follows: relative humidity < 60% — F = 0.90; 61–70% — F = 0.95; 71–80% — F = 1.0; 81–90% — F = 1.05; > 90% — F = 1.10. Similarly, the daily air temperature amplitude (A_t) is assigned values as follows: air temperature < 4.0 °C — A_t = 0.85; 4.1–6.0 °C — A_t = 0.90; 6.1–8.0 °C — A_t = 0.95; 8.1–10.0 °C — A_t = 1.00; 10.1–12.0 °C — A_t = 1.05; 12.1–14.0 °C — A_t = 1.10; 14.1–16.0 °C — A_t = 1.15; 16.1–18.0 °C — A_t = 1.20; > 18.1 °C — A_t = 1.25.

Table 3. Osokin climate severity index scale

S_o	Climatic severity
< 1.0	mild
1.0–2.0	low severe
2.01–3.0	moderately severe
3.01–4.0	severe
4.01–5.0	very severe
5.01–7.0	extremely severe
> 7.01	exceptionally severe

Source: *Osokin* (1968) and *Kozłowska-Szczęsna et al.* (1997).

For each of the parameters, the direction and rate of change over the multi-year period under investigation were determined. Additionally, the statistical significance of these changes was assessed using a t-student test at a significance level of $p < 0.05$. All maps, charts, and calculations were generated using the R programming language.

3. Results

3.1. Climatic conditions

The climate of the mentioned stations exhibits significant thermal variability. There are notably lower average air temperatures in the Carpathian Mountains compared to the Sudetes. The annual average air temperature at high-altitude stations in the Carpathians was -2.5 °C at Łomnica and -1.4 °C at Varful Omu (*Fig. 2*). The difference in the average air temperature between these stations is due to the lower geographical latitude of Varful Omu. On the other hand, in the Sudetes, the annual average air temperature on Śnieżka during the study period was 1.7 °C, which is nearly 2 °C lower than at Serak (3.6 °C). The significantly higher elevation of Śnieżka results in much harsher thermal conditions compared to Serak. The lowest annual air temperature values ranged from -3.3 °C at Łomnica in 2005 to 2.6 °C at Serak in 2013. In three out of four stations, the warmest year occurred in 2014 at Łomnica (-1.3 °C), Śnieżka (2.7 °C), and Serak (4.7 °C). On Varful Omu, the warmest year was recorded in 2018 (-0.2 °C). From the analysis conducted, it can be concluded that there was an increase in the annual average air temperature at all the considered stations during the study period. This increase was most pronounced at Łomnica, with a rate of 0.49 °C/10 years, and at Varful Omu, with a rate of 0.59 °C/10 years. These changes were statistically significant only at the Carpathian stations.

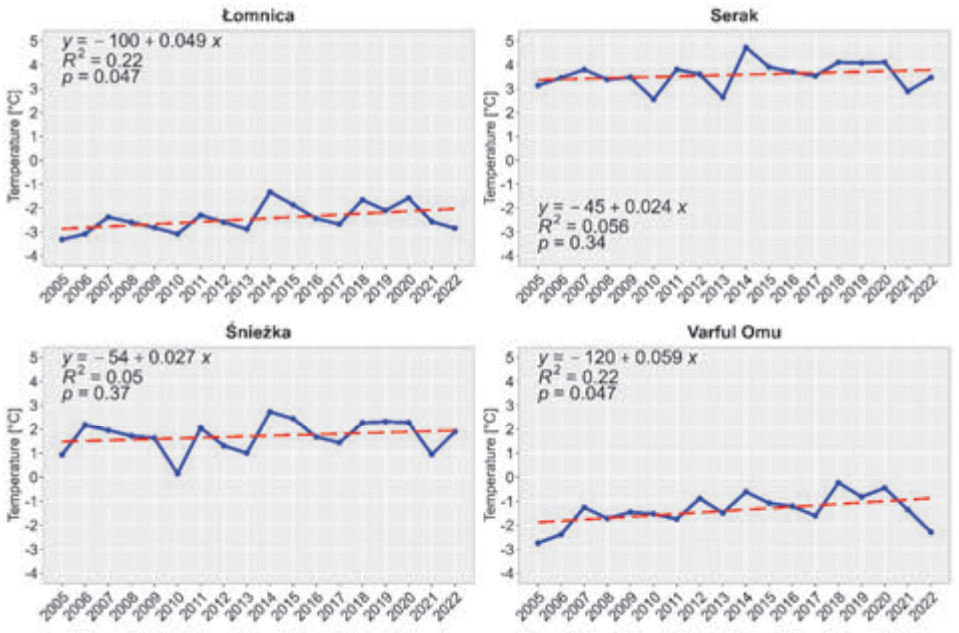

Fig. 2. The course of the average annual air temperature.

Particular attention should be given to the winter air temperature patterns. Over the study period, there was a relatively large difference in thermal conditions between the selected stations in Central Europe. The average winter air temperature at Łomnica was -9.6 °C, while at Varful Omu, it was -9.1 °C (*Fig. 3*). Noticeably milder winters were observed at Śnieżka (-5.6 °C) and Serak (-4.5 °C). The coldest winter was recorded during the 2011/12 season at Łomnica, with an average temperature of -13.4 °C. In the same season, the coldest winter at Varful Omu was slightly milder with an average air temperature of -12.,3 °C. In the Sudeten stations, the coldest winter occurred one year earlier during the 2009/10 season (-8.0 °C) at Śnieżka and (-7.8 °C) at Serak. The warmest winter was recorded during the 2007/08 season at Łomnica (-7.8 °C) and Serak (-2.7 °C). On Śnieżka and Varful Omu, the warmest winter occurred during the 2013/14 season, with average air temperatures of -3.2 °C and -6.9 °C, respectively. The study revealed that the increase in average winter air temperature was more pronounced than for the entire year. The most significant changes were observed at Serak, with a rate of 0.63 °C/10 years, and at Varful Omu, with a rate of 0.73 °C/ 10 years. However, these changes were not statistically significant.

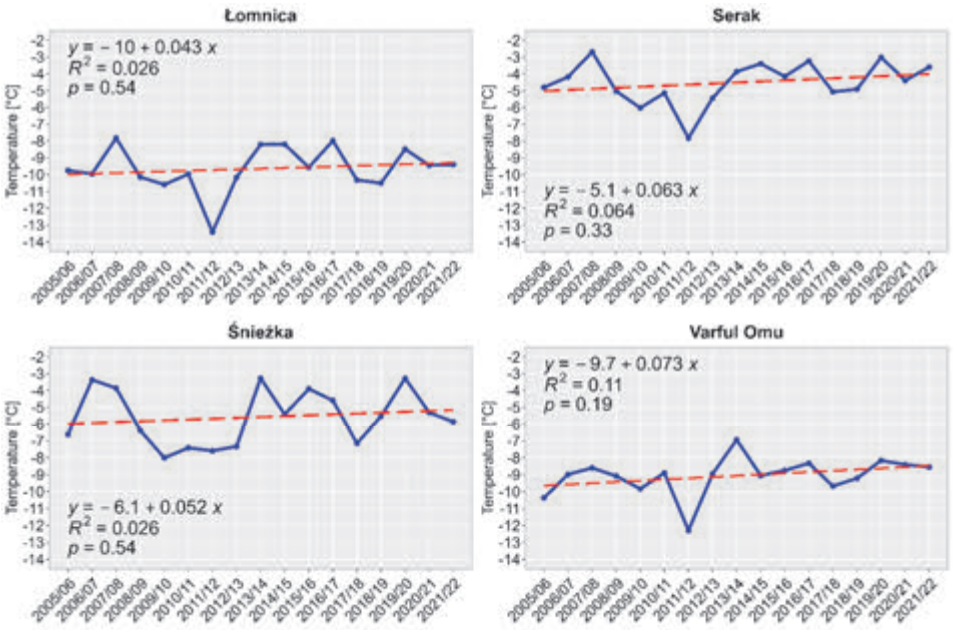

Fig. 3. The course of average air temperature in winter.

Frosty days were significantly more frequent than very frosty days, with an average of 95 days at Serak and 106 days at Śnieżka (*Fig. 4*). At the higher-altitude Carpathian stations, there were 139 frosty days at Varful Omu and 143 at Łomnica. The highest number of these days was recorded in 2022 at Łomnica (166 days) and 122 days at Serak. The highest number of frosty days at Varful Omu was in 2008 (165 days), while on Śnieżka, it was in 2021 (133 days). The lowest occurrence of these days was in 2014, with only 71 days at Serak and 85 days at Śnieżka. On average, the number of very frosty days during the study period ranged from 5 days at Serak to 35 days at Łomnica. The most extreme conditions in this regard were observed in 2005, with 48 very frosty days at Varful Omu and 57 at Łomnica. The research showed an increase in the number of frosty days at 3 out of 4 analyzed stations. The most significant changes in the number of frosty days were observed at Śnieżka, with an increase of 7.1 days/10 years. A decrease in the number of frosty days was observed at Varful Omu, with a decrease of 3.5 days/10 years. In all the analyzed stations, a decrease in the number of very frosty days was recorded. The most significant changes occurred at Varful Omu, with a decrease of 7.2 days/10 years, and at Łomnica, with a decrease of 6 days/ 10 years. However, these observed changes were not statistically significant.

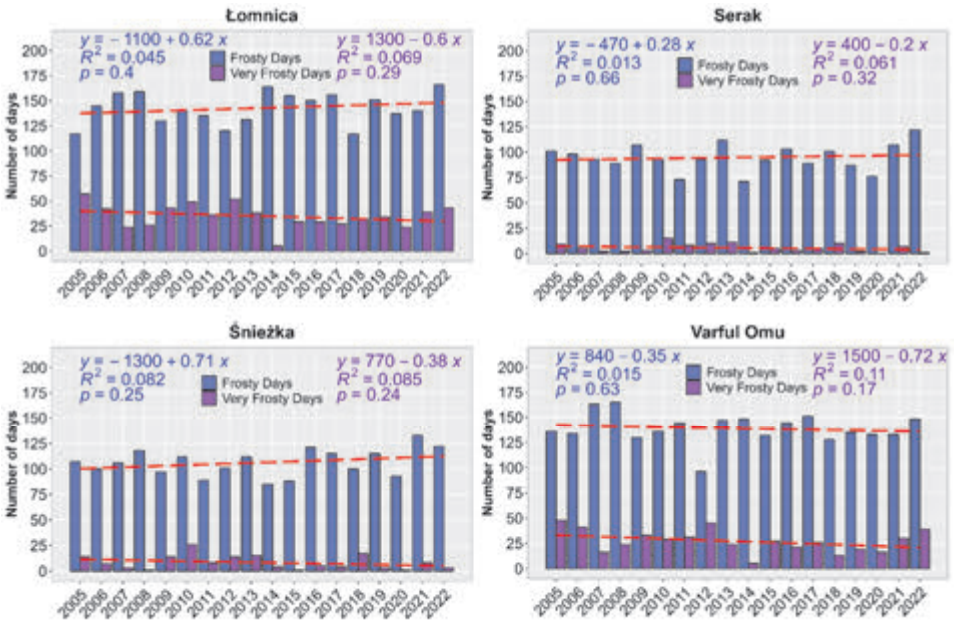

Fig. 4. The course of the number of frosty and very frosty days.

In terms of precipitation, the analyzed stations had similar values, except for the Łomnica station in the Carpathians. Over the study period, the average annual precipitation totaled 1052 mm at Serak, 1058 mm at Varful Omu, and 1102 mm at Śnieżka. A significantly higher amount of precipitation was recorded at Łomnica, with 1965 mm (*Table 4*). The lowest annual precipitation total was observed in 2011 at Varful Omu, with 752 mm, and in 2014 at Serak, with 825 mm. The highest annual precipitation total was recorded in 2017 at Varful Omu, with 1400 mm, and at Łomnica, with 2397 mm. The longest duration of snow cover was observed at Varful Omu, lasting 214 days, and at Łomnica, lasting 251 days. The shortest duration of snow cover was on average 158 days at Serak. The shortest snow cover occurred during the 2014/15 winter season at Serak (133 days), while the longest was in the 2013/14 season (278 days) at Łomnica. There was a considerable variation in the maximum snow cover thickness over the study period. On average, the maximum snow cover thickness ranged from 118 cm at Serak to 272 cm at Łomnica. The thinnest maximum snow cover during the study period was in the 2013/14 season at Serak (42 cm), while the thickest was in the 2008/09 season at Łomnica (407 cm).

Table 4. Accumulated atmospheric precipitation [mm] (A), Number of days with snow cover (B), Number of the days with maximum snow cover thickness [cm] (C). The color blue indicates the lowest value of each parameter for the stations during the studied multi-year period, while red represents the highest value.

	Łomnica			Serak			Śnieżka			Varful Omu		
Year/Season	**A**	**B**	**C**	**A**	**B**	**C**	**A**	**B**	**C**	**A**	**B**	**C**
2005 | 2005/06	1575	245	258	1037	174	**225**	1213	188	152	1029	228	190
2006 | 2006/07	2027	**224**	403	1181	142	93	1177	162	237	791	221	182
2007 | 2007/08	2325	277	328	1098	**186**	82	1241	**205**	118	863	231	**240**
2008 | 2008/09	1791	273	**407**	1094	170	178	1006	188	99	1061	221	174
2009 | 2009/10	2308	248	222	1035	167	108	1180	183	79	1134	222	142
2010 | 2010/11	2039	262	**94**	1191	150	96	**1301**	178	99	1302	219	136
2011 | 2011/12	**1399**	243	260	868	154	164	836	155	**50**	**752**	200	110
2012 | 2012/13	1674	237	264	1007	158	120	1172	178	189	987	**191**	176
2013 | 2013/14	1726	**278**	205	1066	138	**42**	1277	178	152	1064	208	124
2014 | 2014/15	1934	230	213	945	**133**	89	**825**	155	85	1002	197	172
2015 | 2015/16	1845	237	208	**856**	154	94	956	**153**	112	876	215	236
2016 | 2016/17	1948	263	302	1124	174	66	1006	162	148	1226	**237**	110
2017 | 2017/18	**2397**	246	246	1028	155	98	1178	199	103	**1400**	228	219
2018 | 2018/19	1855	236	284	912	163	159	846	170	122	1188	210	146
2019 | 2019/20	2142	244	278	1191	135	92	1274	186	199	1056	195	**72**
2020 | 2020/21	2141	267	322	**1256**	164	104	1095	177	**247**	1130	230	196
2021 | 2021/22	2079	256	292	1092	178	101	1203	169	144	1251	214	223
2022	2157			1049			1043	183		942		
Mean	**1965**	**251**	**272**	**1057**	**158**	**118**	**1102**	**176**	**138**	**1058**	**214**	**170**

Among the other meteorological elements, wind speed stands out as an important factor influencing human thermal perception. Its average value was 21 km/h at Serak, 22 km/h at Łomnica, 28 km/h at Varful Omu, and a substantial 42 km/h at Śnieżka (*Table 5*). The highest average annual wind speed was recorded in 2008, reaching 54 km/h at Śnieżka. Horizontal visibility exhibited minor variations between the mentioned stations, except for the Łomnica station, where the average annual horizontal visibility was 33 km. In the other stations, horizontal visibility ranged from 19 to 20 km. A significant difference is observed in the number of foggy days. The average annual number of foggy days ranged from 266 days at Łomnica to 305 days at Śnieżka. In the most anomalous year at Varful Omu, fog was present for almost 11 months, with 333 foggy days in 2009.

Fog occurred least frequently in 2006 at Łomnica, with 239 foggy days on record. On average, the number of days with thunderstorm ranged from 24 days at Serak to 47 days at Varful Omu. Thunderstorms were most frequent in 2010 at Varful Omu (60 days) and least frequent at Serak in 2022 (13 days).

Table 5. Average wind speed [km/h] (A), Average horizontal visibility [km] (B), Number of days with thunderstorm (C), Number of days with fog (D). The color blue indicates the lowest value of each parameter for the stations during the studied multi-year period, while red represents the highest value.

	Łomnica				Serak				Śnieżka				Varful Omu			
Year	**A**	**B**	**C**	**D**	**A**	**B**	**C**	**D**	**A**	**B**	**C**	**D**	**A**	**B**	**C**	**D**
2005	25	37	**17**	257	23	24	16	**231**	46	18	22	298	32	17	55	311
2006	23	36	22	**239**	23	19	16	254	51	18	29	**282**	34	**15**	50	314
2007	24	37	32	260	**24**	19	28	260	52	16	**40**	302	**38**	19	48	296
2008	**28**	35	24	270	23	19	22	269	**54**	16	22	315	32	18	45	308
2009	21	**27**	21	275	22	17	30	281	38	15	38	305	32	16	55	**333**
2010	23	29	23	278	21	**14**	26	283	37	**13**	26	311	32	17	**60**	322
2011	21	33	31	244	20	21	33	259	40	20	32	291	28	21	37	289
2012	23	33	30	262	22	20	**36**	272	41	19	31	310	28	24	43	**265**
2013	**19**	31	26	260	20	16	17	290	**36**	15	23	321	27	17	44	305
2014	19	31	22	286	20	18	34	**291**	37	18	34	**327**	27	21	43	307
2015	21	32	25	255	21	19	18	253	41	20	**17**	305	26	20	**31**	287
2016	21	30	34	**288**	19	18	21	283	37	19	22	314	26	18	49	326
2017	23	34	32	261	20	20	28	274	43	20	31	325	26	19	48	309
2018	19	34	**43**	269	22	22	27	261	38	**24**	26	292	24	19	48	302
2019	22	34	35	283	21	22	26	271	42	21	23	306	26	18	59	303
2020	21	38	28	260	21	**25**	21	256	41	23	26	285	**24**	**22**	41	289
2021	21	35	30	275	19	23	14	266	38	20	26	311	26	19	36	303
2022	22	**38**	24	277	**19**	25	**13**	270	41	22	22	293	25	20	50	305
Mean	**22**	**33**	**28**	**266**	**21**	**20**	**24**	**268**	**42**	**19**	**27**	**305**	**28**	**19**	**47**	**304**

3.2. Bioclimatic conditions

The values of the wind chill index (*WCI*) exhibited relatively consistent trends over the study period (*Fig. 5*). All the years in the four stations were classified as cold conditions. The highest average annual *WC*I value was 1226 W/m^2 at Śnieżka, while the lowest was 1000 W/m^2 at Serak. The mildest conditions were observed in 2014 at Serak (949 W/m^2). On the other hand, the most severe conditions were recorded in 2006 at Varful Omu, with an average *WCI* value of 1308 W/m^2. All the analyzed stations showed a decrease in *WCI* values during the study period, and these changes were statistically significant in all cases. The observed changes amounted to 27 W/m^2/10 years at both Śnieżka and Serak, and 48 W/m^2/10 years at Łomnica. The most significant changes were observed at Varful Omu, with a decrease of 51 W/m^2/10 years.

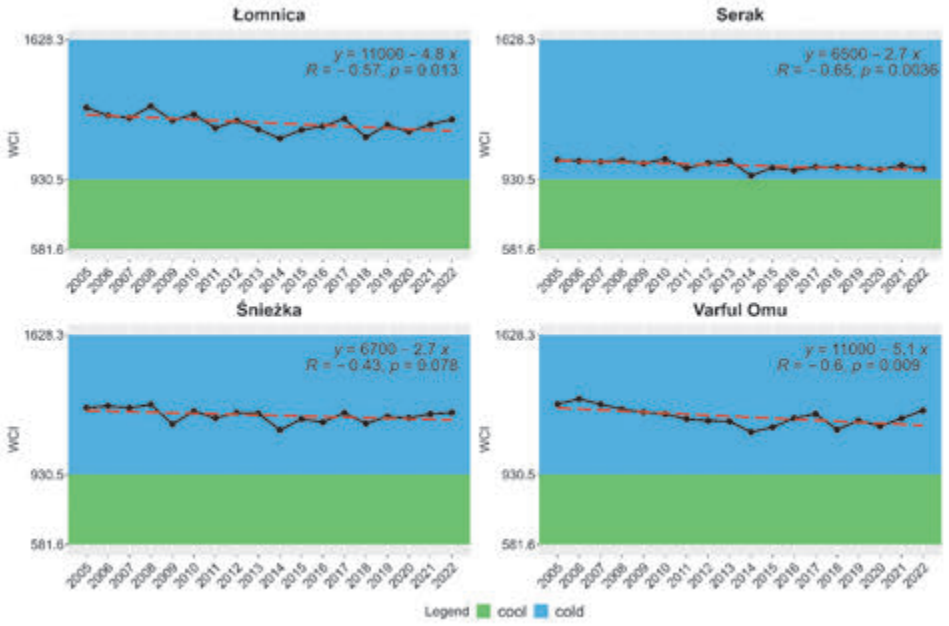

Fig. 5. The course of the wind chill index over the study period.

Significantly higher wind chill index (WCI) values were recorded in the Carpathians during the winter season (*Fig. 6*). These conditions were predominantly cold, with a few seasons classified as frosty. The frosty winters included the 2005/06, 2006/07, and 2011/12 seasons at Varful Omu, as well as the 2011/12 season at Łomnica and Śnieżka. In an average winter season, the *WCI* values ranged from 1333 W/m^2 at Serak to 1569 W/m^2 at Varful Omu. The most

severe conditions were observed in the 2011/12 season at Śnieżka (1726 W/m^2) and Varful Omu (1743 W/m^2). In the 2016/17 season at Serak, the mildest conditions were recorded, with a *WCI* value of 1277 W/m^2. The analysis showed a clear decrease in *WCI* values over the study period, ranging from 14 W/m^2/10 years at Łomnica to 55 W/m^2/10 years at Varful Omu. However, these observed changes were not statistically significant.

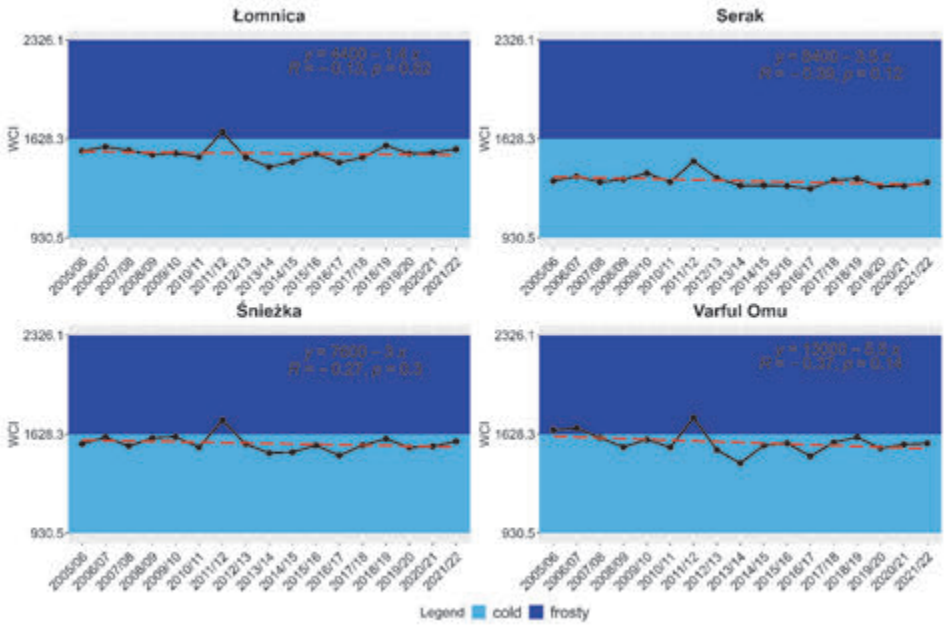

Fig. 6. The course of the wind chill index in winter.

The climate severity index values by Osokin during the winter season were classified as very severe, extremely severe, and predominantly exceptionally severe (*Fig. 7*). The first two severity classes were exclusively recorded at the Serak station, while the other stations exhibited predominantly exceptionally sharp conditions. The average value of the climate severity index during the winter season ranged from 5.4 at Serak to 11.4 at Varful Omu. At Łomnica and Śnieżka, the values were 9.5 and 9.6, respectively. The mildest winter was recorded in the 2016/17 season at Serak (4.9), while the most severe winter occurred in the 2018/19 season at Varful Omu (16.1). The research indicated a decrease in the climate severity index values at three of the analyzed stations, except for Łomnica. These changes ranged from 0.1/10 years at Łomnica to

1.4/10 years at Varful Omu. However, these changes were not statistically significant except for the Serak station.

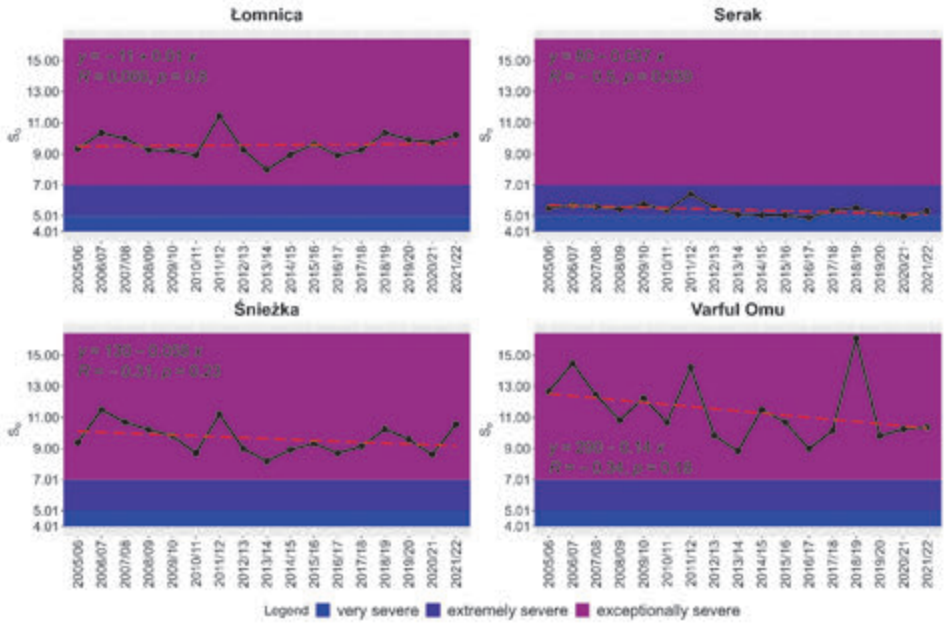

Fig. 7. The course of the Osokin climate severity index in winter.

4. Summary and discussion

The average annual air temperature varied from -2.5 °C at the Carpathian Łomnica station to 3.6 °C in the Sudetes at the Serak station. Meanwhile, on the highest peak in the Sudetes, Śnieżka, the average annual air temperature was 1.7 °C. It is worth noting that *Urban* and *Tomczyński* (2017) reported slightly different results in their study on changes in the average air temperature at Śnieżka from 1881 to 2012. In their study period, the average air temperature was 0.5 °C, with the highest values occurring in 2006 and 2011 (2.3 °C). However, in the current study, it was shown that 2014 was the warmest year at Śnieżka (2.7 °C). Particular attention should be paid to the Łomnica and Serak stations, where the coldest and warmest years in the study period were recorded. This occurred in 2005 at Łomnica, where -3.3 °C was recorded, and in 2013 at Serak, with a value of 2.6 °C. All mountain stations exhibited a significant increase in the average annual air temperature. The most pronounced changes were observed in the Carpathians at Varful Omu

(0.59 °C/10 years) and at Łomnica (0.49 °C/10 years). Previous studies also pointed to a significant increase in air temperature on high-altitude stations. *Micu* and *Micu* (2006) observed a temperature increase of 2.4 °C at the Varful Omu summit in the period from 1961 to 2003. Similarly, changes at Śnieżka amounted to 0.1 °C/10 years from 1881 to 2012 (*Urban* and *Tomczyński*, 2017).

During the winter season, the average air temperature ranged from -9.6 °C at Łomnica to -9.1 °C at Varful Omu, with -4.5 °C recorded at Serak. Similar results were obtained by *Micu* and *Micu* (2006), who, for the period from 1961 to 2003 at Varful Omu, reported a seasonal average air temperature of -9.2 °C. The coldest winter was observed in the 2011/12 season at Łomnica (-13.4 °C), while the warmest occurred in the 2007/08 season at Serak (-2.7 °C). The winter period was characterized by a significant increase in the average air temperature, ranging from 0.43 °C/10 years at Łomnica and 0.52 °C/10 years at Śnieżka to 0,73 °C/10 years at Varful Omu. A lower increase in the average air temperature at Śnieżka during the period from 1881 to 2012 was noted by *Głowicki* (2008), who reported an increase of 0.09 °C/10 years. Meanwhile, *Tomczyk* and *Miś* (2023) identified an increase of 0.25 °C/10 years from 1966 to 2021.

The increase in the average air temperature significantly influenced the frequency of winter days. The average number of frosty days ranged from 95 at Serak to 143 at Łomnica. Meanwhile, the number of very frosty days varied from 5 at Serak to 35 at Łomnica. In most cases, there was an increase in the number of frosty days and a decrease in very frosty days, except for Varful Omu, where a significant decrease in the number of frosty days was observed during the study period. On average, Śnieżka recorded 106 frosty days and 9 very frosty days. *Głowicki* (2008) observed slightly higher frequencies of winter days at Śnieżka for the period from 1951 to 2007. He recorded 129 frosty days and 12 very frosty days, which showed a decreasing trend during the study period.

The lowest average annual precipitation in the study period was recorded at the Sudeten station Serak (1057 mm), while the highest was observed at the Carpathian station Łomnica (1965 mm). The snow cover lasted the shortest time at the peak of Serak (158 days), while it persisted the longest at Łomnica (251 days). Similar results were obtained by *Szyga-Pluta* and *Mendel* (2023) in their study on meteorological conditions at Szrenica in the years 2018–2020. The authors showed that during the study period, the snow cover at the Sudeten measurement station lasted on average for 160 days per year. Among all the stations studied, the thinnest snow cover was typically observed in the Eastern Sudetes at Serak (118 cm), while the thickest cover was recorded at Łomnica (272 cm). The lowest horizontal visibility was observed at Śnieżka and Varful Omu (19 km), while the highest was recorded at Łomnica (33 km). Fog was least frequently present at Łomnica (266 days per year), while it was most frequently observed at Śnieżka (305 days per year). On the other hand, thunderstorms were least frequently observed at Serak, occurring on average for 24 days per year.

They were most frequently recorded at the Carpathian station Varful Omu, with an average of 47 days per year.

The bioclimate of the studied high mountain peaks, as represented by the wind chill index (*WCI*), was characterized by cold conditions. The mildest conditions were observed in the Sudetes at the Serak peak (949 W/m^2). On the other hand, the harshest conditions were observed at Śnieżka (1226 W/m^2). The lowest average annual *WCI* value was recorded in 2014 (949 W/m^2) at Serak, while the highest was in 2006 at Varful Omu (1308 W/m^2). Winter conditions were significantly harsher, confirming the occurrence of cold and frosty winters based on the wind chill index. Frosty winters were observed infrequently at Varful Omu, Łomnica, and Śnieżka. The most severe average winter conditions were observed at Varful Omu (1569 W/m^2), while the mildest were recorded at Serak (1333 W/m^2). Both for the entire year and for the winter period, a decrease in *WCI* values was observed, with the most significant changes noted at Varful Omu (51 W/m^2/10 years for annual values and 55 W/m^2/10 years for winter values). *Błażejczyk et al*. (2020), analyzing bioclimatic conditions based on the universal thermal climate index, *UTCI* in the Northern Carpathians, found that the station at Łomnica had the most severe conditions in the studied area. The average *UTCI* value in the period from 1986 to 2015 was -15.7 °C, while the minimum daily value of this index was as low as -73.5 °C. Next, an analysis of the Osokin climate severity index was conducted for the winter period. The high mountain stations under consideration exhibited conditions ranging from very severe to exceptionally severe, with winters primarily classified as exceptionally severe. The average value of the index during the winter period ranged from 5.4 at Serak to 11.4 at Varful Omu. The most severe winter was recorded in the 2018/19 season at Varful Omu, with a climate severity index value of 16,1. On the other hand, the mildest winter was observed in the 2016/17 season at Serak, with a severity index value of 4.9. In most of the studied stations, a decrease in the severity index value was demonstrated, except for Łomnica. Changes ranged from 0.1/10 years at Łomnica to 1.4/10 years at Varful Omu.

References

Beniston M., 2006: Mountain weather and climate: A general overview and a focus on climatic change in the Alps. *Hydrobiologia 562*, 3–16. https://doi.org/10.1007/s10750-005-1802-0

Błażejczyk K., Nejedlik P., Skrynyk O., Halaś A., Skrynyk O., Baranowski J., and *Mikulo K*., 2020: Thermal stress in the northern Carpathians and air circulation. *Miscellanea Geographica 24*(3), 147–160. https://doi.org/10.2478/mgrsd-2020-0022

Błażejczyk K., Pecejl M., Nejedlik P., Skrynyk O., and *Mikulo K.,* 2021: Thermal stress in selected mountain systems in Central and Eastern Europe – initial research based on UTCI characteristics. *Geographia Polonica 94*, 223–236. https://doi.org/10.7163/GPol.0202

Charalampopoulos M., Kamoutsis A., Panagiotou I., and *Chronopoulou-Sereli A.,* 2006: Investigation of bioclimatic performance in specific mountain areas in Greece and evaluation for decision making in tourism development. In Sixth Annual Meeting of the European Meteorological

Society (EMS)/Sixth European Conference on Applied Climatology (ECAC), EMS Annual Meeting Abstracts.
Coronato F.R., 1993: Wind chill factor applied to Patagonian climatology. *Int. J. Biometeorol.* 37, 1–6. https://doi.org/10.1007/BF01212759
Dogan M., Vural E., and *Tugrul A.V.C.I.*, 2020: Determination of Comfort Areas According to the Wind Chill Index of the Central Anatolia Region. *Kastamonu Univ. J. Engineer. Sci 6*(2), 84–94. https://dergipark.org.tr/en/pub/kastamonujes/issue/58573/824493
Flemming G. and *Schmidt M*., 1983: Klimat-środowisko-człowiek. *Państwowe Wydaw. Rolnicze i Leśne*. (In Polish)
Giorgi F., Hurrell J.W., Marinucci M.R., and *Beniston M.,* 1997: Elevation signal in surface climate change: A model study. *J. Climate 10*, 288–296. https://doi.org/10.1175/1520-0442(1997)010<0288:EDOTSC>2.0.CO;2
Głowicki B., 2008: Ekstremalne zjawiska termiczne w Sudetach w okresie współczesnych zmian klimatu. *Infrastruktura i ekologia terenów wiejskich 8*, 29–40. https://yadda.icm.edu.pl/agro/element/bwmeta1.element.agro-fc0cabd1-0d25-4c4e-affa-fa94092d6068
Gregorczuk M. 1976: O wielkości ochładzania na obszarze Polski. *Czasopismo Geograficzne 47*(3), 255–263. (In Polish)
IPCC, 2021: Climate Change 2021: The Physical Science Basis. Contribution of Working Group I to the Sixth Assessment Report of the Intergovernmental Panel on Climate Change. *Cambridge University Press*, Cambridge, United Kingdom and New York, NY, USA, In press. https://doi.org/10.1017/9781009157896
Kozłowska-Szczęsna T., Błażejczyk K., and *Krawczyk B.*, 1997: Bioklimatologia człowieka: metody i ich zastosowanie w badaniach bioklimatu Polski. *IGiPZ PAN*. (In Polish)
Kozłowska-Szczęsna T., Krawczyk B., and Kuchcik M., 2004: Wpływ środowiska atmosferycznego na zdrowie i samopoczucie człowieka. Monografie-Polska Akademia Nauk. Instytut Geografii i Przestrzennego Zagospodarowania im. Stanisława Leszczyckiego. (In Polish)
Makowski J., 2006: Geografia regionalna świata: wielkie regiony. Wydawnictwo Naukowe PWN. (In Polish)
Micu D. and *Micu M.,* 2006: Winter temperature trends in the Romanian Carpathians–a climate variability index. *AUVT-Geogr. 16,* 33–42.
Miszuk B., 2021: Tourism climate conditions in the Western Sudetes (Poland) in relation to UTCI. *Geographia Polonica 94*, 267–282. https://doi.org/10.7163/GPol.0205
Negi G.C.S. and *Mukherjee S.,* 2020: Climate change impacts in the Himalayan Mountain ecosystems. Encyclopedia of the World's biomes. Elsevier, 349–354. https://doi.org/10.1016/B978-0-12-409548-9.12056-1
Osokin I.M., 1968: O kolićestuennom uyraźenii surouosti zimnich pogod, Vesta. Nauć. Inst. Zabajkal. FU. Geogr. Obšć. SSSR, 9. (In Russian)
Przybylak R. and *Araźny A.,* 2005: Porównanie warunków klimatycznych i bioklimatycznych północnej części Ziemi Oscara II z innymi obszarami zachodniego wybrzeża Spitsbergenu w okresie 1975-2000. *Problemy Klimatologii Polarnej 15,* 119–131. (In Polish) https://repozytorium.umk.pl/handle/item/3002
Szyga-Pluta K. and *Mendel K.,* 2023: Warunki meteorologiczne na Szrenicy w latach 2018-2020. *Badania Fizjograficzne. Seria A: Geografia Fizyczna 11*, 135–153. (In Polish) https://doi.org/10.14746/bfg.2022.13.8
Tomczyk A.M. and *Miś F.,* 2023: Zimowe ekstrema termiczne w Polsce i ich cyrkulacyjne uwarunkowania. *Badania Fizjograficzne. Seria A: Geografia Fizyczna 11*, 193–205. (In Polish) https://doi.org/10.14746/bfg.2022.13.11
Urban G. and *Tomczyński K.,* 2017: Air temperature trends at Mount Śnieżka (Polish Sudetes) and solar activity, 1881–2012. *Acta geographica Slovenica*, 57(2), 33–44. https://doi.org/10.3986/AGS.837
Westerling A.L., Hidalgo H.G., Cayan D.R., and *Swetnam T.W.*, 2006: Warming and Earlier Spring Increases Western U.S. Forest Wildfire Activity. *Science 313*, 940–943. https://www.science.org/doi/full/10.1126/science.1128834
Żmudzka E., 2009: Changes of thermal conditions in the Polish Tatra Mountains. *Landform Analysis 10*, 140–146. https://yadda.icm.edu.pl/baztech/element/bwmeta1.element.baztech-article-BUJ5-00530020

DOI:10.28974/idojaras.2024.3.3

IDŐJÁRÁS

Quarterly Journal of the HungaroMet Hungarian Meteorological Service
Vol. 128, No. 3, July – September, 2024, pp. 327–344

Assessment of soil microclimate in an urban park of Budapest, Hungary

Malek Abidli[1], **Gábor Halupka**[2,3,*], and **István Waltner**[2]

[1] *Hungarian University of Agriculture and Life Sciences*
Doctoral School of Environmental Sciences
2100 Gödöllő, Páter K. u. 1., Hungary

[2] *Hungarian University of Agriculture and Life Sciences*
Institute of Environmental Sciences,
Department of Water Management and Climate Adaption
2100 Gödöllő, Páter K. u. 1., Hungary

[3] *Mining and Geological Survey of Hungary*
1145 Budapest, Columbus street 17–23., Hungary

* *Corresponding Author E-mail: Halupka.Gabor.Erno@uni-mate.hu*

(Manuscript received in final form September 9, 2023)

Abstract— Investigation of urban parks is a particular research section in the frame of urban geology, with increasing social importance. Both natural and anthropogenic factors affect these green sites, giving special scientific importance to their investigation. Thus, the behavior of such a 'composite' system is expected to be quite complex.

Based on the general circumstances, a research project was introduced in 2016 in the former Mining and Geological Survey of Hungary (now: Supervisory Authority for Regulatory Affairs). The ongoing project was focused on the behavior of urban parks. Within the frame of this research, between 2016 and 2019, field studies were started in 4 parks of Budapest. This paper is targeting one of these parks, namely Honvéd square.

Our objective is to understand the behavior of urban parks under special conditions (e.g., during heat island effects) by getting information from well-defined positions. This can be essential to perform more sustainable water management in an urban park.

Within the frame of the field works soil temperature and soil moisture measurements were being recorded manually every week in every park, at four different locations within a park. Observation points were selected to describe the different microclimates of the parks.

A statistical analysis of the data reveals that the urban heat island (UHI) effect is reflected in soil temperatures at a citywide scale and that by moderating urban soil surface temperature extremes, trees and shrubs may help to reduce the adverse impacts of urbanization on microclimate, soil processes, and human health.

It can be stated, that beside the manual measurements, the automated soil temperature detection was significantly influenced by soil depth at the Honvéd square park. At 100 cm below the surface, the soil temperature is relatively constant. It was approved that not only do deeper soil layers undergo less drastic seasonal temperature fluctuations but also the changes taking place lag further behind those of shallower soil layers.

Key-words: urban parks, soil moisture, soil temperature, urban heat island effect, urban geology, general meteorological factors.

1. Introduction

Urban parks are integral parts of the dynamic network of city ecosystems and provide vital environmental services. They support urban populations in an ecological, cultural, social, psychological, and economic context (*Burgess et al.,* 1988; *Conway,* 2000; *Gehl* and *Gemzoe*; 2001, *Grahn*, 1985; *Bowler et al.,* 2010; *Konijnendijk et al*., 2013; *Demuzere et al.*, 2014; *USEPA*, 2017; *Stępniewska*, 2021). Urban parks, unfortunately, often embody the problems of inefficient irrigation use and stormwater runoff. In fact, urban park water management has become a hot subject of growing social significance. If we understand how urban parks behave under special impacts, more effective water management can be performed (*Loures et al*., 2007).

On the other hand, the increasing urbanization of the world's population, which is projected to accelerate in the 21st century (*Angel et al*., 2005), seems to have both beneficial and detrimental effects on citizens and the environment (*United Nations,* 2014). They create their special microclimates as urban areas replace natural habitats with construction materials and anthropogenic activities (*Erell et al*., 2011).

Urbanization changes the climate and results in various climatic features that influence urban residents' everyday lives (*Honjo*, 2009; *Kalnay* and *Cai*, 2003). Urban heat island (UHI) is a phenomenon connected to both climate change and urbanization (*Bowler, et al*., 2010; *Kong et al*., 2016), which identifies urban areas with slightly higher temperatures than the nearby rural areas. Modification of the surface properties of urban areas influences the energy balance at micro- and local scales between the earth and the ambient environment (*Oké*, 1981; *Steward* and *Oké*, 2012). Microclimates can be substantially different from the dominant environment in an area that has high human impact (*Brown* and *Gillespie,* 1995). A healthy microclimate promotes the use of open spaces by the public (*Mahmoud*, 2011; *Thorsson et al*., 2004). Therefore, it is important to explore the factors that directly and indirectly affect microclimates in order to improve outdoor comfort.

Different microclimatic parameters (MPs) may be used in the study of urban microclimates. It can generally be characterized by air temperature (Ta), relative humidity (RH), wind conditions (velocity and direction), mean radiant temperature (MRT), and light intensity (*Li et al.,* 2018; *Honjo*, 2009; *Davies-Colley et al*., 2000).

For a better understanding, in the spring of 2016, the former Mining and Geological Survey of Hungary started a targeted research project on parks in Budapest, aimed at the role of microclimate in the different urban parks of the city. In this paper, we are focusing on one of these investigated parks, the Honvéd square, which is situated east of the Danube river.

The main purpose of the study is to investigate the impacts of microclimate on the urban park and to provide a reference point for the water management of

urban green spaces by better understanding the behavior of urban parks under special conditions (e.g., during heat island effects). The detection of the climatic parameters was established through two different methods, a manual detection for soil temperature and soil moisture, and an automated tool through different depths to detect the soil temperature.

2. Materials and methods

2.1. Manual detection at the Honvéd square

The study area is located in the central part of Budapest. The altitude is approximately 30 m, and the daily mean temperature is between -2.5 °C and 32 °C.

The weekly data collected was for the period from August 22, 2016 to September 26, 2019. This data was collected every week on Wednesday at around 11–12 am. The soil temperature and soil moisture data were collected from four different points. The rationale behind the selection of these four points is explained in Section 2.3. Besides these factors, air temperature and precipitation data were also detected. The park was irrigated by the local authorities. The frequency of the irrigation was according to the dry periods.

The instruments used for the manual measurements are as follows:

- Soil thermometer: To detect the soil temperature in the depth of 30 cm, a low budget 320 mm detachable soil and ground thermometer 'NATURE 6080082' was used. The temperature range of the instrument varied between -5 °C and +80 °C. The instrument was produced by NATURE, Holland.
- Soil moisture meter: The use of 'PCE-SMM 1' instrument started on November 16, 2016. Its limit of measurement for moisture content is between 0 and 50%, with an accuracy of ±0.5%. Its optimal operating temperature is between 0 and 50 °C.
- Air temperature measurements: For this purpose, an analog air thermometer was used, with the range of -35 and +50 °C.

2.2. Automated detection at the Honvéd square

In the Honvéd square, four automated soil temperature instruments (H-1, H-2, H-3, and H-4 – naming of the instruments based on the detection points' name) were installed (*Fig. 1*). The instruments have been developed by Ákos Gyenis, an expert in experimental, custom tailored soil detection devices in Pécs, Hungary.

Fig. 1. Detection points at the Honvéd square in Budapest.

The start of the automated measurements was on December 12, 2018, except in the case of H-4, which was eliminated and changed with an another sensor ('H-plus'), because of some unexpected technical problems. Detections of H-plus started on January 17, 2019.

All the equipments took measurements every hour and on 8 different levels: 0, 5, 10, 20, 30, 50, 100, and 200 cm below the surface.

2.3. Detection points

As for the field works, soil temperature and soil moisture measurements were being monitored weekly in the park, at four different locations, and the automated detection of soil temperature was performed on an hourly basis. For better observation, four points were selected to describe the different conditions of the park. The points are:

- Borderline of the park facing the northern frontage of the surrounding houses (H-1);
- A permanent sunny area (H-2);
- A permanent shady area (H-3);
- Borderline of the park facing to the southern frontage of the houses (H-4).

2.4. Limitation of the data detected

There were expected and unexpected gaps in the data series. In the first case holidays, in the latter one the weather was the reason. When the temperature is below zero the soil becomes frozen, so the moisture content could not be measured (in depths close to the surface), and it caused a malfunction of the soil moisture sensor.

2.5. Software used

For the data processing and statistical calculations, R statistical environment was used (*Venables et al.,* 2023), while the data filtering was done in MS Excel 2016.

3. Results

3.1. Analysis of the manual soil temperature and soil moisture detection at the Honvéd square

3.1.1. Soil temperature

The data has shown that the maximum and minimum air temperatures in the park were 32 °C and -2.5 °C, respectively. On the other hand, the soil temperature in the 30 cm below surface (bs) depth showed 28 °C and -1°C for H-1, 27.5 °C and -2.5 °C for H-2, 26 °C and -2 °C for H-3, and finally, 25.5 °C and -3 °C for H-4 as minimum and maximum temperature during the measurement period (*Table 1., Fig .2*).

Table 1. The highest and lowest soil temperature values at the different detection points. Manual measurements.

	H-1	**H-2**	**H-3**	**H-4**
Soil maximum temperature, °C, 30 cm bs	28	27.5	26	25.5
Soil minimum temperature, °C, 30 cm bs	-1	-2.5	2	-3

The data collected during summer 2018 showed the highest soil temperature, meanwhile, the lowest soil temperature could be detected during the winter of 2017.

Fig. 2 presents the general trend of seasonal air temperature and soil temperature in the studied downtown park, during the whole research period (2016–2019). The calculated R^2, which is the coefficient of determination value, comes to 0.0308 for the air temperature, 0.0402 for the shady point (H-3), 0.0282 for the south point (H-4), 0.0658 for the north point (H-1), and 0.0142 for the sunny point (H-2). It means that the variability in the soil temperature during the whole period is as follows: 4.02% for the Shady point, 2.82% for the South point, 6.58% for the North point, and 1.42% for the Sunny point.

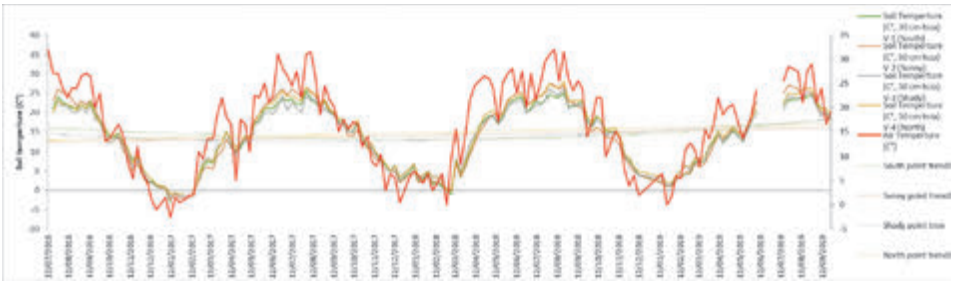

Fig. 2. Change in soil temperature, 30 cm below soil surface at the Honvéd square in Budapest.

Running of curves of the soil temperature presented in *Fig. 2* is different at the four locations. This difference is related not only to the location but also to the season. Furthermore, it is clear that during the summer season, the soil temperatures at 30 cm bs are comparatively higher at the sunny point (H-2) than at the shady point (H-3). In fact, during summer 2019, the soil temperature was 27 °C at the sunny point (H-2) and 25 °C at the shady point (H-3). On the other hand, the soil temperature at the sunny point was still higher than at the northern frontage of the surrounding buildings (H-1) in the summertime.

The results mentioned above support the irrigation effect on the temperature as a cooling factor. Over the years, the greatest UHI effects on soil surface temperature have been observed during the summer months. The vegetation effects are capable of cooling the urban atmosphere and have the ability to reduce the UHI effect and provide proof that this impact applies to the soil system (*Susca et al*., 2011). Although slightly higher, the cooling impact on the hottest days was indistinguishable from that on the mean summer day. This implies that irrigation has a greater impact on particularly hot days, as a cooling factor than the vegetation.

3.1.2. Soil moisture

When it comes to soil moisture, it was detected manually on a weekly basis, same as air temperature, for the period of August 22, 2016 to September 26, 2019. This data was collected every week on Wednesday at around 11–12 am. Soil moisture was measured at 5–10 cm depth at 4 different detection points: borderline of the park facing the northern frontage of the surrounding houses (H-1), a permanent sunny area (H-2), a permanent shady area (H-3), and borderline of the park facing to the southern frontage of the houses (H-4). The soil moisture detection points were very close to the soil temperature detection points. This means that the soil moisture was measured along a circle in which the center was the soil temperature detection point, and its radius was about 20 cm. According to this approach, we measured the moisture content in five different points, and we considered the average of the five measurements.

Applicability of the soil moisture meter was strongly related to the amount of available liquid water in the soil. It means that when the soil was dry or frozen, the sensor wand could be hardly pushed into the soil, or it became impossible. This physical limitation could be so serious, that gaps appeared in the data series.

Although not very apparent from the data presented here, the relationship between these two factors (air temperature and amount of water used for irrigation) probably works both ways. This means that low soil moisture content leads to a higher temperature, because of the lack of the cooling effect (*Al-Kayssi*, 1990). In addition, high temperature undoubtedly accelerates soil drying, resulting in lower soil moisture content. On the other hand, soil moisture came to its minimum during fall 2018, the soil moisture detected at the 4 detection points was 0%, 7.84%, 0%, and 0.56%, respectively (*Fig. 3*). The high soil moisture content among the 4 mentioned points was measured at the sunny point (H-2), due to its exposed position to fall precipitation and with no vegetation cover.

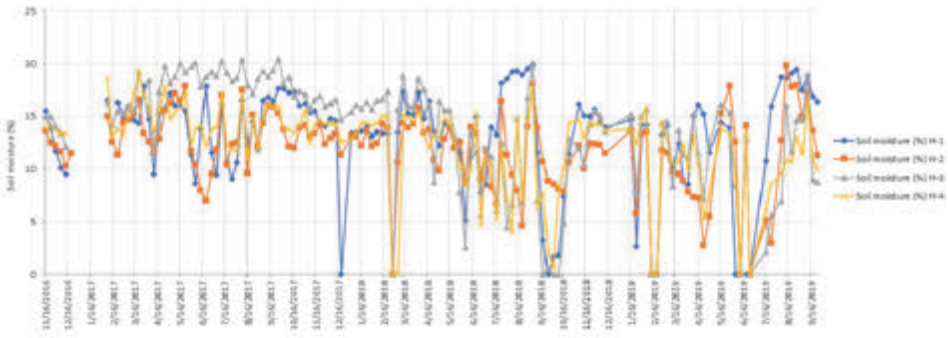

Fig. 3: Changes in soil moisture, 5 cm below soil surface at the Honvéd square in Budapest.

Soil moisture is an important control on heat and water transfer between the land and atmosphere, which in turn affects the development of extreme heat events (*Vogel et al*., 2018). In fact, the soil moisture in the 4 detection points is different especially during summer (see *Fig. 3*). However, the soil moisture at the sunny detection point is more influenced by solar radiation, even during the winter, and the persistence of soil moisture at the sunny detection point was slightly lower than at the shady detection point.

It is obvious that soil temperature and soil moisture are not independent of each other. Analysis of the intrinsic connection between soil temperature and soil humidity can help to understand the possible water management interactions in the park. In other words, soil moisture affects the water supply of the vegetation.

3.2. Analysis of the automated soil temperature detection at the Honvéd square

The air temperature was only measured on a weekly basis in our research (*Fig. 2*). As we mentioned, the soil temperatures at each detection point were measured by automated instruments, as well, at different depths of 0, 5, 10, 20, 30, 50, 100, 200 cm below the surface. We marked the sensors in the different depths, as T1, ..., T8, where T1 belongs to the deepest detection (200 cm), T2 to 100 cm, T3 to 50 cm, ..., and T8 to 0 cm (surface).

The sensors recorded data every hour and were stored in onboard memory. Then, the stored data was read out by a laptop on the spot. The soil temperature was measured for 135 days, 7 hours, from December 12, 2018 at 15:00 UTC to July 30, 2019 at 08:00 UTC. Due to unexpected technical reasons, the detection instrument H-4 had to be replaced by a new one (called H-plus), and the start of the measurement began on January 17, 2019 at 10:00 UTC. Other technical problems also happened during the detection period. The H-2 detection measurement records had multiple abrupt drops of temperature during the warmer months. These errors are so strong and frequent that they reached the 0 °C – which means that the data was not usable for the period in question (*Fig. 4*).

This phenomenon does not exist in plots of H-1, H-3, and H-plus. After consultation with the expert who built the instruments, he believed that the data collector device had some problem when the outer temperature exceeded a threshold value. This is why we ignored to use this data series in the analyses.

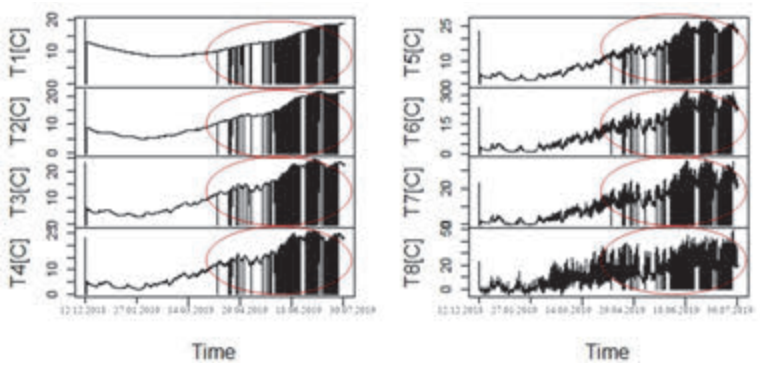

Fig. 4. Technical problems at the measurement point H-2: A severe drop in temperature can be observed during summer 2019 (problems are indicated by red ellipses)

3.2.1. Annual scale

Based on *Table 2*, the minimum and maximum soil temperatures at the different depth at H-1 were -4.99 °C (December 20, 2018, midnight, surface), and 34.52 °C (July 1, 2019, 17:00, surface). At H-3 it was -4.16 °C (December 20, 2018 from midnight until 01:00) and 32.78 °C (July 1, 2019 at 17:00). Finally, at H-plus it was measured as -2.02 °C (January 23, 2019 at midnight) and 32.2 °C (June 13, 2019 at 15:00).

Table 2. Summary of the statistics related to the annual automated soil temperature detections at the park of Honvéd square, Budapest

	Minimum	**Maximum**	**Median**	**Mean**	**Standard deviation**
H-1	-4.99	34.52	11.08	11.00	6.71
H-3	-4.16	32.78	11.41	11.12	6.68
H-plus	-2.02	32.2	12.66	12.79	6.49

Results from soil temperature sensors have revealed (*Fig. 5*) that the highest and lowest measured soil temperatures occur at the surface, and fluctuations in soil temperature are more frequent in the topsoil than in the lower soil layers.

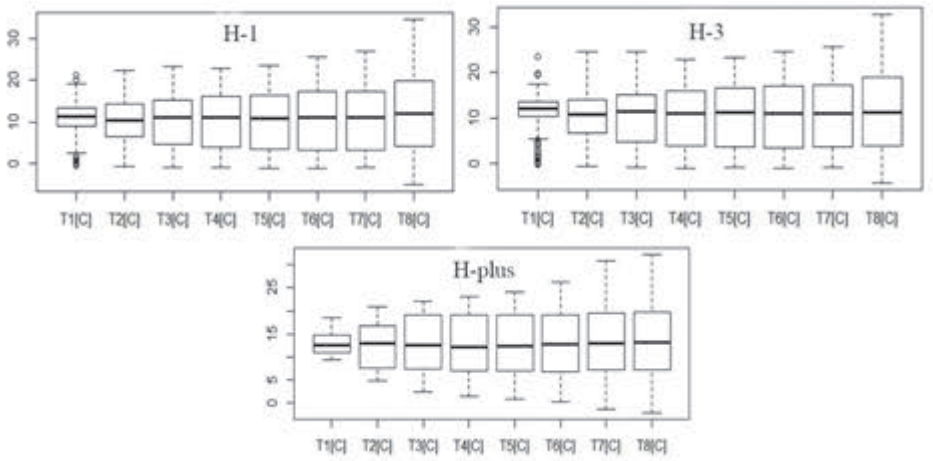

Fig. 5. Box and whisker plot of the annual soil temperature at the different depths (T1 – 200 cm, T2 – 100 cm, T3 – 50 cm, T4 – 30 cm, T5 – 20 cm, T6 – 10 cm, T7 – 5cm, and T8 – 0 cm).

The annual mean and standard deviation of the soil temperature at the different depths were 11.00 °C and 6.71 °C for H-1, 11.12 °C and 6.68 °C for H-3 and 12.79 °C and 6.49 °C for H-plus. Also, the median was 11.08 for H-1, 11.41 for H-3, and 12.66 for H-plus.

We used boxplots to display the soil temperature data distributions, according to the different depths (*Fig. 5*). The boxplots provide additional landmarks describing the distribution of the soil temperature in the different depths (the vertical axis of the box plot is read from the lowest value at the bottom to the highest value at the top). The median relating to the soil temperature is between 11.08 and 12.66 (horizontal line inside the box). The upper and lower ends of the boxes are the hinges (the approximate upper and lower quartiles) of the soil temperature distribution. The vertical lines from the ends of the boxes connect the extreme data points to their respective hinges. The distance from the observation with the smallest value to the largest value represents the range of the data. This is the distance from the left end of the lower whisker to the right end of the upper whisker.

In the 3 boxplot graphs (*Fig. 5*), we can observe different sizes of the boxes, where the deepest depth (T1), have comparatively the shorter plot, while the surface detection (T8) have the taller plot. This indicates that there are minor changes in the soil temperature at 200 cm depth through the year compared to the significant ones detected on the surface. This should make sense, since the surface soil temperature is changing within wide range, resulting lower temperature in winter and higher in summer, than the temperature at the bottom, in the same seasons.

Over the detected year, the soil temperature was aggregated into hourly values. When the soil temperature was consistently below 0 °C, it was documented as frozen condition of the soil, while above 0 °C, it was registered as thawed condition of the soil (*Fig. 6*).

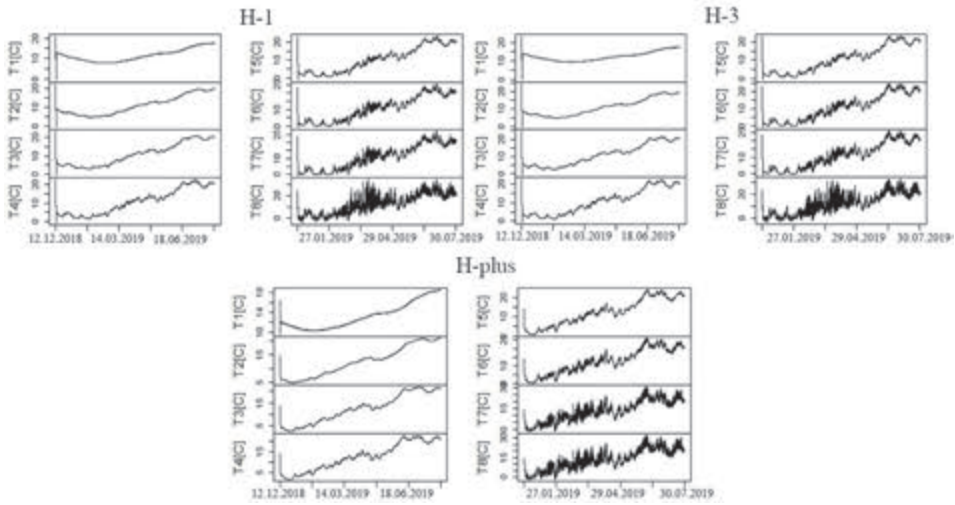

Fig. 6. Time series of the soil temperature at the different layers, at the 3 detection points of the park (T1 – 200 cm, T2 – 100 cm, T3 – 50 cm, T4 – 30 cm, T5 – 20 cm, T6 – 10 cm, T7 – 5cm, and T8 – 0 cm)

In addition to the meteorological factors, the vegetation cover may moderate the response of soil temperature sensors (*Fiebrich* and *Crawford*, 2001). Vegetation plays a role in reducing the heat energy conversion and has a direct effect on the temperature of the soil in different layers (*Chai et al*., 2008). *Chai et al*. (2008) continue by stating that vegetation retains the moisture through the roots contained in the soil, thereby reducing soil evaporation and water loss. They also mention that the degraded vegetation would weaken the cooling impact of plant transpiration on soil temperature and increase water dispersion, ultimately leading to a reduction in soil temperature in deeper depths. According to these cited findings, the bare soil surface of H-2 point retains less soil moisture content than the shady point (H-3), because of the exposed position against the direct heat radiation of the Sun.

A soil-warming trend could be observed during the summer season, but this trend has more "faces" according to the depth. It means, that going by the depth, this change becomes slower, and has less fluctuation (smaller amplitude), compared to the layers closer to the surface. The trend reverses in winter, but the higher temperature fluctuation belongs to the surface layers again (*Fig. 6*). This

implies that the warming occurring in the surface layers needs some time to reach the deeper soil layers, but once warmed, the deeper layers remain warmer through the year. Nevertheless, in this time-shifted warming up process, the soil moisture content can play a key role, since dry soil warms up faster than a wet one (*Javier, et al.*, 2018).

However, change of the temperature in the soil profile with the seasons are also interesting, and can be observed in our data. In spring and summer, soil temperature starts to decrease with depth, because the surface layers are able to warm up faster, than the deep layers. In winter, soil temperature increases with soil depth, because the surface soil temperature drops more quickly. In general, the closer we are to the surface, the higher is the rate of temperature change. This process has two peaks throughout the year: a positive one in the warm half-year, and a negative one in the cold half-year. It means that the response of surface soil temperature to the effects of the everyday weather conditions is much more pronounced than that of the deep layers.

The time-shifted, profile depth-linked behavior of the soil temperature has a connection with the seasonal change of the air temperature, as a factor of the local meteorological, but also, regional climatic factor (*González-Rouco et al*., 2003, *Zhang et al.,* 2005).

According to *Brady* and *Weil* (2013), the lower temperatures of water-saturated soil are due, in part, to water evaporation – a process that consumes a lot of heat – and, in part, to high specific heat in water-saturated soil. Keeping in mind that the park is irrigated, this process has an important role in the analysis of the soil temperature at the different depths. However, role of irrigation is also interesting, since it is a seasonal impact, mainly concentrating on the summer (warm half-year). Furthermore, effect of irrigation can be traced much more in the surface layers, than in the deeper ones (*Abdelaziz, et al*., 2022) Furthermore, according to these authors, soil temperature in the few centimeters above saturated soil is usually 3 to 6 °C lower than that of dry soil or slightly moist soil. In studies performed by *Diniz et al.* (2013), the months of lower soil temperatures were precisely the months with higher rainfall.

3.2.2. At a level scale

In this study, it was interesting to analyze the behavior of the soil temperature in the different depths, namely at 0, 5, 10, 20, 30, 50, 100, and 200 cm below the surface. The drillings to install the sensors did not reach the groundwater.

The climate variation in different seasons and months results in a corresponding variation in soil temperature in different depths. The highest, but also the lowest soil temperature was recorded at the 0 cm depth (*Figs. 5* and *6*). The observed data were analyzed for the period from December 12, 2018 to July 30, 2019.

Fig. 7 shows the variation of the hourly mean soil temperature at different depths at three detection points. (*Fig. 6* displays the three detection points' temperature curves, while *Fig. 7* displays the different depth's temperature at the three detection points.) According to the data series, the soil temperature in the Honvéd square park reaches both of its maximum and minimum temperatures at the surface, with 34.52 °C and -4.99 °C, respectively, during July and December. However, going to the depth, more major features can be observed relating to the change of the soil temperature. a.) The amplitude of the change is decreasing with the depth. b.) There is a time shifting in occurrence of the maximum and minimum values: the bigger is the depth, the time shifting will be higher. c.) The maximum temperature values will be lower and lower toward to the deep than the surface temperature, and the minimum values will be higher with the increasing depth. The temperature delay from surface to deeper layers shows that the heatwave requires a certain time to spread in the soil downward because of slow heat conduction capacity through the vertical soil profile, as mentioned above.

Referring to *Figs. 6* and *7,* the maximum soil temperature occurs in July (when cooling demand is high) at a depth of 0 cm (surface), but it also occurs in January at a depth of 100–200 cm below the surface. It clearly shows that the heat transport needs time to reach the deep layers. However, we can also interpret this phenomenon as a "virtual" movement of a specific temperature value along the soil profile.

Characteristic trends were found in December and January at the three different detection points (*Fig. 7*). The most common trend is that the soil temperature at 200 cm below surface is higher than the average of the seven upper soil layers for the three different detection points. This is because of the downward spread of the stored heat energy from the soil surface, and the less seasonal loss with the growing depth.

Trends in change of soil temperatures at 0, 5, 10, 20, 30, 50, 100, 200 cm depths were also analyzed. There was a significant positive trend with soil temperatures in spring and summer means, but not for the winter and annual means (*Fig. 7*). A positive, warming trend with time in soil temperature was detected at all depths below 5 cm, which associated with trend in air temperatures (and so the incoming radiation) over the same period.

As it was shown in the preceding section, temperatures are increasing at every specific level of soil column during the investigated period (from the winter half year toward the summer half year; see *Fig. 7*), and this trend persists in all of the detection points and months to a varying degree, especially during summer months. A plausible explanation for this observation is that soil and atmospheric heat exchange is the fastest at the surface layers (*Hu* and *Feng*, 2004). As explained by *Bai* (2009), heat loss is amplified by surface evaporation leading to cooler soil temperatures within the first 0 to 30 cm depth. Water accumulating in lower depths tends to retain heat compared to the upper surface

layers where evaporation accelerates cooling (*Hu* and *Feng* 2004). *Jacobs et al.* (2011) reported that lower soil depths, from 100 cm up to 200 cm, are significantly warmer than layers close to the surface during the cold season.

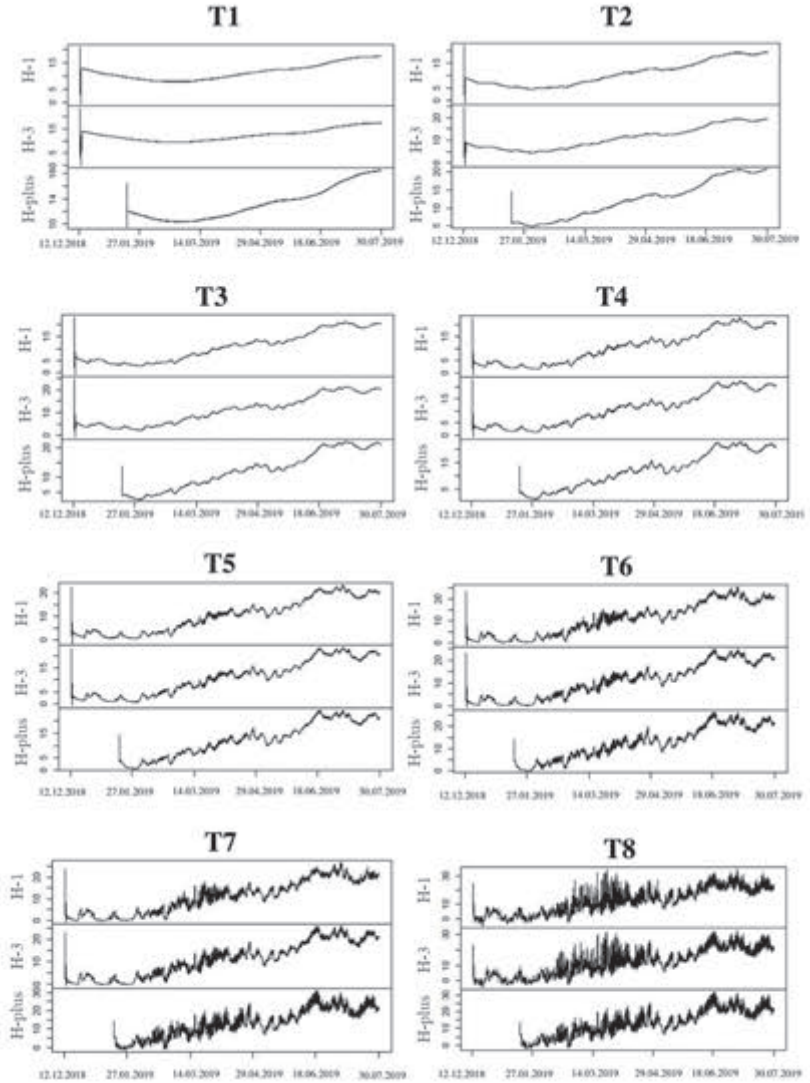

Fig. 7. Time series of the different depths of the automated soil temperature (T1 –200 cm, T2 – 100 cm, T3 – 50 cm, T4 – 30 cm –, T5 – 20 cm, T6 – 10 cm, T7 – 5 cm, and T8 – 0 cm).

The thermal amplitudes studied in the soil for both the hourly and daily mean data showed lower soil temperature variation with increasing depth, regardless of the external variables that affect the increase or decrease in heat emission from the soil.

4. Conclusions

Soil temperature varies from month to month as a function of incident solar radiation, rainfall, seasonal swings in overlying air temperature, local vegetation cover, type of soil, and underground depth. However, it can be also seen, that the effect of the meteorological factors (especially of the temperature) time-shifted with the increasing depth of the soil column.

The stable observable differences among the measurement points within the park indicate that the natural processes in the park are differentiated. This clearly highlights importance of a differentiated park management practice, in terms of a better planned irrigation concept, and preserving of soil moisture by covering the seasonally bare surface (e.g., by mulch).

Due to the much higher heat capacity of soils relative to the air and the thermal insulation provided by vegetation and surface soil layers, seasonal changes in soil temperature deep in the ground are much less than close to the surface and lag significantly behind seasonal changes in overlying air temperature. Thus, by summer, soil temperature in the depth remains cooler than the temperature of the overlying air, and it acts like a natural sink for removing heat from the built and natural environment. This suggests that the heat capacity and speed of heat conductivity of the soil are important factors. This delayed, time-shifted reaction of the soil to the air temperature can be true much more in the deeper parts of the soil section, than in the surface, or even the whole soil column.

Furthermore, a decrease in soil temperature values may be explained by the effect of precipitation on heat conductivity in the soil. When solid particles are surrounded by water, there is an effective increase in the contact surface capable of conduct heat, in addition to the mass flow of soil water. Therefore, thermal conductivity rises quickly and significantly (*Prevedello*, 2010).

Our results have highlighted, that meteorological factors, primarily air temperature and precipitation play a key role for the soil system, as they will influence the soil moisture and temperature data series, producing a seasonal, periodical variability. Effect of these meteorological factors occurs differently according to the depth, so processes of change of the moisture content and temperature show a definite direction at different depths through a year, producing a kind of yearly evolutionary pattern in the data. Soil temperature as a function of time, location, and depth is an important parameter in agronomic, geo-environmental, and geothermal energy applications. In the study, the

automated soil temperature detection highlights that the depth significantly influences the soil temperature at the Honvéd square park. More precisely, the amplitude of the seasonal soil temperature changes is decreasing with going to the deep. In addition, the daily temperature changes can be traced only in the layers close to the surface, so the daily change of the soil temperature is shading with going to the deep. Under 100 cm below the surface, the soil temperature is relatively constant. It was proved that not only do deeper soils undergo less drastic seasonal temperature fluctuations but also the changes taking place lag further behind those of shallower soils.

Our results also indicate that the spatial heterogeneity of urban parks can play a significant role in their sensitivity and alleviating capacity regarding the urban heat island effect. In addition, an important consequence of our results is to re-think the daily park maintenance practice, with differentiating the patterns of irrigation, even within a small urban park.

Acknowledgements: This material is based upon work supported by the former Mining and Geological Survey of Hungary. István Waltner's contribution was supported by Project no. FK 124803, implemented with the support provided from the National Research, Development and Innovation Fund of Hungary, financed under the FK_17 funding scheme.

References

Abdelaziz, M.O., Nehad, D., Adel, H.E., Salah, E., Mayadah, W F., Aitazaz, A.F., and *Zaher, M.Y.,* 2022: Effects of Irrigation Method and Water Flow Rate on Irrigation. *Agricult. J. 12(8),*1164. https://doi.org/10.3390/agriculture12081164

Al-Kayssi, A.A.-K. ,1990: Influence of soil moisture content on soil temperature and heat storage under greenhouse conditions. *J. Agricult. Engin. Res. 45*, 241–252. https://doi.org/10.1016/S0021-8634(05)80076-9

Angel, S., Sheppard, S., and *Civci, D.,* 2005: The Dynamics of Global Urban Expansion. Washington D.C., Transport and Urban Development Department: The World Bank Report. http://citeseerx.ist.psu.edu/viewdoc/download?doi=10.1.1.309.2715&rep=rep1&type=pdf

Bai, Y., 2009: Distribution of Soil Temperature Regimes and Climate Change in the Mojave Desert Region. University of California Riverside: Electronic Theses and Dissertations.

Bowler, D., Buyung-Ali, L., Knight, T., and *Pullin, A.,* 2010: Urban greening to cool towns and cities: A systematic review of the empirical evidence. *Lands. Urban Plan. J. 11*, S147. https://doi.org/10.1016/j.landurbplan.2010.05.006

Brady, N., and *Weil, R.,* 2013: Elementos da natureza e propriedades dos solos (Elements of nature and soil properties: Bookman.

Brown, R. and *Gillespie, T.,* 1995: Microclimatic landscape design: creating thermal comfort and energy effciency. Wiley, Hoboken: John Wiley and Sons.

Burgess, J., Harrison, C., and *Limb, M.,* 1988: People, parks and the urban green: a study of popular meanings and values for open spaces in the city. *Urban Stud. J. 25*(6), 455–473. https://doi.org/10.1080/00420988820080631

Chai, W., Wang, G., Li, Y., and *Hu, H.,* 2008: Response of soil moisture under different vegetation coverage to precipitation in the headwaters of the Yangtze River. *J. Glaciol. Geocryol. 30*, 329–337.

Conway, H., 2000: Parks and people: the social functions. In: Woudstra. The Regeneration of Public Parks. https://doi.org/10.4324/9780203857540

Davies-Colley, R., Payne, G., and *Van Elswijk, M.,* 2000: Microclimate gradients across a forest edge. *New Zealand J. Ecol. 24*(2), 111–121. http://www.jstor.org/stable/24054666

Demuzere, M., Orru, K., Heidrich, O., Okazabal, E., Geneletti, D., Orru, H., Bhave,AG., Mittal, N., Feliu, E., Faehnle, M., 2014: Mitigating and adapting to climate change: Multi-functional and multi-scale assessment of green urban infrastructure. *J. Environ. Manage. 146*, 107–115. https://doi.org/10.1016/j.jenvman.2014.07.025

Diniz, J., Carneiro, R., Alvino, F., Sousa, E., and *Sousa, J.,* 2013a: Avaliação do comportamento térmico diário do solo de Campina Grande-PB (Evaluation of the daily thermal behavior of the soil of Campina Grande-PB: *Ravistas Agropecuária Científica no Semiárido (Scientific Agriculture in the Semi-arid Region Journal), 9*, 55–60. https://doi.org/10.30969/acsa.v9i2.372

Erell, E., Pearlmutter, D., and *Williamson, T.,* 2011: Urban Microclimate: Designing the Spaces between Buildings. Earthscan. London. https://doi.org/10.4324/9781849775397

Fiebrich, C. and *Crawford, K.,* 2001: The Impact of Unique Meteorological Phenomena Detected by the Oklahoma Mesonet and ARS Micronet on Automated Quality Control. *Bull. Amer. Meteorol. Soc. 82*, 2173–2188. https://doi.org/10.1175/1520-0477(2001)082<2173:TIOUMP>2.3.CO;2

Gehl, J. and *Gemzoe, L.,* 2001: New City Spaces. The Danish Architectural Press.

González Rouco, J., Von Storch, H., and *Zorita, E.,* 2003: Deep soil temperature as proxy for surface air-temperature in a coupled model simulation of the last thousand years. *Geophys. Res. Lett. J., 30*(21). https://doi.org/10.1029/2003GL018264

Grahn, P., 1985: Man's Needs for Urban Parks, Greenery and Recreation. Institute for Landscape Planning. Alnarp: Swedish Agricultural University.

Honjo, T., 2009: Thermal comfort in outdoor environment. *Glob. Environ. Res. J. 13*, 43–47.

Hu, Q. and *Feng, S.,* 2004: A Role of the Soil Enthalpy in Land Memory. *Amer. Meteorol. Soc. J., 17*, 3633–3643. https://doi.org/10.1175/1520-0442(2004)017<3633:AROTSE>2.0.CO;2

Jacobs, A., Heusinkveld, B., and *Holtslag, A.,* 2011: Long-term record andanalysis of soil temperatures and soil heat fluxes in a grassland area, The Netherlands. *Agric. Forest Meteorol., 151*(7), 774–780. https://doi.org/10.1016/j.agrformet.2011.01.002

Javier, L.-P., Manuel, P., Carlos, L.-F., and *Susanne, S.,* 2018: How do Soil Moisture and Vegetation Covers Influence Soil Temperature in Drylands of Mediterranean Regions? *Water J. 10*(2), 1747. https://doi.org/10.3390/w10121747

Kalnay, E. and *Cai, M.* (2003: Impact of urbanization and land-use change. *Nature 423*(6939), 528–531. https://doi.org/10.1038/nature01675

Kong, F., Yan, W., Zheng, G., and *Yin, H.,* 2016: Retrieval of three-dimensional tree canopy and shade using terrestrial laser scanning (TLS) data to analyze the cooling effect of vegetation. *Agric. Forest Meteorol. 217*, 22–34. https://doi.org/10.1016/j.agrformet.2015.11.005

Konijnendijk, C., Annerstedt, M., Nielsen, A., and *Maruthaveeran, S.,* 2013: Benefits of Urban Parks – A systematic review. A Report for IFPRA.

Li, Y., Kang, W., Han, Y., and *Song, Y.,* 2018: Spatial and temporal patterns of microclimates at an urban forest edge and their management implications. *Environ. Monitor. Assess. 190*(2), 93. https://doi.org/10.1007/s10661-017-6430-4

Loures, L., Santos, R., and *Panagopoulos, T.,* 2007: Urban Parks and Sustainable City Planning-The Case of Portimão, Portugal. *WSEAS Transact. Environ. Develop. J. 3*.

Mahmoud, A., 2011: Analysis of the microclimatic and human comfort conditions in an urban park in hot and arid regions. *Build. Environ. J. 46* (12), 2641–2656. https://doi.org/10.1016/j.buildenv.2011.06.025

Oké, T., 1981: Canyon geometry and the nocturnal urban heat island: comparison of scale model and field observations. *Int. J. Climatol. 1*, 237–254. https://doi.org/10.1002/joc.3370010304

Prevedello, C., 2010: Energia térmica do solo (Soil thermal energy). Sociedade Brasileira de Ciência do Solo (Brazilian Society of Soil Sciences).

Stępniewska, M., 2021: The capacity of urban parks for providing regulating and cultural ecosystem services versus their social perception. *Land Use Policy J. 111*, 105778. https://doi.org/10.1016/j.landusepol.2021.105778

Steward, I. and *Oké, T.,* 2012: Local climate zones for urban temperature studies. *Bull. Amer.Meteorol. Soc. 93*, 1879–1900. https://doi.org/10.1175/BAMS-D-11-00019.1

Susca, T., Gaffin, S., and *Dell'Osso, G.,* 2011: Positive effects of vegetation: Urban Heat Island and green roofs. *Environ. Pollut. J. 159*, 2119–2126. https://doi.org/10.1016/j.envpol.2011.03.007

Thorsson, S., Lindqvist, M., and *Lindqvist, S.,* 2004: Thermal bioclimatic conditions and patterns of behaviour in an urban park in Göteborg. *Int. J. Biometeorol. 48*(3), 149–156. https://doi.org/10.1007/s00484-003-0189-8

United Nations, 2014: Transforming our World: The 2030 Agenda for Sustainable Development.

USEPA, 2017: United States Environmental Protection Agency (), Office of Water: Green Infrastructure in Parks: A Guide to Collaboration, Funding, and Community Engagement.

Venables, W.N., Smith, D.M. and the R Core Team, 2023: An Introduction to R – User manual, p. 105. https://cran.r-project.org/doc/manuals/r-release/R-intro.pdf

Vogel, M., Zscheischler, J., and *Senevirante, S.,* 2018: Varying soil moisture–atmosphere feedbacks explain divergent temperature extremes and precipitation projections in central Europe. *Earth Syst. Dynam. J., 9*, 1107–1125. https://doi.org/10.5194/esd-9-1107-2018

Zhang, Y., Chen, W., Smith, S., Riseborough, D., and *Cihlar, J.,* 2005: Soil temperature in Canada during the twentieth century: Complex responses to atmospheric climate change. *J. Geophys. Res.: Atmospheres, 110*(D3), D03112. https://doi.org/10.1029/2004JD004910

DOI:10.28974/idojaras.2024.3.4

IDŐJÁRÁS

Quarterly Journal of the HungaroMet Hungarian Meteorological Service
Vol. 128, No. 3, July – September, 2024, pp. 345–366

The influence of rural areas transformation on the urban heat islands occurrence – Tourist center Zlatibor case study

Ljiljana Mihajlović [1, *], **Ivan Potić** [2], **Miroljub Milinčić** [3], and **Dejan Đorđević** [4]

[1] *Faculty of Geography, University of Belgrade*
Belgrade, Serbia
[2] *Military Geographical Institute "General Stevan Bošković"*
Belgrade, Serbia
[3] *Faculty of Geography, University of Belgrade*
Belgrade, Serbia
[4] *Military Geographical Institute "General Stevan Bošković"*
Belgrade, Serbia

* *Corresponding Author E-mail: ljiljana.mihajlovic@ gef.bg.ac.rs*

(Manuscript received in final form August 4, 2023)

Abstract— As urbanization continues to increase, changes in the ecological characteristics of urban areas are becoming more reasonable to meet the needs of a growing population. However, the profound impact of human-induced urban pressures on land, often called the "billing impact", is strongly emphasized in research publications. In many cases, contemporary anthropogenic processes alter the dynamics of environmental functions in complex ways. Urban regions meet a particular climate regime characterized by increased air temperatures compared to peripheral areas and a significant reduction in wind speed, attributable to the interaction of natural and anthropogenic factors. An urban heat island (UHI) occurs when the air above populated areas heats up additionally, causing air to flow from the site's edges to its center and creating a heat dome. This study reveals the influence of urbanization on microclimatic changes, encompassing increased evapotranspiration, altered vegetation cover, and temperature fluctuations. The results illustrate environmental transformations caused by abrupt and unregulated urbanization in the mountainous area of Zlatibor, Serbia, a trend that has intensified over the past decade.

Key-words: image analysis, GIS analysis, landsat, multispectral imagery, thermal infrared bands, land surface temperature, actual evapotranspiration

1. Introduction

Urbanization presents activities to enhance underdeveloped urban regions or create new infrastructure in undeveloped areas. The primary objective of these activities is to provide enhanced quality of life for the population. These processes frequently lead to a shift in the operational dynamics of the settlements. Contemporary society and lifestyle demands drive the significant conversion of nature, especially vegetated areas (*Grădinaru et a*l., 2020; *Tosic* and *Obradovic*, 2003). The interaction between nature and society forms an organically linked system, with the ecological characteristics of the resulting urbiocoenoses primarily determined by the degree of artificial pressure exerted on nature in urbanized regions. Such characteristics distinguish them from the original biogeocoenoses. As the biosphere transforms into the biotechnosphere, it becomes crucial to study one of the most significant thermodynamic characteristics of the biosphere and its components (*Vukoičić et al.*, 2023). The community's social organization and the effective management of social processes influence urbanization's pace, form, and characteristics. Urbanization is a process characterized by a substantial aggregation of activities within regions designated for priority development (*Živanović et al*., 2021). One of the vital material outcomes of modern urbanization is the creation of vast urban regions, a conglomeration of interconnected suburban villages, forming a complex dynamic system.

Zlatibor Mountain is a popular tourist destination within the Dinaric Alps Mountain range in the western part of Serbia. Famous for its green forests, pristine rivers, and attractive landscapes, the mountain of Zlatibor serves as a sanctuary for those who appreciate the natural world and engage in outdoor pursuits. It provides a multitude of opportunities for activities including, but not limited to, hiking, skiing, cycling, and fishing (*Pecelj et al.*, 2017). Furthermore, with its attractive natural features and traditional values combined with modern urban development trends, Zlatibor Mountain is an area that urbanizes remarkably quickly and is an exceptional subject for this study.

The study and understanding of the surface urban heat island (SUHI) have far-reaching implications across various fields. In climatology, it helps us understand the impact of urbanization on local and global climate patterns (*Zhou et al.*, 2015). In geography, it aids urban planning and the development of strategies to mitigate heat-related health risks (*Tan et al*., 2010). In tourism, SUHI influences tourist behavior and preferences, potentially impacting the local economy (*Zhou et al.*, 2016). Researchers extensively study the SUHI phenomenon using remote sensing technology, which provides a comprehensive spatial and temporal understanding of UHIs (Zhou et al., 2016). For instance, satellite data enables the quantification of SUHI effects across various urban forms and climatic conditions (*Zhou et al.*, 2014). The rise in global urbanization and its associated environmental and health challenges highlight the importance

of SUHI research. Therefore, it continues to be a crucial study area in urban climatology and related fields.

Researchers can study the UHI-derived phenomena by analyzing the air temperature observed at urban and rural weather stations and using land surface temperature data obtained through remote sensing (*Imhoff et al*., 2010). However, studying the UHI phenomenon in regions with insufficient weather stations can be challenging. With its extensive area synchronization and spatial coverage advantages, remote sensing data has become an effective tool for studying the UHI phenomenon (*Gallo et al*., 1993; *Gong et al.*, 2008; *Weng et al.*, 2004). The first use of the infrared thermal band from satellite imagery to study the UHI effect occurred in 1972 (*Rao*, 1972). Since then, remote sensing data and algorithms have been utilized and improved to examine the UHI effects (Cao et al., 2016; *Liu* and *Li*, 2018; *Stathopoulou* and *Cartalis*, 2007; *Tang et al.*, 2022). Analyses have been conducted on the scale of UHI phenomena and its spatiotemporal evolution features, considering its implications on diverse environmental factors. Additionally, researchers actively search for measures to mitigate its harmful effects (Chen et al., 2016; *Imhoff et al.*, 2010; *Priyadarsini et al*., 2008; *Stathopoulou* and *Cartalis*, 2007; *Streutker*, 2003; *Voogt* and *Oke*, 2003).

The formation of "heat islands" has several effects: a decrease in relative and absolute humidity, the emergence of a rising convection current, a decrease in wind speed, an increase in cloud cover and precipitation, an increase in the frequency of smog-like fog, and a decrease in solar radiation (*Mohajerani et al.,* 2017; *Pecelj et al.*, 2021). In addition to measuring the temperature of a given area, estimates of evapotranspiration (ETa) derived through remote sensing and global weather datasets provide valuable information about the existence of UHI. Such information proves useful for various applications, including calculating a basin's water budget, evaluating water consumption and crop yield, and monitoring drought conditions. The process of evapotranspiration is essential to understand the energy and water budgets of the planet, in addition to the carbon cycle. Acquiring a time series of spatially consistent, historical Landsat data for the entire world is a significant step forward in advancing scientific knowledge (*Sugiarto et al.*, 2021).

Heat domes, rarely exceeding 700 meters in height, intensify air pollution in cities and populated areas (*Lješević* and *Mihajlović*, 2020). Its distribution and strength depend on the size of the city, the area it occupies, the density of buildings, variations in air temperature and humidity, and differences in land use. The wind regime affects the extent and shape of the heat dome above the surface. At wind speeds between 10 and 15 m/s, a dome cannot exist (*Mohajerani et al*., 2017). Therefore, a wind of this speed cleans the air during the day more effectively than 20 times the air exchange (*Pecelj et al.*, 2010; 2017). However, even under these conditions, the dome can become a cloud of air pollution covering suburban areas (settlements, recreational areas, agricultural land, and others).

This study aims to delve into the impact of urbanization on the UHI and SUHI effects, with a particular emphasis on the Zlatibor Mountain region. Zlatibor Mountain, situated in the southwestern region of Serbia, extends from northwest to southeast, covering a vast area of approximately 1.015 km². It spans 55 km in length and 22 km in width, encompassing significant portions of the widespread Starovlaška plateau. The mountain shares its borders with the Kremna Valley to the northwest, the Sušica and Mačkatska areas to the north, the Murtenica Mountain to the southeast, and the Uvac River to the south. Additionally, a foothill connecting to Tara also forms a part of Zlatibor. Located at a distance of 230 km from the Serbian capital of Belgrade (*Fig. 1*), Zlatibor Mountain is accessible via the Zlatibor magisterial road, which serves as a crucial route connecting Belgrade to the Adriatic Sea coast.

Regarding tourism, Zlatibor is predominantly known for its central part – a spacious rolling plateau, about 30 km long and 12 km wide. Several peaks and tops, including Tornik, Čigota, Gradina, Čavlovac, Viogor, Crni Vrh, and the upper stream of the Sušica River, border this central area (*Stojsavljević et al.*, 2016). The research uses remote sensing data and other relevant datasets to analyze the changes in land surface temperature and evapotranspiration rates and their implications on the local climate and environment. The findings from this study enrich the growing body of knowledge on UHI, and provide valuable insights for urban planning and environmental management in the face of rapid urbanization.

2. Materials and methods

2.1. Study area

The initial hypothesis of this article is that the urban heat islands have emerged after intensive and excessive construction in the tourist center of Zlatibor. This tourist center, located in the western part of Serbia, is near Užice (*Fig. 1a*) and Čajetina town (*Fig. 1c*). The study area includes the surrounding area of the newly built urban environment in the tourist center (according to the 2022 situation). The study area extends to 4,847,038.68 m N, 391,257.58 m E, and 4,838,842.59 m N, 399,385.45 m E (*Fig. 1b*) and covers an area of 66.62 km^2. The urban part of the study area covers an area of 9.48 km^2 with a mean geographic center at 4,842,793.46 m N and 395,452.68 m N. The UTM34N projection provides all coordinates.

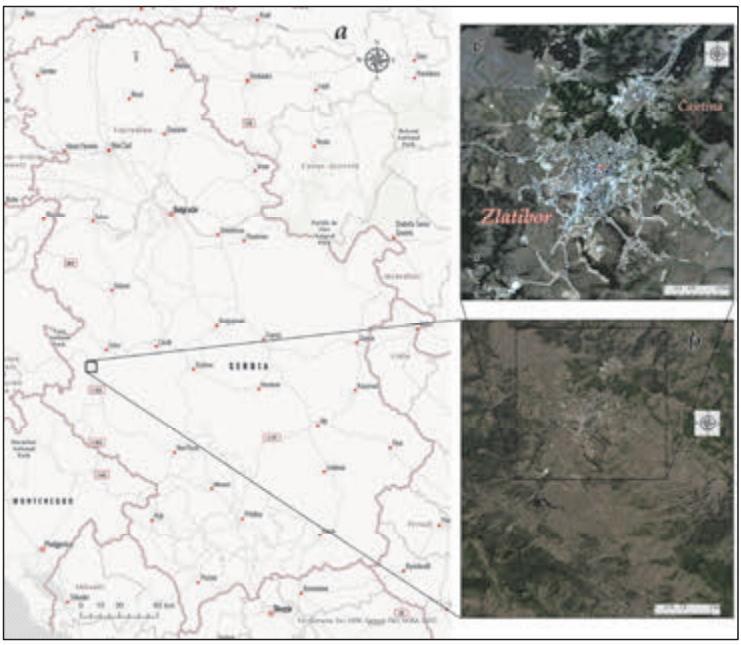

Fig. 1. Zlatibor's a) position within Serbia, b) the Area area of interest (AOI), c) urban part of AOI.. (*Engebretson*, 2020a; *Prostak*, 2023)

The tourist center of Zlatibor has undergone substantial urbanization, particularly in developing tourism infrastructure, over the past three decades. The region witnesses growth in hotels, restaurants, cafes, and other amenities, enhancing its appeal as a tourist destination (*Basarin et al*., 2018). This area lacks regulated urbanization, with individual houses making up most of the permanent residential space. However, collective housing is available in the tourist center of Zlatibor and in the municipal headquarters. The main issue is the high prevalence of temporary residences such as weekend houses and holiday homes. The 2011 census data reveals that the area contains 7,229 permanent and temporary dwellings, covering 637,182 m^2. The municipality undergoes the construction of approximately 654 new apartments annually, spanning a total area of 33,714 m^2. Owing to the high rate of residential construction, the number of built apartments per 1,000 inhabitants has experienced a steady increase since 2015 (*Republički zavod za statistiku Srbije*, 2023). This extensive and unregulated construction exerts significant pressure on the environment, while simultaneously, urbanization brings new job opportunities and stimulates economic growth in the region. Nevertheless, it has also upraised concerns about the impact of tourism on the environment, including waste management, water supply, and air temperature

increase. Despite these challenges, Zlatibor Mountain remains a popular tourist destination, combining natural beauty and modern amenities. The region continues to attract visitors from all over the world, seeking relaxation, outdoor activities, and a taste of Serbian culture.

Zlatibor's geological structure primarily consists of Zlatibor ultramafites, the Triassic sediments, and ophiolitic mélange in the eastern part of the area (*Dimitrijević,* 1996). Tertiary formations cover this area in some places, with a thin rim of Paleozoic bedrock. The Zlatibor Mountain area is part of the ophiolitic zone of the inner Dinaric Alps belt (*Vakanjac et al*., 2015). It is made up of Paleozoic phyllites, sandstones, and conglomerates, as well as Mesozoic rocks of the diabase-rose stone formation. Palaeozoic rocks comprise most of the geological structure, while Neogene sediments have been formed on land once inhabited by lakes.

The climate is moderately continental in the low, northern part of the region, but becomes sub-mountainous as altitude ascends. The average summer air temperature is about 25 °C, while winter air temperatures can drop to -5 °C. The yearly precipitation typically ranges between 700 and 900 millimeters (*Novković*, 2008).

The land cover of the study area presents a mix of barren, developed, forest, and herbaceous regions, with a minimal proportion of water bodies based on 2022 data (*Table 1*). The dominance of barren and developed lands may underscore prevailing environmental and anthropogenic factors influencing the landscape. Barren land is the most prominent class, covering most of the area. This category, often signifying a scarcity of vegetation, covers a substantial 52.16% of the total study area. The prominent presence of barren land suggests potentially harsh or unproductive environmental conditions. The second most widespread class is developed land, approximately 14.24% of the total study area. This classification typically refers to areas with a considerable human footprint, such as settlements, infrastructures, or extensively cultivated lands. The proportion of developed land might signal significant human activity or industrial influence. Forest and herbaceous classes encompass relatively similar areas. Forest land, indicative of areas dominated by trees and other woody plants, occupies 17.93% of the study area. However, herbaceous land, usually characterized by grasses, herbs, and other non-woody plants, accounts for 15.59% of the total study area. The presence of these classes suggests a balance of both woody and non-woody vegetated zones in the study area. Finally, the smallest class (water land), represents a minuscule 0.08% of the total study area. This diminutive portion implies that surface water bodies like lakes, rivers, or reservoirs are likely scarce within the study area.

Identifying and mapping UHI requires multiple inputs (*Fig. 2*). The process begins with analyzing meteorological data to verify the temperature change hypothesis and determine the critical point at which this phenomenon emerged. The next step involves scrutinizing satellite images and their related outputs (*Fig. 2*) for more precise information.

2.2. *Meteorological data*

The air temperature data used to create a database for this research are collected from meteorological statistical yearbooks of the Hydrometeorological Service of the Republic of Serbia for the Zlatibor meteorological station and the given climatological period. The research encompassed a complete climatological cycle of at least a 30-year time series and followed the World Meteorological Organization (WMO) guidelines.

From 1986 to 2022, air temperature (RHSS, 1987–2022) change is analyzed to determine the trend of mean August values and the threshold year, in which the mean monthly air temperature did not drop below 16 °C.

August is chosen as the warmest month of the year in the meteorological station Zlatibor, located within the settlement of Zlatibor at an altitude of 1,029 m.a.s.l. (RHSS, 1987–2022).

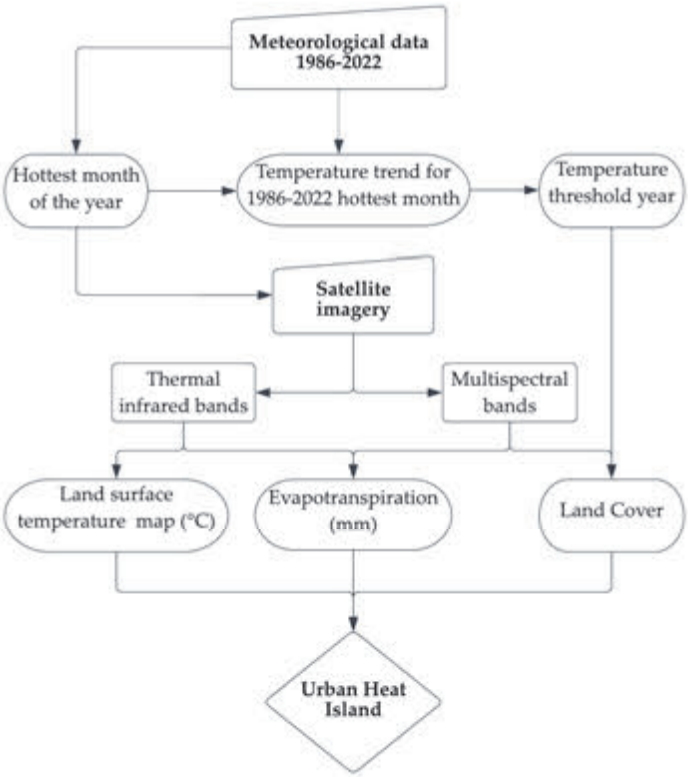

Fig. 2. Flow chart of urban heat island detection used in this research.

2.3. Satellite imagery processing

The creation of Landsat Level-2 science products involves using Collection 2 Level-1 inputs that do not exceed the 76 degrees Solar Zenith Angle limitation and include the necessary auxiliary input data to provide a scientifically credible solution (*Sayler et al*., 2022; *Sayler* and *Zanter*, 2021). The Version 1.5.0 of the Land Surface Reflectance Code (LaSRC) algorithm generates the Landsat 8/9 Operational Land Imager (OLI) surface reflectance products. (*Engebretson*, 2020a). The Landsat 4–5 surface reflectance products are created using the Version 3.4.0 Landsat Ecosystem Disturbance Adaptive Processing System (LEDAPS) algorithm (*Engebretson*, 2020b). The Landsat 4-9 surface temperature products are produced using the Landsat surface temperature algorithm Version 1.3.0, created in collaboration with NASA's Jet Propulsion Laboratory and Rochester Institute of Technology (*Cook*, 2014).

Land surface temperature (*LST*) products are measured in Kelvin (K) and generated with a 30-meter spatial resolution. Landsat Collection 2 Level-1 thermal infrared bands, TOA Reflectance, TOA Brightness temperature, ASTER Global Emissivity Database (GED) data, ASTER NDVI, and atmospheric profiles of geopotential height, specific humidity, and air temperature obtained from ASTER data are used to produce Landsat Level-2 Surface Temperature products (*Sayler et al*., 2022). The final step is to calculate the *LST* in °C (*Avdan* and *Jovanovska*, 2016):

$$LST = BT / \{1 + [(\lambda BT / \rho) \ln (LS\varepsilon)]\} \ , \tag{1}$$

where BT is at-sensor brightness temperature in °C, λ is the wavelength of emitted radiance (center wavelengths for Landsat TIR bands are: for Landsat 5 Band 6 value is 11.45, and for Landsat 8 Bands 10 and 11 values are 10.895 and 12, respectively (*Engebretson*, 2020b; *Sayler et al*., 2022)), $LS\varepsilon$ is the emissivity, and ρ is the density of air.

The amount of water vaporising from a surface due to evaporation and transpiration is called actual evapotranspiration (*ETa*), measured in millimetres (mm). ETa is derived from the Landsat Level-2 Surface Temperature products and uses a scene-based approach. The Landsat Surface Temperature is one of the variables provided in a surface energy balance model, along with other auxiliary data, to calculate the daily total of *ETa*, which is part of the product entitled Landsat Collection 2 Level-3 Provisional Actual Evapotranspiration Science (*Sayler* and *Glynn*, 2022). The robust model solves the surface energy balance equation for the latent heat flow to produce the Landsat C2 Provisional *ETa* products. This *ETa* computation uses a surface energy balance model built directly from the Operational Simple Surface Energy Balance (SSEBop) model (*Senay*, 2018; *Senay et al*., 2013, 2022, 2023). An SSEBop model is provided with

the Landsat C2 Level-2 Surface Temperature product and external auxiliary data to derive the daily total of *ETa.*

The SSEBop model is a parametric energy balance-based model that considers real *ET* to be the product of two independently estimated quantities: (1) *ET* fraction (*ETf*) and (2) the maximum *ET* under water-unlimited environmental circumstances *(ETr*) (*Senay et al*., 2023):

$$ETa = ETf \cdot ETr, \tag{2}$$

where *ETa* is the actual *ET* (mm) and *ETr* is the alfalfa-reference ("maximum/potential") *ET* (mm).

Land cover classification uses Landsat 5 and Landsat 8 (*Sayler* and *Zanter*, 2021) optical bands. Imagery from 3 different periods (initial 1986, threshold 2005, and final 2022) is acquired using USGS Earth Explorer (*U.S.G.S*., 2015) application. Five different classes are distinguished: 1) water, 2) developed, 3) forest, 4) herbaceous, and 5) barren land. Class "water" includes areas of open water, such as lakes, rivers, and ponds. Class "developed" includes areas developed for human use, such as residential, commercial, and industrial areas, and includes transportation infrastructure, such as roads, airports, and railroads. Class "Forest" includes areas dominated by trees (natural or planted forests). Forests can include a variety of tree species. The "herbaceous" class refers to areas dominated by non-woody plants, such as grasslands, fields, lawns, or other open areas. These areas may be natural or managed landscapes like parks or lawns. The "barren land" class refers to landscape areas with little to no plant life. This class could include deserts, rocks, sand, or other areas, where the soil is too poor to support much plant life. These areas are often devoid of human activity due to their harsh conditions. SVM classifier is employed in semi-automatic supervised object-based classification procedures using ArcGIS Pro (*Esri Inc*., 2023) to perform satellite image classification and obtain a land cover map for a specific year.

The SUHI effect is a significant environmental concern characterized by higher temperatures in urban areas than in rural ones. Human activities, urbanization, and modifying natural landscapes cause this phenomenon. The quantification of the SUHI effect is typically achieved by subtracting the rural temperature from the urban temperature (*Zhou et al.*, 2014), and in recent years, there have been several advancements in the methodologies used to study and mitigate the SUHI effect (*Almeida et al.,* 2022; *Bande et al*., 2022; *Fardani* and *Yosliansyah*, 2022).

3. Results

Fig. 3 presents the analysis of average August air temperatures over 37 years, from 1986 to 2022. The trendline reveals a consistent rise in these air temperatures. The data exhibits yearly variability, with the highest average temperature recorded in 2012 (21.00 °C) and the lowest in 1995 (15.40 °C). Some years, such as 1992, 1994, 2000, 2003, 2012, 2015, 2017, and 2019, have air temperatures above the average, while others, like 1987, 1991, 1995, 1997, 2002, 2005, and 2016, fall below the average.

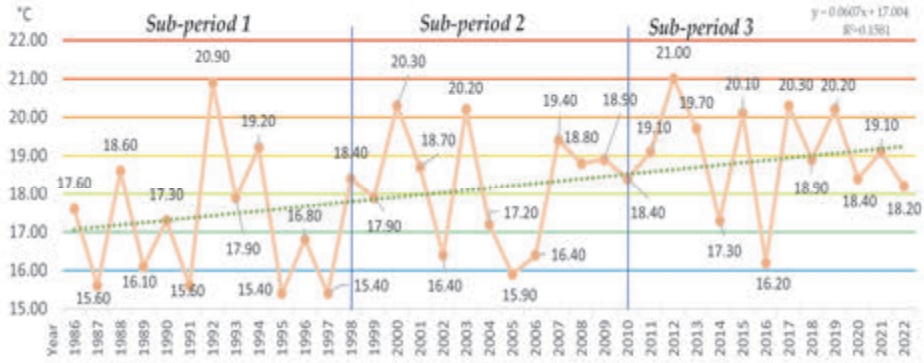

Fig. 3. Average August air temperatures (°C) in the period 1986–2022.

Overall, the data suggest some variability in August air temperatures from year to year, but the average air temperature over the 37 years is 17.96 °C.

Empirically, the air temperature data indicates that 2005 is a temperature threshold year suitable to present the studied area's mean urbanization state related to the temperature increase. The temperature threshold year is chosen by dividing the thirty-seven-year observation period into three sub-periods to compare the lowest monthly average temperatures (*Fig. 3*). The data shows that 2005 is the last year with an average monthly temperature below 16 °C. The given linear trend equation, $y = 0.0607x + 17.004$, indicates a positive linear relationship between the years (independent variable, x) and the average monthly air temperature in August (dependent variable, y) for the study area. The slope of the trend line (0.0607) suggests an annual increase in August air temperatures. Specifically, the average monthly air temperature for August tends to rise by approximately 0.0607 °C for each one-year increase. The equation suggests a long-term warming trend over the observed period, despite potential fluctuations from year to year. Thus, the evidence supports the assertion that there is an increasing trend in the August air temperatures for the observed period and study area. However, the coefficient of determination, $R^2 = 0.1581$, implies that

approximately 15.81% of the variance in the average monthly air temperature can be explained by the year in the context of this model. Therefore, a substantial portion of the variance (around 84.19%) is still unexplained by the linear model. This result suggests other factors influencing the average August air temperature beyond time (year). These factors could encompass various climatic or anthropogenic elements not accounted for in the simple linear model. R^2 of 0.1581 signifies that the model has successfully captured a significant portion of the variation in the data. It implies that a definite structure underlies the data, as elucidated by the model, even though the model does not account for a substantial portion of the variability.

The land cover classes information is provided in *Table 1* for three different years, 1986, 2005, and 2022, in terms of their areas and percentages for a wider study area (Figure 1c). *Table 1* shows that the class „developed" has increased its area significantly over time, with 9.48 km^2 in 2022, 4.68 km^2 in 2005, and 0.71 km^2 in 1986. Determined values compute the increasing trend between 1986 and 2022 for the class „developed". The calculated percentage increase is 1 233.8%.

Table 1. Land cover results for 1986, 2005, and 2022 for Zlatibor study area

Class name	Area 2022 (km^2)	2022 (%)	Area 2005 (km^2)	2005 (%)	Area 1986 (km^2)	1986 (%)
Water	0.05	0.08	0.01	0.02	0.02	0.03
Developed	**9.48**	**14.24**	**4.68**	**7.02**	**0.71**	**1.07**
Forest	11.94	17.93	9.97	14.98	15.15	22.75
Herbaceous	10.38	15.59	38.73	58.17	21.78	32.71
Barren	34.73	52.16	13.19	19.81	28.93	43.45
Total	**66.58**	**100.0**	**66.58**	**100.0**	**66.58**	**100.0**

The precise analysis of *LST* and *ETa* results includes only the area of Zlatibor's widest urbanization (*Fig 1c*, white outline) according to the 2022 classification (9.48 km^2), which are shown in *Table 2* and *3*.

The *LST* ranges from 15 °C to 40 °C. In 1986, the area covered at lower *LST* values, between 15 °C and 24 °C, is much smaller than in 2022, indicating a significant increase in urbanization or land use change. In 2022, most areas are covered by *LST* values between 27 °C and 35 °C.

In 2022, the most extensive part of the Zlatibor urban area (4.495 km^2) exhibits *ETa* values in the 2–3 mm range. The second most extensive area (2.646 km^2) presents *ETa* values of 1–2 mm, while the smallest area (0.009 km^2) shows ETa values greater than 4 mm. Conversely, in 1986, the most significant area (4.641 km^2) shows *ETa* values in the 2–3 mm range, and the second-largest area (3.159 km^2) presents *ETa* values in the 3–4 mm range.

Table 3 reveals that the area with ETa values in the 2–3 mm range is the largest in both 1986 and 2022, covering 4.641 km^2 and 4.495 km^2, respectively, indicating that this range of *ETa* values is the most frequent in the Zlatibor urban expansion area.

Table 3 also highlights that the area with *ETa* values in the 1–2 mm range expands from 1.527 km^2 in 1986 to 2.646 km^2 in 2022, suggesting an increase in vegetation cover in the Zlatibor urban expansion area, leading to higher evapotranspiration rates in this range.

Table 2. Land surface temperature coverage 1986–2022 for Zlatibor main urban area

Temperature (°C)	**Area 2022 (km^2)**	**Area 1986 (km^2)**
15	/	0.003
16	/	0.075
17	/	0.269
18	/	0.518
19	/	0.697
20	/	1.031
21	/	1.274
22	/	1.766
23	/	1.310
24	/	0.893
25	/	0.770
26	0.002	0.343
27	0.048	0.230
28	0.243	0.241
29	0.963	0.052
30	1.331	0.009
31	1.597	/
32	1.457	/
33	1.276	/
34	0.926	/
35	0.781	/
36	0.522	/
37	0.198	/
38	0.105	/
39	0.029	/
40	0.004	/
Total area	**9.482**	**9.482**

Table 3. Evapotranspiration coverage in the period 1986–2022 for Zlatibor urban expansion area

***ETa* range (mm)**	**Area 2022 (km^2)**	**Area 1986 (km^2)**
0–1	0.325	0.155
1–2	2.646	1.527
2–3	4.495	4.641
3–4	2.007	3.159
> 4	0.009	/
Total area	**9.482**	**9.482**

Nevertheless, it is fundamental to mention that the area with *ETa* values in the 0–1 mm range also increased from 0.155 km^2 in 1986 to 0.325 km^2 in 2022. This trend may indicate that there has been an increase in impervious surfaces in the Zlatibor urban expansion area, such as paved roads and buildings, which has reduced the amount of vegetation and soil moisture, resulting in lower rates of evapotranspiration in this range.

To determine the SUHI effect, the region surrounding the Zlatibor main urban area (MUA) is divided into five distinct zones (*Fig. 4* and *Table 4*):

Zone 1, which represents the main urban area of Zlatibor.

Zone 2, which encompasses an area of 100 m around Zone 1.

Zone 3 covers an area from 100 m to 300 m from Zone 1.

Zone 4 includes the area from 300 m to 500 m from Zone 1.

Zone 5 covers the area from 500 m to 1000 m from Zone 1.

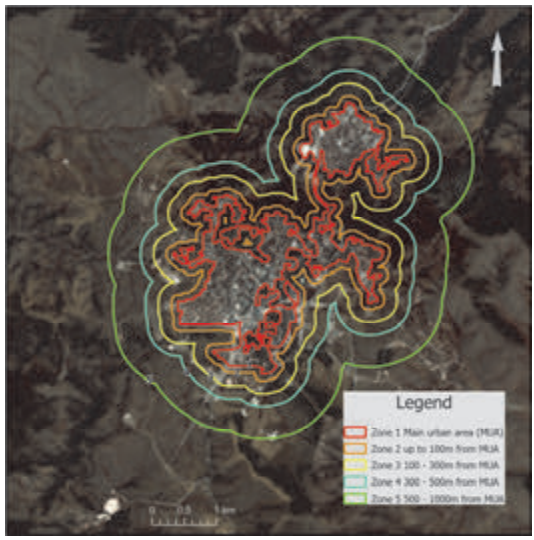

Fig. 4. Zlatibor's main urban area and buffer zones.

Table 4. Comparative analysis of air temperature variations in different zones of Zlatibor MUA from 1986 to 2022

Zone Id (2022)	MIN (2022)	MAX (2022)	RANGE (2022)	MEAN (2022)	STD (2022)	MEDIAN (2022)	Area km^2 (2022)
5	25.43	40.48	15.06	32.65	3.34	33.22	9.00
4	25.47	37.58	12.11	31.53	3.24	32.07	3.68
3	25.36	38.37	13.01	30.78	3.06	30.72	4.29
2	25.46	37.79	12.34	30.29	2.30	29.99	3.35
1	26.39	35.65	9.26	31.05	1.53	31.04	3.97
Zone Id (1986)	**MIN (1986)**	**MAX (1986)**	**RANGE (1986)**	**MEAN (1986)**	**STD (1986)**	**MEDIAN (1986)**	**Area km^2 (1986)**
5	14.25	29.18	14.94	22.35	3.29	22.82	9.00
4	13.78	29.18	15.40	20.81	3.22	21.06	3.68
3	14.25	29.18	14.94	20.07	3.02	20.17	4.29
2	14.25	26.25	12.00	19.76	2.39	19.73	3.35
1	15.18	27.93	12.76	21.13	2.24	21.06	3.97

In 2022, Zone 1, an urbanized area (*Fig. 5*), shows significantly higher *LST* values than the other zones. The mean temperature for Zone 1 is 31.05 °C, which is higher than the mean *LST* values of the other zones. This increase in *LST* is due to the SUHI effect, where urbanized areas tend to be warmer than their rural surroundings due to human activities and the physical characteristics of the built environment.

The minimum and maximum *LST* values for Zone 1 in 2022 are 26.39 °C and 35.65 °C, respectively, with a range of 9.26 °C. This range is the smallest among all zones, indicating a less variable *LST* within the urbanized area. The standard deviation, a measure of temperature variability, is also the lowest in Zone 1, further supporting this observation.

LST increases significantly in all zones, particularly in Zone 1, comparing the 2022 data with the 1986 data. The mean *LST* in Zone 1 increased from 21.13 °C in 1986 to 31.05 °C in 2022, a rise of nearly ten °C. This increase is more significant than those observed in the other zones, suggesting that urbanization has substantially impacted the *LST* rise. It is evident from the data that Zone 1, the most urbanised area, exhibits the highest mean *LST* in 2022 at 31.05 °C. This is a significant increase from the mean temperature of 21.13 °C recorded in 1986, underscoring the impact of urbanization on temperature rise.

Fig. 5. Transformation of main urban area in Zlatibor: a dual temporal perspective of 1986 and 2022, highlighting urbanized and pre-urbanized land.

In contrast, Zones 2 to 5, which are less urbanized, show lower mean *LST* values in 2022. Specifically, Zone 2 has a mean LST of 30.29 °C, Zone 3 has 30.78 °C, Zone 4 has 31.53 °C, and Zone 5 has 32.65 °C. While high, the *LST* values for Zones 2 and 3 are still lower than the temperature in Zone 1, indicating that the level of urbanization directly correlates with the increase in temperature. The urbanization in Zone 1, characterized by increased building density and the transformation of natural landscapes into built environments, has led to a significant rise in the *LST* values. This change is a manifestation of the SUHI effect, where urbanized areas tend to be warmer than their rural surroundings due to human activities and the physical characteristics of the built environment. The built environment in Zone 1, with its concrete and asphalt structures, absorbs and retains heat more effectively than the natural landscape, increasing the ambient *LST*. This contrasts with Zones 2 to 5, where vegetation and rocks that absorb heat contribute to the high *LST* values, but not to the same extent as the urbanization in Zone 1. The data from the different zones in the Zlatibor settlement clearly illustrates the significant impact of urbanization on temperature rise. Despite the natural factors contributing to high LSTs in Zones 2 to 5, the effect of urbanization in Zone 1 is significantly more pronounced, leading to the highest mean *LST* among all zones. This underscores the need for sustainable urban planning strategies to mitigate the SUHI effect and promote thermal comfort in urban areas.

4. Discussion

The analysis of average August air temperatures over 37 years shows a constant increase in temperature from 1986 to the present, with some variability from year to year. The most deviant year is 2012, with the highest deviation from the mean. The data suggests that 2005 is a temperature threshold year, indicating increased urbanization and built-up areas. The area covered by class „developed" has increased dramatically over time, indicating rapid urbanization and development.

The tables also show an increase in temperature coverage in the higher temperature ranges, indicating the urban heat island effect and changes in the distribution of evapotranspiration ranges over time. Evapotranspiration values can provide valuable information about urban areas' water balance and environmental conditions. Urban areas often have a higher surface temperature than surrounding rural areas due to the urban heat island effect. This effect can increase the evapotranspiration rate in urban areas, as the higher temperature can increase the evaporation rate from the ground and plant transpiration. However, urban areas may also have lower vegetation and soil moisture levels than rural areas, which can decrease evapotranspiration rates. Additionally, human activities such as paving and building can alter the hydrological cycle, leading to changes in evapotranspiration rates (*Grimm et al.*, 2008).

One of the essential features of this process is the appearance of elements of the artificial environment in the study area: buildings, irrigation systems, transport, and other technical means of communication, which exert an increasing influence on the natural environment and change it, as it was already indicated earlier (*Vasilescu et al*., 2022). Urbanized regions have a dynamic interaction between the natural and artificial environments (biosphere and human-made structures), forming a distinct anthropogenic state of nature. This state, often referred to as the interface between nature and the built environment, is shaped by human actions and is profoundly influenced by our social nature. Overall, the data suggest a significant impact of human development on the environment in the study area.

The study has provided significant insights into the SUHI effect of the studied region. The results align with the findings of *Polydoros et al*. (2022), who also emphasized the role of landscape metrics in mitigating the SUHI effect. The current study's findings further substantiate this claim by providing empirical evidence from the studied region, thereby contributing to the existing body of knowledge on the subject.

However, the study diverges from the work of *Kiran* (2021), which focused on cool surfaces as a mitigation strategy for the SUHI effect in tropical climates. While Kiran's study provides a valuable perspective, the current research underscores the importance of considering a broader range of factors, including landscape metrics and urban planning strategies, in addressing the SUHI effect. This divergence suggests that mitigation strategies may need to be tailored to specific regional and climatic contexts, underscoring the need for further research in this area.

The study also resonates with *Zhou et al*. (2014), who investigated the SUHI effect in China's major cities and identified spatial patterns and drivers. The current study extends this inquiry by identifying similar patterns and drivers in the studied region and suggesting potential mitigation strategies. This comparative analysis underscores the global nature of the SUHI effect and the need for comprehensive, context-specific solutions.

One of the key strengths of this study is the use of a comparative analysis of *LST* variations across different zones over a significant period from 1986 to 2022. This approach has allowed for a comprehensive understanding of the impact of urbanization on temperature rise, particularly in the context of the SUHI effect. The use of mean *LST* as a critical metric has provided a clear and quantifiable measure of the impact of urbanization on temperature.

However, the study is not without its limitations. While useful, reliance on the LST data alone may not capture the full complexity of the SUHI effect, which can influence a range of factors including building materials, vegetation cover, and human activities. Furthermore, the study focuses solely on the Zlatibor main urban area and five surrounding zones, which may limit the generalizability of the findings to other regions or contexts.

In terms of future work, it would be beneficial to incorporate additional variables into the analysis, such as the specific types of urbanization activities in each zone, the types of building materials used, and the extent of vegetation cover. This could provide a more nuanced understanding of the factors contributing to the SUHI effect. Additionally, conducting similar studies in other regions would enhance the generalizability of the findings and contribute to a broader understanding of the impact of urbanization on temperature.

The implications of this study are significant. The findings underscore the urgent need for sustainable urban planning strategies to mitigate the SUHI effect and promote thermal comfort in urban areas. As urbanization continues to increase globally, understanding its impact on temperature and developing strategies to mitigate this effect will be crucial for ensuring the sustainability and liveability of our urban environments.

5. Conclusions

From an urban heat island (UHI) perspective, it is obvious how urbanization contributes to land use changes and increases building density, leading to higher surface air temperatures in urban areas than the in surrounding rural areas. This phenomenon, referred to as the UHI effect, can lead to eco-environmental problems that become more severe with accelerated urbanization.

To better understand the UHI phenomenon, analysing air temperature at urban and rural weather stations and calculating *LST* and *ETa* data from satellite imagery is essential (*Castaldo et al.,* 2015; *Gedzelman et al.*, 2003; *Jiang et al*.,

2019; *Liu* and *Li*, 2018; *Nouri et al.*, 2018; *Yang et al*., 2018). Remote sensing data and algorithms have been utilized and adapted to examine the UHI scale and effect, and its spatiotemporal evolution features have been analyzed (*Gallo et al.*, 1993; *Gong et al.*, 2008; *Imhoff et al*., 2010; *Weng et al.*, 2004).

Biosphere-to-biotechnosphere transformation is accelerating increasingly and is accompanied by a disturbance of the ecological balance and the biological basis of the biotechnosphere. Nature has the characteristic of evolution and progress. In contrast, urbanized areas are subject to obsolescence and must be constantly rebuilt. For overly urbanized areas to be sustainable, efforts should be made to maintain the environment's complex geochemical and energetic processes (*Grădinaru et al*., 2020). The problem is that urban areas are characterised by low biological activity, and very pronounced, generally increasing energy consumption directed toward the immediate satisfaction of human needs. The degradation of the environment is accompanied by the consumption of resources and the emission of polluting substances and energies that damage other natural ecosystems.

It can be concluded that the degree of anthropogenic pressure on nature, taking urbanized areas as an example, is proportional to the difference between the biological characteristics of the original biogeocoenoses and the urban ones that developed later.

Furthermore, in addition to measuring the temperature of a given area, estimates of evapotranspiration derived through remote sensing and global weather datasets offer good information about the existence of UHI. This information is helpful for various applications, including calculating a basin's water budget, evaluating water consumption and crop yield, and monitoring drought conditions.

Understanding the UHI phenomenon is essential, as it can lead to significant eco-environmental problems in urban areas. It also emphasises the significance of using remote sensing data and GIS algorithms to study UHI effects, especially in regions with insufficient weather stations.

This study underscores the significance of the SUHI effect, particularly in urban environments, where it is a critical factor in urban climate change. The SUHI effect, characterized by higher temperatures in urban areas than in surrounding rural ones, is influenced by numerous factors, including urban morphology, land use, and anthropogenic heat. The research also emphasizes the crucial role of green spaces, such as parks and gardens, in mitigating the SUHI effect due to their cooling impact on urban environments. Therefore, the study highlights the importance of comprehensively understanding the SUHI effect and its determinants in developing effective urban climate change mitigation and adaptation strategies. It further underscores the necessity of incorporating green spaces into urban planning and development strategies. The article provides an effective tool for studying the UHI effect, especially in regions with insufficient weather stations. The results provide valuable information on the distribution of

LST in the Zlatibor urban area, which can help study the UHI phenomenon and identify potential areas for implementing UHI mitigation strategies in the area with a significant human development impact on the environment. Finally, research data provide strong evidence of the SUHI effect in Zone 1, with urbanization leading to higher and less variable temperatures than in the surrounding areas. The comparison between 1986 and 2022 clearly shows the significant impact of urbanization on temperature rise over time.

Acknowledgements: The research reported in this paper is supported by Project 451-03-47/2023-01/200091 (Ministry of Science, Technological Development and Innovation of the Republic of Serbia) and Project 1.23/2023 of the Ministry of Defense and the Serbian Army.

References

Almeida, C.R. de, Furst, L., Gonçalves, A., and Teodoro, A.C., 2022: Remote Sensing Image-Based Analysis of the Urban Heat Island Effect in Bragança, Portugal. *Environments - MDPI*, *9*(8), 98. https://doi.org/10.3390/environments9080098

Avdan, U., and *Jovanovska, G.,* 2016: Algorithm for automated mapping of land surface temperature using LANDSAT 8 satellite data. *J. Sensors 2016*, ID 1480307. https://doi.org/10.1155/2016/1480307

Bande, L., Mohamed, M., Asmelash, Y., and Alnuaimi, A., 2022: Residential neighborhood assessment in the city id Al Ain, United Arab Emirates, and the impact on climate change (heat island eddect amalysis). *WIT Trans. Built Environ. 210*. 127–138. https://doi.org/10.2495/ARC220111

Basarin, B., Lukić, T., Bjelajac, D., Micić, T., Stojićević, G., Stamenković, I., Đorđević, J., Đorđević, T., and Matzarakis, A., 2018: Bioclimatic and climatic tourism conditions at Zlatibor mountain (Western Serbia). *Időjárás*, *122*, 321–343. https://doi.org/10.28974/idojaras.2018.3.6

Cao, C., Lee, X., Liu, S., Schultz, N., Xiao, W., Zhang, M., and *Zhao, L.,* 2016: Urban heat islands in China enhanced by haze pollution. *Nat. Commun. 7*. 12509. https://doi.org/10.1038/ncomms12509

Castaldo, V. L., Coccia, V., Cotana, F., Pignatta, G., Pisello, A. L., and *Rossi, F.*, 2015: Thermal-energy analysis of natural "cool" stone aggregates as passive cooling and global warming mitigation technique. *Urban Climate*, *14,* 301–314. https://doi.org/10.1016/j.uclim.2015.05.006

Chen, G., Zhao, L., and *Mochida, A*., 2016: Urban Heat Island simulations in Guangzhou, China, using the coupled WRF/UCM model with a land use map extracted from remote sensing data. *Sustainability 8*(7) 628. https://doi.org/10.3390/su8070628

Cook, M. J. (2014: Atmospheric compensation for a Landsat Land Surface Temperature Product. In RIT Scholar Works. https://doi.org/10.1117/12.2015320

Dimitrijević, M., 1996: Zlatibor, Its Geological Framework . In (Ed. *M.D. Dimitrijević*), Geology of Zlatibor (Special Pu, Vol. 18). Geoinstitute.

Engebretson, C., 2020a: Landsat 8-9 Operational Land Imager (OLI) - Thermal Infrared Sensor (TIRS) Collection 2 Level 2 (L2) Data Format Control Book (DFCB) (Vol. 2, Issue September). Department of the Interior U.S. Geological Survey. Retrieved from https://d9-wret.s3.us-west-2.amazonaws.com/assets/palladium/production/s3fs-public/atoms/files/LSDS-1328_Landsat8-9-OLI-TIRS-C2-L2-DFCB-v6.pdf

Engebretson, C., 2020b: *Landsat Thematic Mapper (TM) Collection 2 (C2) Level 2 (L2) Data Format Control Book (DFCB) Version 4.0*. Department of the Interior U.S. Geological Survey. Retrieved from https://d9-wret.s3.us-west-2.amazonaws.com/assets/palladium/production/s3fs-public/atoms/files/LSDS-1336_Landsat4-5-TM-C2-L2-DFCB-v4.pdf

Esri Inc., 2023: ArcGIS Pro (Version 3.0.3). In *Esri Inc.*

Fardani, I., and *Yosliansyah, M.R*., 2022: Kajian penentuan prioritas ruang terbuka hijau berdasarkan fenomena urban heat island di kota cirebon.. *Jurnal Sains Informasi Geografi*, *5*(2). https://doi.org/10.31314/jsig.v5i2.1708

Gallo, K.P., McNab, A.L., Karl, T.R., Brown, J.F., Hood, J.J., and *Tarpley, J.D*., 1993: The use of NOAA AVHRR data for assessment of the urban heat island effect. *J. Appl. Meteorol. 32*, 899–908. https://doi.org/10.1175/1520-0450(1993)032<0899:TUONAD>2.0.CO;2

Gedzelman, S. D., Austin, S., Cermak, R., Stefano, N., Partridge, S., Quesenberry, S., and *Robinson, D.A*., 2003: Mesoscale aspects of the Urban Heat Island around New York City. *Theor. Appl. Climatol. 75*(1–2), 29–42. https://doi.org/10.1007/s00704-002-0724-2

Gong, A. Du, Xu, J., Zhao, J., and *Li, J.*, 2008: A survey of study method for urban heat island. *J. Nat.Disasters17*(6).

Grădinaru, S.R., Iojă, C. I., Vânău, G.O., and O*nose, D.A.,* 2020: Multi-dimensionality of land transformations: From definition to perspectives on land abandonment. *Carpathian J. Earth Environ. Sci. 15*(1), 161–177. https://doi.org/10.26471/cjees/2020/015/119

Grimm, N.B., Faeth, S.H., Golubiewski, N.E., Redman, C.L., Wu, J., Bai, X., and *Briggs, J.M*., 2008: Global change and the ecology of cities. *Science 319*, 5864. https://doi.org/10.1126/science.1150195

Howard, L., 1833: The Climate of London: Deduced from Meteorological Observations, Made at Different Places in the Neighbourhood of the Metropolis,Vol.1. In IAUC edition.

Imhoff, M.L., Zhang, P., Wolfe, R.E., and *Bounoua, L*., 2010: Remote sensing of the urban heat island effect across biomes in the continental USA. *Remote Sens. Environ. 114*, 504–513. https://doi.org/10.1016/j.rse.2009.10.008

Jiang, P., Liu, X., Zhu, H., and *Li, Y.,* 2019: Features of urban heat Island in mountainous chongqing from a dense surface monitoring network. *Atmosphere*, *10,* 67. https://doi.org/10.3390/atmos10020067

Kiran, K., 2021: Cool surface as urban heat island effect mitigation strategy for tropical climate. Nanyang Technological University. https://doi.org/10.32657/10356/153374

Liu, C., and *Li, Y*., 2018: Spatio-temporal features of urban heat island and its relationship with land use/cover in mountainous city: A case study in Chongqing. *Sustainability 10*(6), 1943. https://doi.org/10.3390/su10061943

Liu, K., Su, H., Zhang, L., Yang, H., Zhang, R., and *Li, X.*, 2015: Analysis of the urban heat Island effect in shijiazhuang, China using satellite and airborne data. *Remote Sensing 7,* 4804–4833. https://doi.org/10.3390/rs70404804

Lješević, M. and *Mihajlović, L.,* 2020: Geomorphological diversity influence on population settlement. *EGU General Assembly 2020*, EGU2020-20838. https://doi.org/10.5194/egusphere-egu2020-20838

Mohajerani, A., Bakaric, J., and J*effrey-Bailey, T.,* 2017: The urban heat island effect, its causes, and mitigation, with reference to the thermal properties of asphalt concrete. *J. Environ. Manage. 197*, 522–538. https://doi.org/10.1016/j.jenvman.2017.03.095

Nouri, A.S., Costa, J.P., Santamouris, M., and *Matzarakis, A*., 2018: Approaches to outdoor thermal comfort thresholds through public space design: A review. *Atmosphere 9*(3), 108. https://doi.org/10.3390/atmos9030108

Novković, I., 2008: Geoheritage of Zlatibor District. *J. Inst.r Nature Conservation of Serbia "Protection of Nature," 58*(1–2), 37–52. https://www.zzps.rs/wp/casopisi_pdf/010/casopis.pdf?script=lat

Pecelj, M., Dordević, A., Pecelj, M.R., Pecelj-Purković, J., Filipović, D., and *Šećerov, V.,* 2017: Biothermal conditions on Mt. Zlatibor based on thermophysiological indices. *Arch. Biol. Sci. 69,* 455–461. https://doi.org/10.2298/ABS151223120P

Pecelj, M., Matzarakis, A., Vujadinović, M., Radovanović, M., Vagić, N., Đurić, D., and *Cvetkovic, M.* (2021: Temporal analysis of urban-suburban pet, mpet and utci indices in belgrade (Serbia). *Atmosphere*, *12*(7), 916. https://doi.org/10.3390/atmos12070916

Pecelj, M., Pecelj, M., Mandic, D., Pecelj, J., Vujadinovic, S., Šecerov, V., Dejan, Š., Gajic, M., and *Milincic, M.,* 2010: Bioclimatic assessment of weather condition for recreation in health resorts. 6th WSEAS Int. Conf. on Cellular and Molecular Biology, Biophys. and Bioeng., BIO'10, 8th WSEAS Int. Conf. on Environ., Ecosystems and Dev., EED'10, Int. Conf. on Biosci. and Bioinformatics, ICBB'10.

Polydoros, A., Cartalis, C., Santamouris, M., and *Kolokotsa, D.,* 2022: Use of landscape metrics for the mitigation of the surface urban heat island effect in Mediterranean cities. *Glob. Urban Heat Island Mitig.* 2022, 95–108. https://doi.org/10.1016/B978-0-323-85539-6.00015-9

Priyadarsini, R., Hien, W.N., and *Wai David, C.K*., 2008: Microclimatic modeling of the urban thermal environment of Singapore to mitigate urban heat island. *Solar Energy 82*, 727–745. https://doi.org/10.1016/j.solener.2008.02.008

Prostak, C., 2023: Newspaper Map. In *ESRI basemap*. ESRI. Retrieved from https://www.arcgis.com/home/item.html?id=75a3ce8990674a5ebd5b9ab66bdab893

Rao, P., 1972: Remote sensing of urban "heat islands" from an environmental satellite. *Bull. Amer. Meteorol. Soc.*, 647–648.

Republički zavod za statistiku Srbije., 2023: Popisni podaci - eksel tabele. Retrieved from https://www.stat.gov.rs/sr-Latn/oblasti/popis/popis-2011/popisni-podaci-eksel-tabele

RHSS., 1987–2022: Meteorological Yearbook 1. – Climatological Data for [respective year]. Republic Hydrometeorological Service of Serbia. Retrieved from https://www.hidmet.gov.rs/data/meteo_godisnjaci/

Sayler, K. and *Glynn, T.,* 2022: Landsat 4-9 Collection 2 Level-3 Provisional Actual Evapotranspiration Product Guide Version 1.0. Department of the Interior U.S. Geological Survey.

Sayler, K. and *Zanter, K.*, 2021: Landsat 4-7 Collection 2 (C2) Level 2 Science Product (L2SP) Guide Version 4.0 (Vol. 4). Department of the Interior U.S. Geological Survey. Retrieved from https://d9-wret.s3.us-west-2.amazonaws.com/assets/palladium/production/s3fs-public/media/files/LSDS-1618_Landsat-4-7_C2-L2-ScienceProductGuide-v4.pdf

Sayler, K., Zanter, K., and *Glynn, T.,* 2022: Landsat 8-9 Collection 2 (C2) Level 2 Science Product (L2SP) Guide Version 4.0 (Vol. 4, Issue May). Department of the Interior U.S. Geological Survey. Retrieved from https://d9-wret.s3.us-west-2.amazonaws.com/assets/palladium/production/s3fs-public/media/files/LSDS-1619_Landsat-8-9-C2-L2-ScienceProductGuide-v4.pdf

Senay, G.B., 2018: Sattelite Psychrometric Formulation of the Operational Simplified Surface Energy Balance (Ssebop) Model for Quantifying and Mapping Evapotranspiration. *Applied Engineering in Agriculture*, *34*(3) 555–566. https://doi.org/10.13031/aea.12614

Senay, G.B., Bohms, S., Singh, R.K., Gowda, P.H., Velpuri, N.M., Alemu, H., and *Verdin, J.P*., 2013: Operational Evapotranspiration Mapping Using Remote Sensing and Weather Datasets: A New Parameterization for the SSEB Approach. *J. Amer. Water Res. Assoc. 49*(3). https://doi.org/10.1111/jawr.12057

Senay, G. B., Friedrichs, M., Morton, C., Parrish, G. E. L., Schauer, M., Khand, K., Kagone, S., Boiko, O., and *Huntington, J.,* 2022: Mapping actual evapotranspiration using Landsat for the conterminous United States: Google Earth Engine implementation and assessment of the SSEBop model. *Remote Sens. Environ 275*, 113011. https://doi.org/10.1016/j.rse.2022.113011

Senay, G. B., Parrish, G. E. L., Schauer, M., Friedrichs, M., Khand, K., Boiko, O., Kagone, S., Dittmeier, R., Arab, S., and *Ji, L.*, 2023: Improving the Operational Simplified Surface Energy Balance Evapotranspiration Model Using the Forcing and Normalizing Operation. *Remote Sensing 15,* 260. https://doi.org/10.3390/rs15010260

Stathopoulou, M. and *Cartalis, C*., 2007: Daytime urban heat islands from Landsat ETM+ and Corine land cover data: An application to major cities in Greece. *Solar Energy*, *81,* 358–368. https://doi.org/10.1016/j.solener.2006.06.014

Stojsavljević, R., Božić, S., Kovačević, M., Živković, M.B., and *Miljković, Đ*., 2016: Influence of selected climate parameters on tourist traffic of Kopaonik and Zlatibor mountains (Republic of Serbia). *Geographica Pannonica*, *20*(4), 208–219. https://doi.org/10.5937/GeoPan1604208S

Streutker, D.R., 2003: Satellite-measured growth of the urban heat island of Houston, Texas. *Remote Sens. Environ. 85*(3), 282–289. https://doi.org/10.1016/S0034-4257(03)00007-5

Sugiarto, A., Setiawan, B.I., Arif, C., and *Saptomo, S.K*., 2021: Estimasi Dampak Urban Heat Island terhadap Laju Evapotranspirasi: Studi Kasus di Kota Palembang. *Jurnal Teknik Sipil Dan Lingkungan*, *6*(1). https://doi.org/10.29244/jsil.6.1.23-34

Tan, J., Zheng, Y., Tang, X., Guo, C., Li, L., Song, G., Zhen, X., Yuan, D., Kalkstein, A. J., Li, F., and *Chen, H.* ,2010: The urban heat island and its impact on heat waves and human health in Shanghai. *Int. J. Biometeorol. 54*(1). https://doi.org/10.1007/s00484-009-0256-x

Tang, J., Lan, X., Lian, Y., Zhao, F., and Li, T. (2022: Estimation of Urbanandndash;Rural Land Surface Temperature Difference at Different Elevations in the Qinlingandndash;Daba Mountains Using MODIS and the Random Forest Model. *Int. J. Environ.Res. Publ. Health 19,* 11442. https://doi.org/10.3390/ijerph191811442

Tosic, D. and *Obradovic, D*., 2003: Modern tendencies in developing net of settlements of municipality Smederevo. *Glasnik Srpskog Geografskog Drustva*, *83*(2), 31–44. https://doi.org/10.2298/GSGD0302031T

U.S.G.S. (2015: USGS EarthExplorer. USGS Science for a changing world.

Vakanjac, V.R., Stevanović, Z., Stevanović, A.M., Vakanjac, B., and *Ilić, M.Č.,* 2015: An example of karst catchment delineation for prioritising the protection of an intact natural area. *Environ. Earth Sci. 74,* 7643–7653. https://doi.org/10.1007/s12665-015-4390-y

Vasilescu, A.G., Niță, M.R., and *Pătru-Stupariu, I*., 2022: Methods for identifying the benefits associated with urban green infrastructure at different urban scales. *Carpathian J. Earth Environ. Sci. 17*, 69-80. https://doi.org/10.26471/cjees/2022/017/201

Voogt, J.A. and *Oke, T.R.*, 2003: Thermal remote sensing of urban climates. *Remote Sens. Environ. 86*, 370–384. https://doi.org/10.1016/S0034-4257(03)00079-8

Vukoičić, D., Ristić, D., Milinčić, U., Petrović, D., Mihajlović, L., Božović, S., and *Protić, B.,* 2023: Assessment of the Attractiveness of Natural Resources and Landscapes of the Kopaonik National Park (Serbia): Framework and Importance for Tourism Development. *Polish J. Environ. Studies*, *32*, 281–295. https://doi.org/10.15244/pjoes/152378

Weng, Q., Lu, D., and *Schubring, J.,* 2004: Estimation of land surface temperature-vegetation abundance relationship for urban heat island studies. *Remote Sens. Environ. 89*(4), 467–483. https://doi.org/10.1016/j.rse.2003.11.005

Yang, J., Mohan Kumar, D. llamathy, Pyrgou, A., Chong, A., Santamouris, M., Kolokotsa, D., and *Lee, S.E.,* 2018: Green and cool roofs' urban heat island mitigation potential in tropical climate. *Solar Energy 173,* 597–609. https://doi.org/10.1016/j.solener.2018.08.006

Zhou, D., Zhang, L., Hao, L., Sun, G., Liu, Y., and *Zhu, C.*, 2016: Spatiotemporal trends of urban heat island effect along the urban development intensity gradient in China. *Sci. Total Environ. 544*, 617–626. https://doi.org/10.1016/j.scitotenv.2015.11.168

Zhou, D., Zhao, S., Liu, S., Zhang, L., and *Zhu, C.,* 2014: Surface urban heat island in China's 32 major cities: Spatial patterns and drivers. *Remote Sens. Environ. 152*. 51–61. https://doi.org/10.1016/j.rse.2014.05.017

Zhou, D., Zhao, S., Zhang, L., Sun, G., and *Liu, Y.,* 2015: The footprint of urban heat island effect in China. *Scientific Reports 5*. https://doi.org/10.1038/srep11160

Živanović, V., Pavlović, M., Kovjanić, A., Tošić, D., and Krstić, F. (2021: Concept of polycentricity—the differences between development policies and spatial reality. *J. Geograph. Inst. Jovan Cvijic SASA*, *71*(1), 75–90. https://doi.org/10.2298/IJGI2101075Z

DOI:10.28974/idojaras.2024.3.5

IDŐJÁRÁS

Quarterly Journal of the HungaroMet Hungarian Meteorological Service
Vol. 128, No. 3, July – September, 2024, pp. 367–377

Observed changes in the contribution of extreme precipitation over the Zagros Mountains, Iran

Hamid Nazaripour[1,*], **Mehdi Sedaghat**[2], and **Alireza Sadeghinia**[3]

[1]*Department of Physical Geography*
University of Sistan and Baluchestan
Zahedan, Iran

[2]*Department of Geography*
Payam-e Noor University (PNU)
Tehran, Iran

[3]*Department of Geography Education*
Farhangian University
Tehran, Iran

**Corresponding Author Email: h.nazaripour@gep.usb.ac.ir*

(Manuscript received in final form July 10, 2023)

Abstract— Due to global warming, precipitation regimes are expected to change, and heavy events are expected to occur more frequently. This study investigates the relative share of heavy daily precipitation events to total precipitation for past and current climates. In this regard, daily precipitation data with a spatial resolution of 0.25° × 0.25° from the APHRODITE and CHIRPS databases are used. We used two nonparametric tests, the Mann–Kendall test and Sen's slope estimator, to identify the trend. The results showed that the frequency of daily heavy precipitation has been increasing in most regions of Iran. The relative share of heavy daily precipitation events to total precipitation has increased over the southwest and central areas of Iran from a case of the past to the current climate. The rise in the share of heavy precipitation of the total precipitation has led to a decrease in the frequency of rainy days (wet days) and an increase in the intensity and concentration of precipitation in Iran. The amount of increase in the share of heavy rainfall to the total precipitation is more prominent in the middle parts of the Zagros Mountains. These conditions lead to heavy floods in the southwestern plains of Iran.

Key-words: extreme daily precipitation, Mann-Kendall test, trend analysis, Iran

1. Introduction

In general, a climate extreme event is defined as the occurrence of a weather or climate event above (or below) a certain threshold value near the upper (or lower) ends of the range of observed values of the variable. Extreme weather events (droughts, heavy rainfall, floods, and heatwaves) are a matter of great topical importance and interest in a variety of environmental and social situations (*Karimi et al*., 2021). Compared to the average climate, extreme events have a much greater impact on human activity and natural environments (*Kunkel et al*., 1999; *Easterling et al*., 2000). The possible increase of extreme weather events both in frequency and intensity is among the predicted effects of climate change. Observational analysis has indicated that extreme climate events have exhibited an increasing trend in most areas of the earth in the past half century, including arid areas, such as Iran (*Zarrin* and *Dadashi-Roudbari*, 2022; *Darand* and *Pazhoh*, 2022; *Nazaripour* and *Mansouri Daneshvar*, 2014; *Jian-Qi*, 2012). Rainfall extremes are likely to have profound impacts on human societies (e.g., *Miri et al*., 2023) and can lead to the loss of lives and property (*Sharifi* and *Bokaie,* 2019). In addition, simulation studies have predicted the occurrence of more extreme rainfall events due to the cumulative effects of greenhouse gases (*Zarrin et al*., 2022; *Ayugi et al*., 2021; *Chen et al*., 2020; *Darand*, 2020; *Almazroui* and *Saeed*, 2020). Thus, in the past decades, there has been increased research focusing on extreme climate events to more deeply and comprehensively understand their variability (*Nourani* and *Najafi*, 2022; *Rousta et al*., 2016). However, the studies of heavy precipitation in Iran it has not yet been perfected.

The mean annual precipitation of Iran in more than half of the surface area (60%) is less than 200 mm, and some parts (30%) get less than 50 mm annually. On this basis, Iran is located in a dry climatic zone with a mean rainfall of approximately 250 mm/year. The northern slopes of the Alborz Mountain range in the north, Zagros highlands, and northwestern Iran receive more rainfall; while the interior parts of the country receive much less precipitation (*Fig. 1*). During the last decades, some aspects of precipitation in Iran have undergone several changes, and about half of the country's surface area has been subject to them. Studies have shown that precipitation amounts during wet days as well as a number of heavy and very heavy precipitation days tend to decrease across the study area (*Alavinia* and *Zarei*, 2021). In addition, a general downward trend in annual precipitation can be observed, particularly in areas of northern, western, and northwestern Iran (*Najafi* and *Moazami*, 2016). The frequency of heavy precipitation has declined in the northwest, western and northeastern parts of Iran (*Mahbod* and *Rafiee*, 2021). While the trend of the most extreme precipitation indicators in Iran is increasing (*Balling et al*., 2016), the relative occurrence of one-day precipitations in creating total rainfall and the frequency of rainy days on an annual scale has decreased by about 20% over the area of Iran (*Nazaripour* and *Mansouri Daneshvar*, 2014). Studies have shown an upward trend in both

intensity and number of extremes, e.g., maximum daily precipitation and number of days with precipitation above the 90th percentile, across Iran (*Fathian et al*., 2020). In general, winter (between December and March) represents the main rainy season in Iran. Most parts receive more than half of the annual precipitation totals during winter (*Domroes et al*., 1998). Today, the research results show a change in the precipitation regime, a decrease in rainy days and total precipitation, and an increase in the concentration of precipitation in Iran (*Darand* and *Pazhoh*, 2022).

Heavy rainfall is one of the most important types of extreme weather events. Each year, Iran experiences massive heavy rainfall events, for example, the unprecedented heavy precipitation events in the western district of Iran between March 20 and April 21 in 2019 (*Fazel-Rastgar*, 2020; *Alborzi et al*., 2022), and in the western and southwestern part of Iran in April 2016 (*Dizaji et al*., 2019). These extreme events resulted in a great damage of life and property throughout a great number of regions. In each part of Iran, the extreme rainfalls share a portion of total rainfall amounts. The mentioned variability can be considered as climate change signals in respect of heavy rainfall events. The results of previous studies have shown variations in two important aspects of heavy rainfall events (frequency and intensity) in Iran. But in reality, the variation in frequency or intensity does not determine the share of heavy precipitation in total precipitation. The spatial distribution of the share of heavy precipitation of the total rainfall in Iran is still not clear, although a number of studies have investigated the variation of its frequency and intensity. Thus, in this study, we attempt to investigate the variation of the contribution of extreme rainfall to the total rainfall.

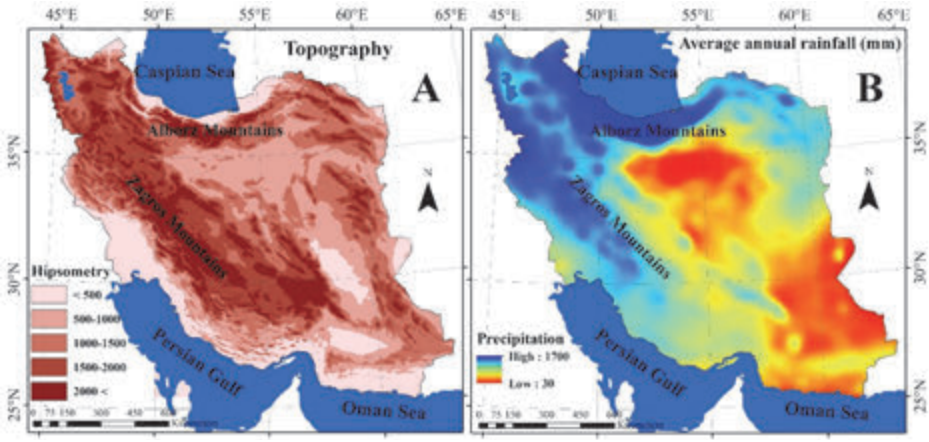

Fig. 1. Geographical distribution of topography (A) and annual long-term mean precipitation (1961–2010) (B) over Iran.

2. Data and methodology

The global estimated daily rainfall data were extracted from two high-resolution (0.25°×0.25°) databases (CHIRPS and APHRODITE) for a similar domain 43.125° to 64.125° E and 24.125° to 40.125° N. Precipitation data of the APHRODITE and CHIRPS datasets are accessible for everyone in the links https://data.chc.ucsb.edu/products/CHIRPS-2.0/global_daily and http://aphrodite.st.hirosaki-u.ac.jp/product/APHRO_V1101/APHRO_ME/025deg_nc. Then, the two databases are merged to obtain a long-term time period. Daily rainfall data is accessible for the period 1951–2007 and 1981–2022 in APHRODITE and CHIRPS, respectively. Thus, in this study, the period of 1961–2010 is considered. Consequently, the rainfall data from 4893 points were used in this study. The threshold of heavy precipitation is estimated according to the percentile. First, we set the convention criterion ($R \geq 1$mm) for the wet day, where R is the daily precipitation amount, and then, we modified the combined precipitation database accordingly. Subsequently, we calculated the 95th and 90th percentiles of daily rainfall for the wet days of each year from 1961–2010. Then, the 30-year mean of the 95th and 90th percentile values are regarded as the heavy precipitation threshold. Here, a heavy precipitation day is considered a day with rain more than the extreme precipitation threshold. The heavy precipitation for one year is considered the sum of precipitation for the heavy precipitation days of the year, and the total precipitation is considered the sum of precipitation for all rainy days of the year. The share of heavy precipitation to the total rainfall is calculated as

$$CRNN_j = \frac{\sum_{w=1}^{w} R_{wj} \quad whrer\, R_{wj} > R_{wj}NN}{R_j} \ , \tag{1}$$

where $CRNN_j$ is the percentage of total rainfall contributed by heavy rainfall in any year, R_j is the total amount of daily rainfall on wet days ($R \geq 1$mm) in period j, R_{wj} is the sum of daily precipitation on heavy precipitation days ($R >$ 90th and 95th percentile) and represents the count of wet days in the period j. The output of applying this equation to the merged database creates two new databases of the share of heavy precipitations to total rainfall, which are named CR^{90} and CR^{95}, respectively. In this database, the share of heavy precipitation to total rainfall in every year (up to 50 years) is available at every point (up to 4893 points).

Trend analysis can be performed by parametric and nonparametric tests. Nonparametric techniques are more suitable for time series when statistical distributions are not fit for them. The negligible influence of this method on extreme values is one of the benefits of this method (*Alavinia* and *Zarei*, 2021). Considering these advantages, this research used the Mann-Kendall test to

determine the trend in the share of heavy precipitation to total rainfall. The null (H_0) and alternative (H_a) hypotheses of the MK nonparametric test are defined as the non-existence and existence of a trend in time series (*Shadmani et al*., 2012). Negative and positive MK values indicate a decreasing or increasing trend, respectively (*Nazaripour* and *Mansouri Daneshvar*, 2014). The Mann-Kendall statistic S is given as

$$S = \sum_{i=1}^{n-1} \sum_{j=i+1}^{n} sgn(x_j - x_i) \,. \tag{2}$$

The application of the trend test is done to the time series x_i (i=1, 2, …, n-1) and x_j (j=i+1, 2, …., n). each of the data point x_i is taken as a reference point which is evaluated with the other of the data points x_j, and the value $sgn(x_j - x_i)$ is computed as

$$sgn(x_j - x_i) = \begin{cases} +1 & if \ (X_j - X_i) > 0 \\ 0 & if \ (X_j - X_i) = 0 \\ -1 & if \ (X_j - X_i) < 0 \end{cases} \,. \tag{3}$$

This statistic represents the number of positive differences minus the number of negative differences for all the differences considered. Where n is the number of observed series, X_j and X_i are data values at time j and i, respectively. The Mann-Kendall statistic S is standardized as follows

$$Z_{MK} = \begin{cases} \frac{S-1}{\sqrt{Var(S)}} & if \quad S > 0, \\ 0 & if \quad S = 0, \\ \frac{S+1}{\sqrt{Var(S)}} & if \quad S < 0. \end{cases} \tag{4}$$

The variance statistic is given as

$$\text{Var}\,(S) = \frac{1}{18}[n(n-1)(2n+5) - \sum_{i=1}^{m} t_i(t_i-1)(2t_i+5)] \,, \tag{5}$$

where t_i is considered as the number of ties up to sample i, m represents the number of series in which at least one duplicate data exists. A positive (negative) value of Z_{MK} signifies an increasing (decreasing) trend of the time series. A significance level α is also utilized for testing either an increasing or a decreasing

trend (two-tailed test). If Z_{MK} is greater than $Z_{\alpha/2}$, where α depicts the significance level, then it is recognized that the trend is significant. The magnitude of the trend was predicted by the Sen's estimator (*Sen*, 1968). Here, the slope (T_i) of all data paired is computed as

$$T_i = \frac{(x_j - x_k)}{(j-k)} \quad for\ i = 1, 2, \dots, N\ , \tag{6}$$

where x_j and x_k are considered as data values at time j and $k(j > k)$ correspondingly. The median of these N values of T_i is represented by Sen's estimator of the slope, which is given as

$$Q_i = \begin{cases} T_{\frac{N+1}{2}} & N\ is\ odd, \\ \frac{1}{2}\left\{T_{\frac{N}{2}} + T_{\frac{N+2}{2}}\right\} & N\ is\ even\ . \end{cases} \tag{7}$$

The Sen's estimator is computed as $Q_{med} = T(N+1)/2$ if N is odd, and it is considered as $Q_{med} = [T(N/2) + T_{(N+2)/2}]$ if N is even. In the end, Q_{med} is computed by a two-sided test at the $100(1-\alpha)\%$ confidence level. The positive (negative) value of Q_i indicates an increasing (decreasing) trend in the time series.

3. Results and discussion

The mean annual precipitation of Iran in more than 70% of area is below 250 mm, some parts get less than 50 mm, and only less than 5% of the surface area of Iran receives above 500 mm annually. The annual mean rainfall ranges from smaller than 50 mm up to beyond 1500 mm (*Fig. 1*). On this basis, Iran is located in an arid and semiarid zone. The topography is also associated with much of the spatial variation of annual precipitation. The precipitation pattern in Iran is heavily affected by the Alborz and Zagros mountain ranges. The wettest areas are located in northern Iran, on the southwestern coast of the Caspian Sea, and on the western and southern slopes of the Zagros Mountains. The interior areas receive much less precipitation .These regions (i.e., the Lut and Kavir deserts) are referred to as arid areas (*Alijani et al*., 2008).

Fig. 2 shows the percentage ratio of rainfall caused by extreme daily rainfall events (R > 95th percentile) to the total rainfall over Iran. To better understand the changes, the share of heavy rainfalls in two different 30-year periods (1961–1990 and 1991–2020) have been investigated. Heavy daily rainfall events contributed a large proportion (almost 50%) of the total precipitation over Iran during the periods examined (*Fig. 2*). The results in the first period (1961–1990) imply that heavy daily rainfall events contributed 20% of the total annual precipitation in the

wettest zones. In the second period (1991–2020), this contribution has increased by about 5%. By evaluation, the share of heavy rainfall events to the total rainfall in arid areas is more than twice that of wet areas.

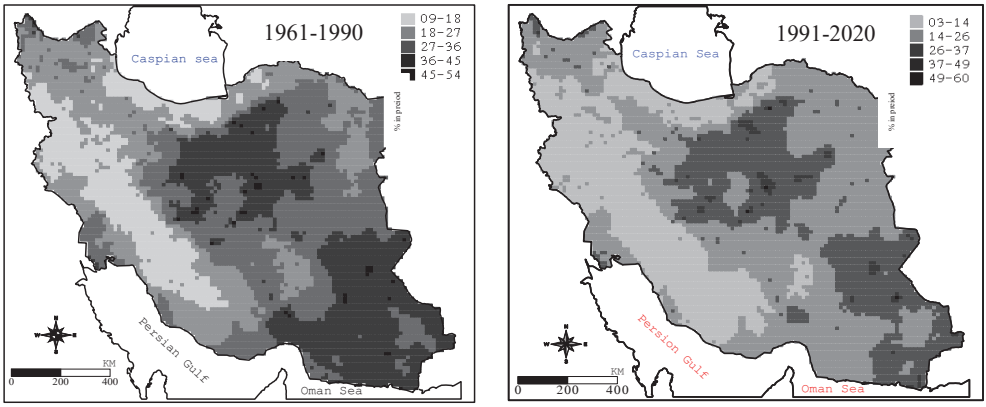

Fig. 2. Relative share of heavy daily rainfall events (R > 95th percentile) to the total rainfall over Iran during the periods 1961–1990 (left) and 1991–2020 (right).

Trend analysis of the share of heavy daily rainfall events to total precipitation has been done in the present research for 50 years (1961–2010). Mann-Kendall test and Sen's slope estimator have been used for the recognition of the trend. The spatial distribution of significant trends (at the 5% confidence level) and also the magnitude of the decadal trend for the share of extreme rainfall to total rainfall in Iran are shown in *Figs. 3* and *4*. The results of the trend analysis using the Mann-Kendall test indicate the existence of a significant upward trend in the share of heavy rainfall to total precipitation in the long period of 1961–2010 in the entire area of Iran. These results are in line with earlier studies (such as *Zarin* and *Dadashi-Roudbari*, 2022; *Almazroui* and *Saeed*, 2020). The integrity of the upward trend is stretched in a wide strip from the southwest to the northeast of Iran. These areas correspond to the Zagros mountain range, especially its wide parts on the shores of the Persian Gulf, and also to the central deserts. This increasing trend is evident in the country of Iraq and can be extended to the Arabian Peninsula as well (*Almazroui* and *Saeed,* 2020). These results seem reasonable because, on the one hand, due to global

warming, the moisture content of the atmosphere (water vapor) in the surrounding areas of water beds has increased, leading to heavy rains. On the other hand, wet days are decreasing in desert areas and far from moisture sources, and it leads to intensifying the concentration of precipitation and increasing its intensity. The magnitude of the decadal trends of the contribution of heavy precipitation to total rainfall in southwestern Iran is higher than in the central deserts. In the southwestern regions, the share of heavy rain is increasing up to 5%, while in the central deserts, it is up to 1%.

The southwestern regions of Iran is the the drainage basin of the major and permanent rivers (e.g., Karun, Karkheh, Jarahi, etc.) that originate from the heights of Zagros and lead to the Persian Gulf. Floods as natural hazard have always threatened the human and natural environments of these regions. In recent decades, the natural environment of these areas has become extremely vulnerable as a result of natural climate change (drought) and anthropogenic activities (dam construction, forest destruction, agriculture, etc.). As a result of these conditions, flooding is expected to occur more frequently and more severely in these areas in the future.

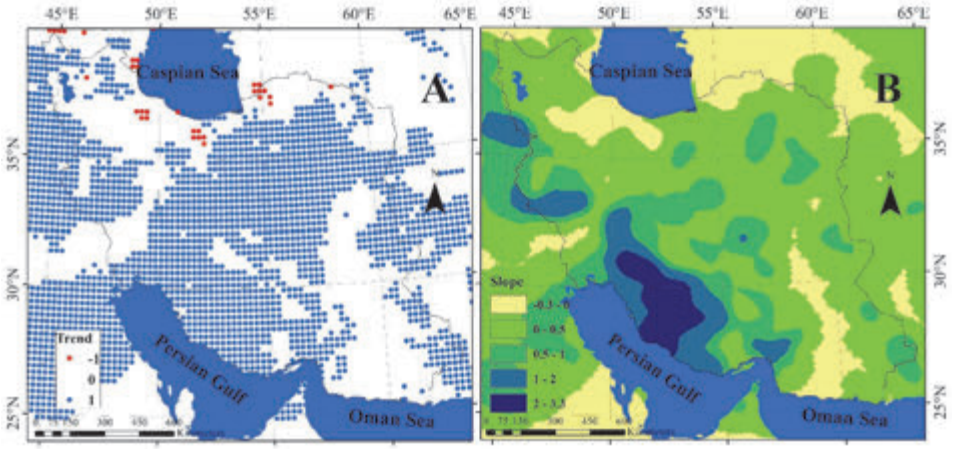

Fig. 3. Spatial distribution of significant trends (left) and magnitude of trends (right) in CR95 based on Mann-Kendall and Sen's estimator tests in the 1961–2010 period, respectively. Filled blue(red) circles indicate positive (negative) trends at the 5% significance level.

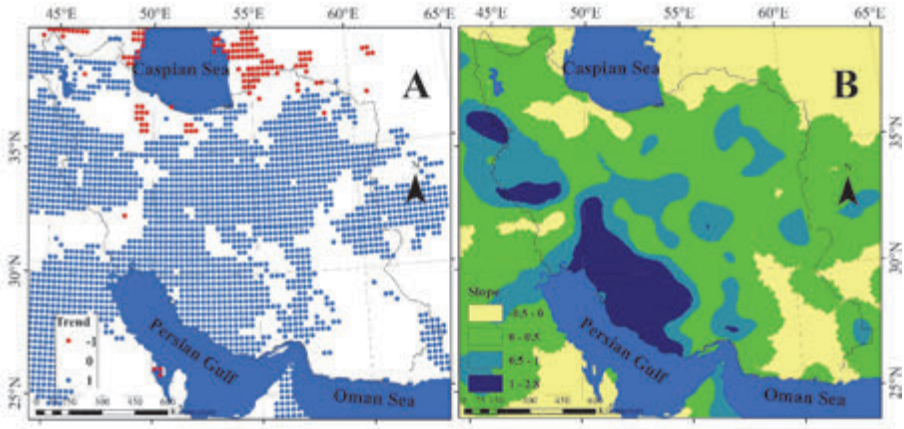

Fig. 4. Spatial distribution of significant trends (left) and (right) in CR90 based on Mann-Kendall and Sen's estimator tests in the 1961–2010 period, respectively. Filled blue(red) circles indicate positive (negative) trends at the 5% significance level.

4. Conclusion

As a general result, the change in the relative share of heavy rainfall to the total precipitation in Iran is statistical evidence of the change in Iran's rainfall regime. This means that the precipitation regime will become more concentrated and intense. The analysis of the contribution of heavy rainfall to total precipitation in the territory of Iran based on the data of APHRODITE and CHIRPS databases in the last half century (1961–2010) indicates the existence of a strong positive (upward) and reliable trend. The spatial distribution of increasing trends in a wide strip has a southwest-northeast arrangement. The relative share of heavy daily rainfall events to total precipitation has increased over the southwestern and central parts of Iran from the past to the current climate. The amount of increase in the share of heavy rainfall to the total precipitation is more prominent in the middle parts of the Zagros Mountains. The amount of decennial increase in the share of extreme rainfall to total precipitation also decreases from southwest to northeast. The increasing trend of this indicator in the territory of Iran is an evidence of the change in Iran's rainfall regime. This means that the increase in the share of heavy rainfall to the total rainfall has led to a decrease in the frequency of rainy days (wet days) and to an intensification in the intensity and concentration of precipitation in Iran.

Acknowledgments: We are very grateful to *Dr. Mahmood Khosravi* from the Department of Geography at the University of Sistan and Baluchestan in Iran for his superior advice. Thanks also to one of the anonymous reviewers for suggestions on data interpretations.

References

Alavinia, S. H., and *Zarei, M. 2021*. Analysis of spatial changes of extreme precipitation and temperature in Iran over a 50-year period. *Int. J. Climatol. 41*, E2269-E2289. https://doi.org/10.1002/joc.6845

Alborzi, A., Zhao, Y., Nazemi, A., Mirchi, A., Mallakpour, I., Moftakhari, H., ... and *AghaKouchak, A*. 2022. The tale of three floods: From extreme events and cascades of highs to anthropogenic floods. *Weather Climate Ext. 38*, 100495. https://doi.org/10.1016/j.wace.2022.100495

Alijani, B., O'Brien, J., and *Yarnal, B*. 2008. Spatial analysis of precipitation intensity and concentration in Iran. *Theor. Appl. Climatol. 94*(1), 107–124. https://doi.org/10.1007/s00704-007-0344-y

Almazroui, M., and *Saeed, S*. 2020. Contribution of extreme daily precipitation to total rainfall over the Arabian Peninsula. *Atmos. Res. 231*, 104672. https://doi.org/10.1016/j.atmosres.2019.104672

Ayugi, B., Zhihong, J., Zhu, H., Ngoma, H., Babaousmail, H., Rizwan, K., and *Dike, V*. 2021. Comparison of CMIP6 and CMIP5 models in simulating mean and extreme precipitation over East Africa. *Int. J. Climatol 41*, 6474–6496. https://doi.org/10.1002/joc.7207

Balling, R. C., Keikhosravi Kiany, M. S., Sen Roy, S., and *Khoshhal, J*. 2016. Trends in extreme precipitation indices in Iran: 1951–2007. *Adv. Meteorol 2016*. ID 2456809. https://doi.org/10.1155/2016/2456809

Chen, H., Sun, J., Lin, W., and *Xu, H*. 2020. Comparison of CMIP6 and CMIP5 models in simulating climate extremes. *Sci. Bull. 65*, 1415–1418.https://doi.org/10.1016/j.scib.2020.05.015

Darand, M. 2020. Projected changes in extreme precipitation events over Iran in the 21st century based on CMIP5 models. *Climate Res. 82*, 75–95.https://doi.org/10.3354/cr01625

Darand, M., and *Pazhoh, F*. 2022. Spatiotemporal changes in precipitation concentration over Iran during 1962–2019. *Climatic Change*, *173*(3), 1–22.https://doi.org/10.1007/s10584-022-03421-z

Dizaji, R. A., Ardalan, A., and *Fatemi, F*. 2019. Response functions in disasters: Iran flash flood 2016. *Dis. Medicine Public Health Prepar. 13*, 842–844. https://doi.org/10.1017/dmp.2018.94

Domroes, M., Kaviani, M., and *Schaefer, D:* 1998. An analysis of regional and intra-annual precipitation variability over Iran using multivariate statistical methods. *Theor. Appl. Climatol. 61*, 151-159.

Easterling, D. R., Evans, J. L., Groisman, P. Y., Karl, T. R., Kunkel, K. E., and *Ambenje, P*. 2000. Observed variability and trends in extreme climate events: a brief review. *Bull. Amer. Meteorol. Soc. 81*(3), 417–426.https://doi.org/10.1175/1520-0477(2000)081<0417:OVATIE>2.3.CO;2

Fathian, F., Ghadami, M., Haghighi, P., Amini, M., Naderi, S., and *Ghaedi, Z*. 2020. Assessment of changes in climate extremes of temperature and precipitation over Iran. *Theor. Appl. Climatol. 141*(3), 1119–1133. https://doi.org/10.1007/s00704-020-03269-2

Fazel-Rastgar, F. 2020. Extreme weather events related to climate change: widespread flooding in Iran, March–April 2019. *SN Appl. Sci. 2*(12), 1–14.https://doi.org/10.1007/s42452-020-03964-9

Jian-Qi, S. 2012. The contribution of extreme precipitation to the total precipitation in China. *Atmos. Oceanic Sci. Lett. 5*(6), 499–503.https://doi.org/10.1080/16742834.2012.11447046

Karimi, S., Nazaripour, H., and *Hamidianpour, M*. 2021. Spatial and temporal variability of precipitation extreme indices in arid and semi-arid regions of Iran for the last half-century. *Időjárás 125*, 83–104.https://doi.org/10.28974/idojaras.2021.1.4

Kunkel, K.E., Pielke, R.A., and *Changnon, S. A*. 1999. Temporal fluctuations in weather and climate extremes that cause economic and human health impacts: A review. *Bull. Amer Meteorol Soc 80*(6), 1077–1098.https://doi.org/10.1175/1520-0477(1999)080<1077:TFIWAC>2.0.CO;2

Mahbod, M., and *Rafiee, M. R*. 2021. Trend analysis of extreme precipitation events across Iran using percentile indices. *Int. J. Climatol.41*, 952–969.https://doi.org/10.1002/joc.6708

Miri, M., Raziei, T., Zand, M., and *Kousari, M. R*. 2023. Synoptic aspects of two flash flood-inducing heavy rainfalls in southern Iran during 2019–2020. *Nat. Hazards 115*, 2655–2672. https://doi.org/10.1007/s11069-022-05658-4

Najafi, M. R., and *Moazami, S*. 2016. Trends in total precipitation and magnitude–frequency of extreme precipitation in Iran, 1969–2009. *Int. J. Climatol 36*, 1863–1872. https://doi.org/10.1002/joc.4465

Nazaripour, H., and *Mansouri Daneshvar, M. R*. 2014. Spatial contribution of one-day precipitations variability to rainy days and rainfall amounts in Iran. *Int. J. Environ. Sci. Technol. 11*, 1751–1758. https://doi.org/10.1007/s13762-014-0616-x

Nourani, V., and *Najafi, H*., 2022: Historical changes in hydroclimatic extreme events over Iran. In Climate Impacts on Extreme Weather Elsevier. 101–115. https://doi.org/10.1016/B978-0-323-88456-3.00001-0

Rousta, I., Soltani, M., Zhou, W., and *Cheung, H.H*. 2016: Analysis of extreme precipitation events over central plateau of Iran. *Amer. J. Climate Change 5*, 297–313. https://doi.org/10.4236/ajcc.2016.53024

Sen, P. K. 1968. Estimates of the regression coefficient based on Kendall's tau. *J. Amer. Stat. Assoc. 63*, 1379–1389. https://doi.org/10.1080/01621459.1968.10480934

Shadmani, M., Marofi, S., and *Roknian, M*. 2012. Trend analysis in reference evapotranspiration using Mann-Kendall and Spearman's Rho tests in arid regions of Iran. *Water Resour. Manage. 26*, 211–224. https://doi.org/10.1007/s11269-011-9913-z

Sharifi, L., and *Bokaie, S.* 2019. Priorities in prevention and control of flood hazards in Iran 2019 massive flood. *Iranian J. Microbiol.* 11(2), 80–84.

Zarrin, A., and *Dadashi-Roudbari, A*. 2022. Spatiotemporal Variability, Trend, and Change-Point of Precipitation Extremes and Their Contribution to the Total Precipitation in Iran. *Pure and Appl. Geophys. 179*, 2923–2944. https://doi.org/10.1007/s00024-022-03098-6

Zarrin, A., Dadashi-Roudbari, A., and *Hassani, S*. 2022. Future changes in precipitation extremes over Iran: Insight from a CMIP6 bias-corrected multi-model ensemble. *Pure Appl. Geophys.* 179, 441–464. https://doi.org/10.1007/s00024-021-02904-x

DOI:10.28974/idojaras.2024.3.6

IDŐJÁRÁS

Quarterly Journal of the HungaroMet Hungarian Meteorological Service
Vol. 128, No. 3, July – September, 2024, pp. 379–398

Forecasting extreme precipitations by using polynomial regression

Fatih Dikbaş

Pamukkale University, Civil Engineering Department, Denizli, Turkey

Author E-mail: f_dikbas@pau.edu.tr

(Manuscript received in final form September 18, 2023)

Abstract— It is well known that the recent global warming intensifies the magnitude of rainfalls due to the increase in water content in the atmosphere. Therefore, the probability of exceeding the previously observed extreme precipitation values also increases with the experienced climate change, and forecasting extreme weather events is becoming more important. This paper presents a new polynomial regression approach and software (PolReg), where future extreme precipitations exceeding all previous observations are estimated for each month of year by using prediction bounds with a level of certainty at 95%. The presented method determines the degrees and coefficients of best-fitting polynomials for each precipitation station and forecasts the expected extreme value for each month of year by using the determined polynomials. The performance of the method is tested by removing and estimating a total of 792 highest observed monthly total precipitation values of 66 precipitation stations in Turkey (the highest observation for each month of year for each station). The results show that the proposed method and the provided software have a high performance and accuracy in estimating future precipitation extremes and might be applied in many disciplines dealing with forecasting probable extreme values.

Key-words: forecasting extreme precipitations, polynomial regression, data-driven modeling, hydrometeorology, Turkey

1. Introduction

Precipitation is one of the principal atmospheric forcing parameters required for hydrologic modeling (*Liu and Coulibaly* 2011). The forecasting of precipitation extremes is becoming more important with the worldwide increase in the frequency and intensity of water-related disasters like floods and droughts and dwindling water supplies (*Baxevani and Wilson* 2018; *Fowler et al.* 2010; *Leconte et al.* 2013; *McElroy* 2016). These forecasts can provide estimates of probabilities of having more (or less) precipitation than certain specified amounts (*Unkašević et al.* 2004). Understanding the variability and forecasting the probable extreme values of precipitation are also highly important for the efficient prevention of potential natural disasters (*Beguería and Vicente-Serrano* 2006; *Bhatia et al.* 2019; *Block and Rajagopalan* 2007; *Keupp et al.* 2019; *Tian et al.* 2014; *Yuan et al.* 2017). Accurate determination of design rainfall directly influences the selection of appropriate dimensions for water structures and prevents loss of lives and environmental damage (*Zhang et al.* 2021). With the impact of climate change and abnormal weather caused by the recent global warming, the magnitude of precipitation is likely to intensify in most regions of the world as indicated by both observations and climate model simulations (*Hou et al.* 2014; *Ibrahim* 2019; *Lazoglou et al.* 2019; *Li et al.* 2019; *Rai et al.* 2019; *Reager and Famiglietti* 2009; *Zhang et al.* 2013). For example, *Schönwiese et al.* (2003) have demonstrated that the increase in extreme wet months is reflected in a systematic increase in the variance and the Weibull probability density function parameters, respectively. Although there is a relative agreement in climate change scenarios about changes in extremes, significant differences in the magnitudes of extremes have been reported (*Kyselý and Beranová* 2009; *Meena et al.* 2019; *Zhao et al.* 2019). Observations indicate that there is a continuous change in the climate (*Knox* 1993) and consequently in the hydrological cycle and associated rainfall patterns (*Zhang et al.* 2009). A study on the changes in flood frequency over paleo-timescales demonstrated that the estimated flood exceedance probability can increase quite rapidly over time (*Porporato and Ridolfi* 1998). Due to these reasons, the changing character of return periods of precipitation extremes should be considered in the hydrological design and water resources management studies (*Su et al.* 2009).

Hydrologic variables depict a two-dimensional periodic behavior because of seasonality associated with the hydrologic cycle (*Dikbas* 2017a; *Dikbas* 2017b). For example, precipitation generally shows significant variations throughout a year, but the observations in the sub-periods (months, seasons, etc.) tend to be in a definite range, and alternating trends might be observed for a station in different months of the year (*Trömel and Schönwiese* 2007). In Turkey, minimum precipitations are generally observed in the July-September (summer) period varying in a low range, while the highest precipitations are mostly experienced within the November-January (winter) period. Though precipitation is normally

seasonal, its uncertain (*Kent et al.* 2015), nonstationary, and sometimes chaotic behavior (*Sivakumar* 2000; *Sivakumar et al.* 1999; *Wilks* 2012) makes the observation, quantification, estimation, and forecasting of precipitation challenging (*Gao et al.* 2017; *Schliep et al.* 2010; *Wang and Lin* 2015). The two-dimensional behavior of precipitation can be observed when the data series are placed on a matrix so that each row contains observations for each month (12 rows). This approach provides significant advantages in data-driven modeling studies over the one-dimensional approach and allows obtaining accurate modeling results and estimations as in the 3D imputation (*Dikbas* 2016b), frequency-based imputation (*Dikbas* 2016a; *Dikbas* 2017b), and two-dimensional correlation methods (*Dikbas* 2017a, 2018a; *Dikbas* 2018b) which use data located on a two-dimensional matrix.

It can be visually observed that the time series graphs of sorted monthly total precipitation series generally depict a nonlinear behavior and the slope of the curve always increases towards the higher values. This property of the precipitation series was the main reason for the selection of polynomial regression as the method for estimating future extreme values. Polynomial regression can be used to describe trend curves to model complicated patterns of sorted temporal data. Together with its applications on various hydrological data, some studies making use of polynomial regression for modeling precipitation also exist in literature (*Acock* and *Pachepsky* 2000; *Adnan et al.* 2016; *Block and Rajagopalan* 2007; *George et al.* 2016; *Goodale et al.* 1998; *Hwang et al.* 2012; *Stefanescu et al.* 2014; *Tian et al.* 2014). This study presents a methodology and software for reliably estimating expected future extreme monthly total precipitation values exceeding all previous observations of a station for each month of the year by applying univariate polynomial regression on the observed precipitation values of the investigated station itself. The prediction bounds for each monthly series are determined by using a 95% confidence level. The observations are located on two-dimensional matrices where months are in rows. The application of the developed method on 66 precipitation observation stations in Turkey has shown that the method successfully estimates the removed extreme observations. The extreme precipitation values expected with a high occurrence probability in the future were also calculated for all months for all stations. The forecasted extreme precipitation values have values exceeding all previous observations and provide crucial information especially to be considered in water resources management projects. The proposed method has a flexible structure in that new observations can be easily appended to the existing input dataset, and the best-fitting polynomials might be updated accordingly allowing consideration of the non-stationarity of the precipitation series. The results obtained for the station 18-003 are reported to illustrate the details of the developed methodology as presented in Section 3, and the summary of obtained results for all stations are presented in Section 4.

2. Study area and data

The developed method and the provided software were tested on 66 precipitation observation stations across 20 different basins in Turkey (*Fig. 1*). The figure shows the average annual precipitation values in Turkey between 1981 and 2010. The selected stations represent the majority of the climate and elevation zones and cover most of the hydrological basins in Turkey. The climate in Turkey is moderately dry with higher average precipitation in the coastal regions. Average annual total precipitation varies between 250 mm (Salt Lake region) and 2300 mm (Rize region on the coast of the Black Sea). The Black Sea coastline receives precipitation throughout the year and the Aegean and Mediterranean coasts are wet in winter but dry during the summer seasons.

Fig. 1. Map of 1981–2010 average annual precipitation in Turkey, including the locations of the 66 stations used in this study.

The descriptive statistics for all stations, including percentiles and best-fitting distributions are outlined in *Table 1*. The majority of precipitation series (46/66) fit the Wakeby distribution. The probability distributions for all stations are positively skewed and leptokurtic (except for station 21-007) as shown by the skewness and excess kurtosis measures. The maximum observations of all stations constitute the lower limit for the estimations of the expected next extreme precipitation, and the maximum observations vary between 123.0 mm (station 15-010) and 893.5 mm (station 08-006).

Table 1. Descriptive statistics, percentiles, and best-fitting distributions for the first ten stations. The complete table for all stations is provided as an online supplement because of space restrictions.

	Station	01-004	01-005	01-008	02-004	02-009	02-011	02-012	03-009	03-013	03-027
	Elevation (m)	90	395	395	35	40	10	180	20	770	240
Statistic	**Sample Size**	492	492	480	456	492	468	456	480	528	516
	Mean	42.3	54.0	46.4	69.3	77.8	47.2	82.5	46.3	55.6	52.2
	Variance	1139	1627	1331	3015	4301	1541	5073	1755	2680	1420
	Std. Error	1.52	1.83	1.68	2.60	2.99	1.82	3.39	1.93	2.25	1.69
	Skewness	1.11	1.04	1.45	1.18	1.55	1.27	1.66	1.50	1.44	0.78
	Excess Kurtosis	1.06	1.01	3.56	2.07	2.76	2.21	4.02	4.14	2.91	0.28
Percentiles	**Min**	0.0	0.0	0.0	0.0	0.2	0.0	0.0	0.0	0.0	0.0
	5%	1.2	3.0	4.6	4.2	7.0	1.7	4.6	0.0	0.3	1.2
	10%	4.6	8.0	7.8	7.8	13.4	4.4	10.2	2.3	2.3	7.7
	25% (Q1)	17.0	24.2	18.5	26.8	30.1	17.1	31.8	13.2	15.2	22.6
	50% (Median)	33.8	46.1	38.7	56.5	61.8	38.0	64.5	36.2	42.9	46.0
	75% (Q3)	60.0	77.9	65.0	101.1	103.3	70.5	114.5	66.8	83.0	74.7
	90%	89.6	107.6	93.3	142.0	165.6	98.0	171.1	107.8	129.6	105.0
	95%	111.1	134.3	117.6	174.5	211.2	117.8	225.2	123.6	154.3	122.4
	Max	170.1	205.0	264.3	365.5	351.0	242.5	476.5	315.9	320.5	184.1
	Best-fit Distr.	WAK	WAK	WAK	WAK	WAK	WAK	WAK	WAK	BETA	WAK

https://www.dropbox.com/scl/fi/48xw7tbif7qoeiuocqhvh/Table.1.Descriptive.Statistics.and.Quantiles.-Full.Version.Supplement.xlsx

3. Polynomial regression

Polynomial regression is intrinsically a form of multiple linear regression. The polynomial regression model can be expressed as follows:

$$y_i = a_0 x_i^m + a_1 x_i^{m-1} + a_2 x_i^{m-2} + \cdots + a_{m-2} x_i^2 + a_{m-1} x_i + a_m + \varepsilon_i \quad (i = 1, 2, \ldots, n), \tag{1}$$

where n is the number of observations to which the polynomial function is fit, m is the degree of the polynomial to be fit to the observations, y_i is the ith element of the response vector containing the observations (the dependent variable), a_j is the coefficients (parameters) of the fitted polynomial (j = 1, 2, … , m), ε_j is the

random error (the difference between the estimation and observation), and x_i is the ith element of the vector containing the independent variable.

Eq.(1) can be expressed in matrix form as follows:

$$\begin{bmatrix} y_1 \\ y_2 \\ y_3 \\ \vdots \\ y_n \end{bmatrix} = \begin{bmatrix} x_1^m & x_1^{m-1} & x_1^{m-2} & \dots & x_1^2 & x_1 & 1 \\ x_2^m & x_2^{m-1} & x_2^{m-2} & \dots & x_2^2 & x_2 & 1 \\ x_3^m & x_3^{m-1} & x_3^{m-2} & \dots & x_3^2 & x_3 & 1 \\ \vdots & \vdots & \vdots & & \vdots & \vdots & \vdots \\ x_n^m & x_n^{m-1} & x_n^{m-2} & \dots & x_n^2 & x_n & 1 \end{bmatrix} \begin{bmatrix} a_0 \\ a_1 \\ a_2 \\ \vdots \\ a_m \end{bmatrix} + \begin{bmatrix} \varepsilon_1 \\ \varepsilon_2 \\ \varepsilon_3 \\ \vdots \\ \varepsilon_n \end{bmatrix} . \quad (2)$$

As shown with the examples below, the sorted precipitation series mostly have curved shapes far from being linear and the sections with high precipitation values generally have a higher slope than the lower values. The polynomial regression method presented in this paper determines the degrees (m) and coefficients (a_0, a_1, … , a_m) of the polynomials best fitting to the precipitation series of a station for each month of the year (12 observation series and 12 polynomials for each station) with a level of certainty at 95%. The series in each month are sorted in ascending order before fitting the polynomial function. Thus, in Eq.(2), y_1 stands for the minimum and y_n stands for the maximum observation in an individual month for which the polynomial is being fit. The precipitation series are not evaluated as a whole because of the seasonal variations in the behavior of precipitation. Therefore, 12 polynomial functions are determined for each station. Then, for each month, estimation of the next probable extreme precipitation (y_{n+1}) becomes possible by using the determined best-fitting polynomial function. The details of the implemented approach are presented below for the selected station 18-003 (Uzunpınar) located in the central region of Kayseri, Sivas, and Malatya cities.

4. Results

4.1. Forecasting extreme precipitation for June for station 18-003

Estimation of the expected highest monthly precipitation exceeding all the previous observations for each month of year is the main aim of the method presented in this manuscript. The raw time series data of precipitation generally has complicated quantitative and temporal associations as shown in the heatmap of the observations of the station 18-003 for the 46 years between 1960 and 2005 (top panel in *Fig. 2*). This complicated behavior makes estimation of precipitation more challenging than other hydrologic variables like streamflow. When the return period is not the primary interest, sorting the observations is one of the mostly applied methods for assessing quantitative associations in precipitation

observations. Therefore, prior to making estimations of extreme precipitation values, all rows containing the observations for each month are sorted in ascending order. The bottom panel in *Fig. 2* shows the heatmap of the sorted precipitation observations of the station 18-003. The sorted values generate monotonically increasing series making estimation of the next highest value probable by using polynomial regression. The values to be estimated will constitute the 47th column in the bottom panel in *Fig. 2,* and they are calculated by separately determining the polynomial equations representing the relationships for all the series in the 12 rows of the horizontally sorted data matrix. Consequently, 12 polynomials fitting to the sorted precipitation series for each month of year are obtained for each station, because there are significant differences in the behavior of the precipitation series in view of both expected and observed precipitation amounts for each month of year.

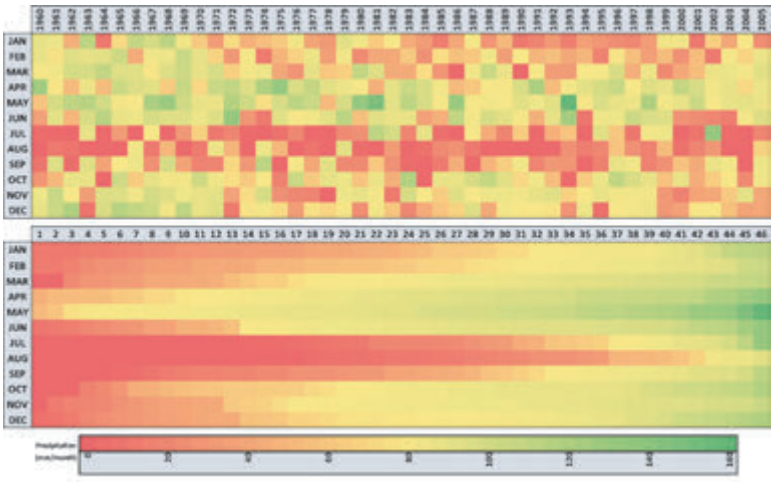

Fig. 2. Heatmaps of the monthly total precipitation observations of station 18-003 (top) and the row-wise sorted values (bottom).

For finding the best fitting polynomial for each row, the developed PolReg software (the link to the freely distributed code of the software is provided at the end of the manuscript above the References) fits polynomials from 2nd to 8th degree and calculates the performance of each fit by using 11 different statistical measures (mean squared error (MSE), normalized mean squared error (NMSE), root mean squared error (RMSE), normalized root mean squared error (NRMSE), mean absolute error (MAE), mean bias error (MBE), coefficient of correlation (r), coefficient of determination (D), coefficient of efficiency (E), maximum absolute

error (MaxAE), and mean absolute scaled error (MASE)). The software automatically generates plots of all fitted polynomials.

Fig. 3 shows the plots of the polynomials generated for the sorted observations of station 18-003 in the month of June during the 46 years. The blue points are the observed values and the grey point on the right of each panel shows the next expected value determined by simply calculating the y-value of the function of the fitted polynomial corresponding to the 47th observation on the x-axis. The plots in each panel show the fitted polynomials starting from the 2nd degree up to the 8th degree. The green dashed lines indicate the prediction bounds with a level of certainty at 95%. This interval indicates that there is a 95% chance that the new observation is contained within the lower and upper prediction bounds.

The highest observed values are out of the prediction bounds of the fitted polynomials in the plots for the second- and third-degree polynomials. Also, the expected next-extreme precipitations are lower than the highest observed values for the second- and third-degree polynomials. Consequently, the plots obtained for the polynomials with a degree of 4 and higher fit the sorted series better and provide more accurate estimates for the next highest expected precipitation as shown in the plots for June.

The plots of the polynomials do not provide sufficient clues for deciding on the best-fitting polynomial. The PolReg software calculates 11 statistical performance measures for each fitted polynomial, and the user determines the best-fitting polynomial by evaluating the plots and the performance tables together. The software generates a results table for each month and summarizes the results of the fitting procedure. *Table 2* shows the outputs obtained for the month of June. The table contains the coefficients of each fitted polynomial (a_0 to a_8); the maximum precipitation value observed in the evaluated month (Max: 107.60 mm for June which was observed in 1972); the estimated maximum value by the fitted polynomial (EstMax); the expected next highest precipitation forecasted by the fitted polynomial (EstNextMax); the upper (PredIntU(n)) and the lower (PredIntL(n)) limits of the prediction interval for the estimated maximum precipitation corresponding to the observed maximum precipitation, and the upper (PredIntU(n+1)) and lower (PredIntL(n+1)) limits of the prediction interval for the expected next maximum precipitation. Here, n is the number of observations used for fitting the polynomials and making the estimations (n = 46 for the station 18-003). The polynomials from the 5th to the 8th degree produced estimates between 106.25 mm and 108.03 mm for the observed maximum (which is 107.60 mm for June) and between 122.03 mm and 127.17 mm for the expected next maximum precipitation. The software also reports the statistical performance indicators between the observed values and the fitted polynomials. The best performances are indicated with green background and the worst performances are indicated with a red background color. For the month of June, for the station 18-003, the performance measures point out that the 8th-degree polynomial best fits the observations.

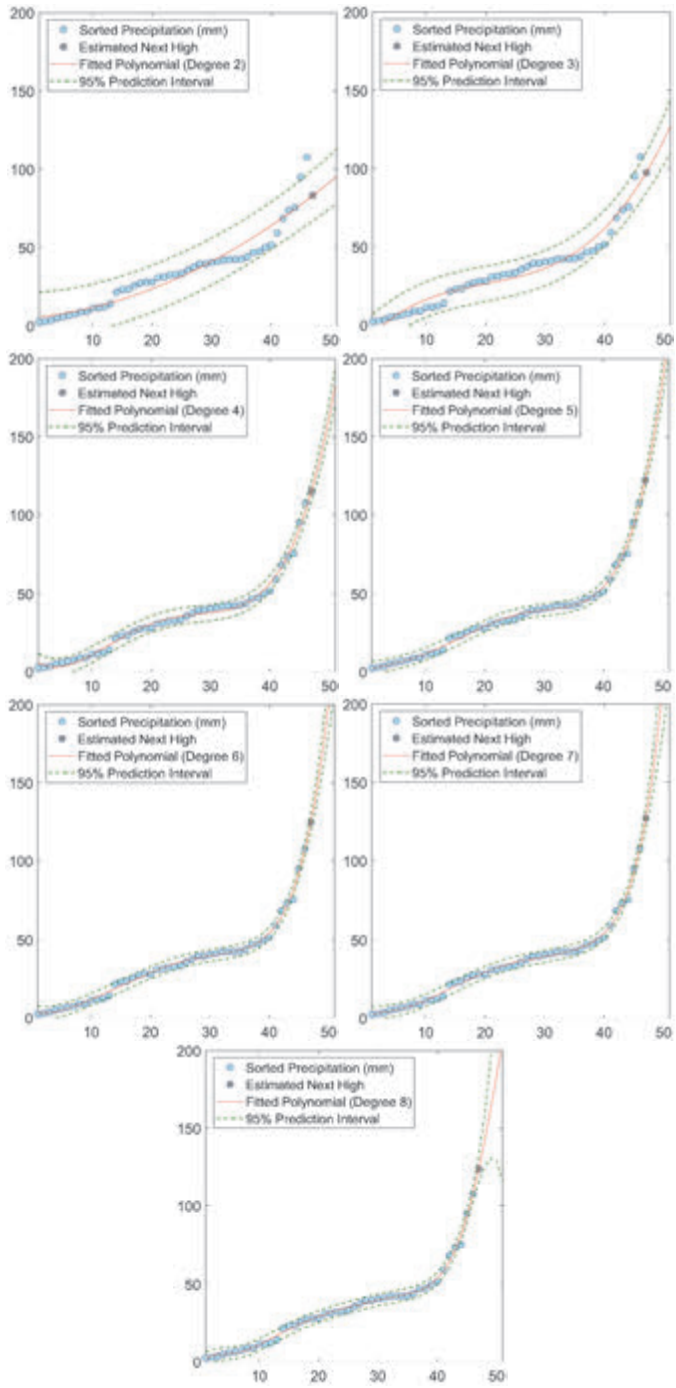

Fig. 3. Plots of the 2nd to the 8th degree polynomials fitted to the sorted 46-year-long monthly total precipitation observations of the station 18-003 in June.

In the case of research on extreme values, a function that generally has a good fit to most of the observed values but not to the extreme values should not be regarded as a good fit. This situation is clearly depicted by the 2nd and 3rd degree polynomials which have an r score of 0.954 and 0.975, respectively (scores which might be regarded as a high correlation), but they are far from representing the extreme values even though they generally have a good fit to the lower observations. Therefore, for providing more clues on the best fitting polynomials, the software also calculates the 11 statistical performance indicators between the highest five observations and the values of the fitted polynomials corresponding to the observed extremes and reports them at the bottom section of the output table.

The statistical measures for the extreme values in June indicate that the 7th degree polynomial fits best to the observed extremes. Consequently, by looking at the plots and the table, it might be concluded that a monthly total precipitation value up to 127.17 mm might be expected in June in the station 18-003 with a prediction bound between 119.93 mm and 134.42 mm at 95% confidence level.

Table 2. Output table summarizing the polynomial fits and statistical measures for the 46-year-long monthly total precipitation observations of the station 18-003 in June

JUNE							
Pol.Deg.:	2	3	4	5	6	7	8
a_0	0.0272	0.0026	0.0002	0.0000	0.0000	0.0000	0.0000
a_1	0.3828	-0.1558	-0.0180	-0.0005	0.0000	0.0000	0.0000
a_2	5.1129	3.8600	0.4724	0.0136	0.0007	0.0001	0.0000
a_3		-9.2332	-2.8683	-0.0955	-0.0167	-0.0035	0.0008
a_4			8.1035	1.1139	0.2708	0.0557	-0.0184
a_5				0.9243	-0.7247	-0.3679	0.2493
a_6					3.4269	1.7129	-1.6842
a_7						0.7807	5.7060
a_8							-2.8217
Max	107.60	107.60	107.60	107.60	107.60	107.60	107.60
EstMax	80.25	91.30	102.52	106.25	107.25	108.03	107.29
EstNextMax	83.16	97.51	114.85	122.03	124.53	127.17	123.57
PredIntU(n)	96.22	103.80	108.46	110.91	111.98	112.84	112.12
PredIntL(n)	64.29	78.80	96.58	101.60	102.52	103.22	102.45
PredIntU(n+1)	99.36	110.55	121.37	127.54	130.76	134.42	132.14
PredIntL(n+1)	66.97	84.47	108.33	116.51	118.30	119.93	115.00
Goodness of Fit Measures for the Whole Series:							
MSE	**49.6702**	27.0253	5.4196	2.9826	2.7899	2.6524	**2.4943**
NMSE	**0.0877**	0.0477	0.0096	0.0053	0.0049	0.0047	**0.0044**
RMSE	**7.0477**	5.1986	2.3280	1.7270	1.6703	1.6286	**1.5793**
NRMSE	**0.2961**	0.2184	0.0978	0.0726	0.0702	0.0684	**0.0664**
MAE	**4.9392**	4.2176	1.8697	1.2329	1.2182	1.2013	**1.1155**
MBE	0.0000	**0.0000**	0.0000	0.0000	0.0000	0.0000	**0.0000**
r	**0.9541**	0.9753	0.9951	0.9973	0.9975	0.9976	**0.9977**
d	**0.9104**	0.9512	0.9902	0.9946	0.9950	0.9952	**0.9955**
E	**0.9104**	0.9512	0.9902	0.9946	0.9950	0.9952	**0.9955**
MaxAE	**27.3472**	16.2979	6.8502	6.3976	5.9546	**5.3896**	6.0817
MASE	**2.1088**	1.8007	0.7983	0.5264	0.5201	0.5129	**0.4763**
Goodness of Fit Measures for the Highest 5 Values:							
MSE	**213.1992**	76.8190	17.1623	11.7163	11.4662	**11.4318**	12.1024
NMSE	**0.7762**	0.2797	0.0625	0.0427	0.0417	**0.0416**	0.0441
RMSE	**14.6013**	8.7646	4.1427	3.4229	3.3862	**3.3811**	3.4789
NRMSE	**0.8810**	0.5288	0.2500	0.2065	0.2043	**0.2040**	0.2099
MAE	**9.6929**	6.7377	3.4075	2.8099	**2.7652**	2.9008	2.8112
MBE	**9.4325**	3.6221	0.4461	**0.2509**	0.3834	0.5720	0.3786
r	**0.9532**	0.9604	0.9691	0.9732	0.9750	**0.9771**	0.9740
d	**0.9085**	0.9223	0.9391	0.9470	0.9506	**0.9547**	0.9487
E	**0.0298**	0.6504	0.9219	0.9467	0.9478	**0.9480**	0.9449
MaxAE	**27.3472**	16.2979	6.8502	6.3976	5.9546	**5.3896**	6.0817
MASE	**0.9916**	0.6893	0.3486	0.2875	**0.2829**	0.2968	0.2876

4.2. Model validation

The exceedance probabilities for the observed and estimated highest values of the station 18-003 for each month are calculated by using the best-fitting distributions (*Table 3*). The parameters of the best fitting distributions and the probabilistic estimates determined by using the inverse cumulative distribution function for $p=1-(1/46)=0.97826$ are also presented for a comparison of expected and experienced observations for the investigated period. EasyFit software was used for deciding the best fitting distributions. The used software makes goodness of fit tests according to the Kolmogorov-Smirnov, Anderson-Darling, and chi-squared tests. The software supports 55 continuous and discrete distributions and sorts the tested distributions according to their scores in the goodness of fit tests. The distribution with the highest scores is regarded as the best fitting distribution. Then, the exceedance probabilities are calculated based on the parameters of the best-fitting distribution. It must not be forgotten that the return period of any observed extreme event is not equal to the investigated period, because the observed extreme might always have a much longer (or even shorter) return period. The selected observation period and the observed extremes should never be regarded as dependent variables. This situation is also pointed out by the exceedance probabilities determined for the observations used in this study, where the exceedance probabilities are very low for some months, even though all of the highest values were experienced within the investigated 46-year period. For example, the exceedance probabilities of the observed extremes for five months (March, June, July, September, and November) vary between 1% and 1.3% based on the best-fitting distributions. The exceedance probabilities calculated for the forecasted future extreme precipitations provide clues about the probable return periods of extreme events. Even though the return periods for some forecasts seem to be long, the experienced extreme values in the evaluated period show that the forecasted future extremes are not far from that being expected.

As another method applied for testing the performance of polynomial regression in the estimation of the observed highest values, all highest observed values for each month of year in each dataset (12 values for each station and a total of 792 extremes) were removed from the datasets, and polynomial regression was used for estimating the removed extremes. An output table was also generated for the calculations (*Table 4*) presenting the results for June for the station 18-003 after the highest value observed in June 1972 (107.60 mm) was removed from the dataset.

The results obtained by the best fitting 2nd and the 3rd degree polynomials were again far from forecasting the deliberately removed extreme value, but the 5th to the 8th degree polynomials all produced forecasts close to the removed value (104.62 mm to 109.38 mm), and the removed value is within the prediction intervals of the 5th to the 8th-degree polynomials. The software does not know the value of the removed extreme during the estimation process.

Table 3. Exceedance probabilities for the observed highest precipitations and estimated future extremes of the station 18-003 for each month of year

	Best-Fitting Distribution	X1*	X(P=0.98)	P(X>X1)	X2*	P(X>X2)
January	Log-Pearson 3	73.9	77.2	0.024	81.6	0.019
February	Inv. Gaussian (3P)	60.7	56.6	0.016	77.8	0.005
March	Wakeby	69.4	69.0	0.021	74.1	0.009
April	Johnson SB	109.1	100.8	0.011	129.7	0.001
May	Fatigue Life (3P)	154.5	147.8	0.018	186.9	0.007
June	Dagum	107.6	91.4	0.010	123.6	0.006
July	Gen. Extreme Value	109.0	75.1	0.011	157.0	0.006
August	Gen. Pareto	38.6	36.1	0.019	46.0	0.013
September	Gen. Pareto	72.5	62.1	0.012	94.2	0.003
October	Wakeby	82.0	78.0	0.017	88.8	0.010
November	Wakeby	63.5	58.0	0.013	72.7	0.006
December	Gen. Extreme Value	85.1	87.1	0.023	89.3	0.020

*X1: Highest observation; X(p=0.98): The probabilistic estimate determined by using the inverse cumulative distribution function for p=0.97826; X2: Forecasted extreme precipitation

Table 4. Output table summarizing the polynomial fits and the statistical measures for the month of June for station 18-003 after 12 highest observations for each month are removed from the input data

JUNE							
Pol.Deg.:	2	3	4	5	6	7	8
a_0	0.0176	0.0020	0.0002	0.0000	0.0000	0.0000	0.0000
a_1	0.7431	-0.1175	-0.0162	-0.0005	0.0000	0.0000	0.0000
a_2	2.9390	3.2557	0.4245	0.0111	0.0005	0.0001	0.0000
a_3		-7.2179	-2.4289	-0.0553	-0.0140	-0.0042	0.0009
a_4			7.1456	0.8672	0.2423	0.0670	-0.0206
a_5				1.3130	-0.5971	-0.4583	0.2747
a_6					3.2714	2.0250	-1.8428
a_7						0.4715	6.1469
a_8							-3.1902
Max	95.10	95.10	95.10	95.10	95.10	95.10	95.10
EstMax	71.93	79.70	88.91	91.90	92.66	93.47	92.73
EstNextMax	74.27	84.42	98.79	104.62	106.58	109.38	105.72
PredIntU(n-1)	84.48	90.29	94.37	96.56	97.46	98.34	97.63
PredIntL(n-1)	59.37	69.12	83.44	87.23	87.86	88.59	87.83
PredIntU(n)	87.01	95.49	104.81	110.18	112.96	116.82	114.56
PredIntL(n)	61.53	73.36	92.77	99.06	100.20	101.94	96.87

Table 4. Continued

Pol.Deg.:	2	3	4	5	6	7	8
Goodness of Fit Measures for the Whole Series:							
MSE	**30.5169**	19.2320	4.5448	2.9596	2.8440	2.6943	**2.5366**
NMSE	**0.0673**	0.0424	0.0100	0.0065	0.0063	0.0059	**0.0056**
RMSE	**5.5242**	4.3854	2.1318	1.7204	1.6864	1.6414	**1.5927**
NRMSE	**0.2595**	0.2060	0.1001	0.0808	0.0792	0.0771	**0.0748**
MAE	**3.9968**	3.4997	1.7008	1.2483	1.2448	1.2084	**1.1288**
MBE	**0.0000**	0.0000	0.0000	0.0000	0.0000	0.0000	**0.0000**
r	**0.9649**	0.9781	0.9949	0.9967	0.9968	0.9970	**0.9971**
d	**0.9311**	0.9566	0.9897	0.9933	0.9936	0.9939	**0.9943**
E	**0.9311**	0.9566	0.9897	0.9933	0.9936	0.9939	**0.9943**
MaxAE	**23.1737**	15.3962	6.1934	5.7482	5.7831	**5.5643**	6.0303
MASE	**1.8930**	1.6575	0.8055	0.5912	0.5896	0.5723	**0.5346**
Goodness of Fit Measures for the Highest 5 Values:							
MSE	**127.2844**	52.8151	13.8332	**11.1934**	11.3853	11.7789	12.1521
NMSE	**0.7347**	0.3048	0.0798	**0.0646**	0.0657	0.0680	0.0701
RMSE	**11.2820**	7.2674	3.7193	**3.3456**	3.3742	3.4320	3.4860
NRMSE	**0.8571**	0.5521	0.2826	**0.2542**	0.2564	0.2607	0.2648
MAE	**8.4804**	4.7540	3.1171	**2.7116**	2.8329	2.9437	2.9430
MBE	**7.0343**	3.0175	0.5262	**0.4096**	0.5197	0.7180	0.5309
r	**0.9458**	0.9506	0.9569	0.9597	0.9609	**0.9632**	0.9591
d	**0.8945**	0.9037	0.9157	0.9210	0.9234	**0.9277**	0.9200
E	**0.0817**	0.6189	0.9002	**0.9192**	0.9179	0.9150	0.9123
MaxAE	**23.1737**	15.3962	6.1934	5.7482	5.7831	**5.5643**	6.0303
MASE	**0.9475**	0.5312	0.3483	**0.3030**	0.3165	0.3289	0.3288

4.3. Forecasting the extreme values for the remaining 65 precipitation stations

The above discussion was generated based on estimations and observations for a single station (18-003). A method's ability to estimate values for a single station is not sufficient to claim that it will be successful in estimating values for other data series. To test the success of the application of the proposed polynomial regression approach across multiple stations, the presented software was used to estimate extreme precipitation values for 66 stations across Turkey. For each station, expected future extreme precipitations were estimated for each month, and the performance of polynomial regression was tested by estimating the removed extremes (a total of 792 observed extremes) as explained above. The scatterplots between the forecasts of the future extremes and the observed maximums for the investigated 65 stations (01-004 to 26-005) are provided as an online supplementary material (*Fig. S1*). The link to the online supplement is at the end of the manuscript above the References.

The success of polynomial regression in forecasting extremes might only be validated when the expected precipitations occur in real life, but testing the performance by removing and estimating the observed extremes has been used in literature as a reliable practice. The scatterplots and the correlations between the removed observed highest precipitation values and the estimations of the fitted polynomial functions show that the presented method is very successful in approximating the removed precipitation values with high accuracy. The closeness of the points in the scatterplots to the straight diagonal $y = x$ line (not shown in the figures) is an indicator of the estimation performance; the closer the points to the $y = x$ line are, the higher the performance is.

The figures show that the majority of the estimations are very close to the observations as it is indicated also by the correlations. 80.3% (53/66) of the correlations are over 0.9, while 65.2% (43/66) are over 0.95, and 15.2% (10/66) are over 0.99. The highest correlation (0.998) was obtained for station 03-027 and the lowest correlation (0.554) was observed for the station 01-004. In addition to correlation, the RMSE, NRMSE, E, and MAE measures between the removed and estimated precipitations are also calculated for all stations (*Table 5*). The values are calculated for the removed and forecasted 12 values for each month of year for each station as shown in the scatterplots in the supplementary materials.

Table 5. Statistical performance measures for the forecasts of the removed highest observations for the first ten stations. The complete table for all stations is provided as an online supplement because of space restrictions.

STATION	01-004	01-005	01-008	02-004	02-009	02-011	02-012	03-009	03-013	03-027
r	0.554	0.921	0.794	0.979	0.963	0.928	0.969	0.974	0.995	0.998
RMSE	29.592	16.897	21.283	24.045	27.685	23.139	30.992	24.823	8.137	2.111
NRMSE	0.233	0.120	0.149	0.126	0.112	0.164	0.131	0.166	0.050	0.015
NSE	-0.434	0.824	0.365	0.894	0.872	0.795	0.910	0.856	0.988	0.994
MAE	13.389	6.935	13.090	16.963	17.728	11.805	19.750	14.334	5.631	1.644

https://www.dropbox.com/scl/fi/n7yd7jos4x00e0cgenh44/Table.5.Performance.Measures.-Full.Version.Supplement.xlsx

Fig. 4 shows the annual averages of the observed and estimated precipitations together with the differences between observations and estimations. In the annual scale, highest future precipitation increases are expected in the southern and northwest shoreline regions. Figures for the monthly observations, estimations, and differences are presented as an online supplement in *Figs. S2-S13.* Those figures clearly show the expected variation of precipitation throughout the seasons.

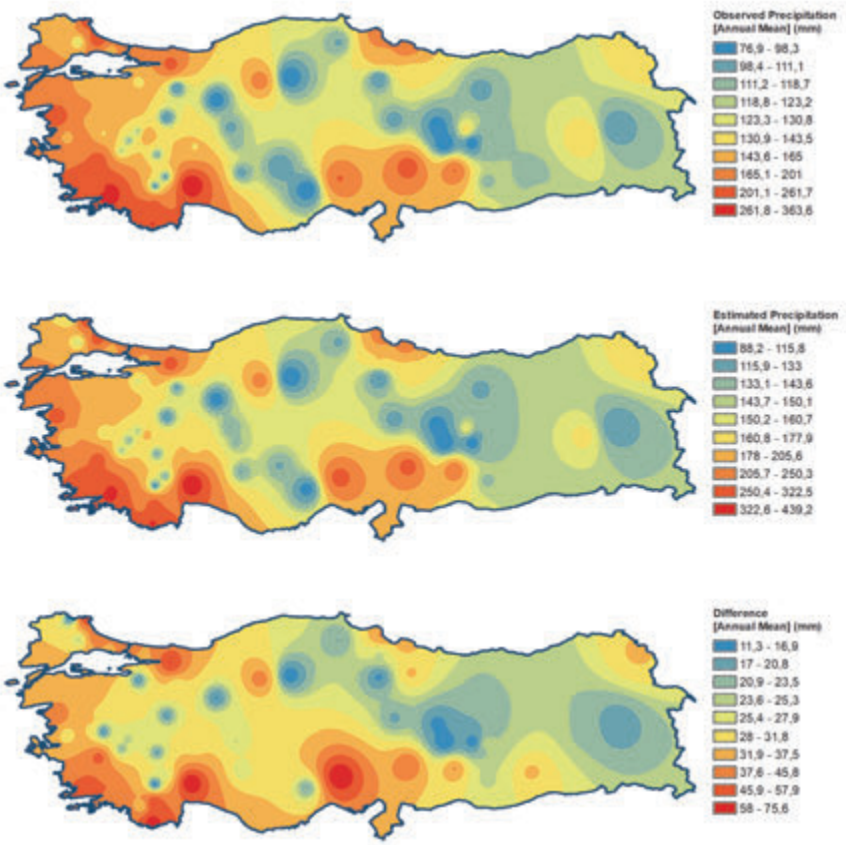

Fig. 4. Annual averages of the observed precipitation, the estimated higher precipitation, and the difference between the observed and the estimated higher precipitation.

In the winter months, extreme precipitation is mostly expected in the western half of the country, while the southern half has a risk of extreme precipitation in spring. Then, in summer, the extreme precipitation expectation moves toward the eastern half of the country, and finally, in autumn months, the northern half of the country seems to be prone to extreme precipitation. These findings fit well with the previously observed extremes showing a rotating motion over the country through the seasons.

Even though polynomials of a given degree provide an advantage in allowing the data to determine the fitted model in a somewhat more flexible way, polynomial regression sometimes suffers from various drawbacks. One disadvantage is that individual observations can exert an influence on remote parts of the curve (*Green* and *Silverman* 1993), and the polynomial regression may

suffer from severe extrapolation problems. It is also well-known that a polynomial with a higher order may fit the data better, but it may produce very weird estimators, especially for extrapolation.

In the presented case, the scatterplots show that a few highly unexpected precipitation values cause the decreases in correlations. For example, for station 01-004, the highest August precipitation was 149.3 mm (the 4th highest observation of the station among 492 observations), while all the remaining 40 August observations are under 44 mm. This very high precipitation value observed in summer was underestimated by all the fitted polynomials, and the correlation value decreased. Another difficulty in polynomial regression is that the model elaboration implicit in increasing the polynomial degree cannot be controlled continuously (*Green* and *Silverman* 1993). Therefore, the users of the presented method and software should be warned that some very rare extreme values might influence the performance of the model negatively, and both the statistical validations and the graphical outputs should be checked comparatively, especially for extremely rare cases. If these shortcomings of polynomial regression are experienced at an unacceptable rate in future uses, then the users might consider some sophisticated models, including local linear regression and penalized regression, which regulate the smoothness of the estimated mean structure but have their shortcomings like collinearity, sparsity, curse of dimensionality, and biased coefficient estimates.

The estimation performance of the presented method is directly associated with the amount and quality of the available data as it has a data-driven methodology. Therefore, it is expected that an even better performance should be expected when the data covers a longer range of observations and contains more information about the behavior of precipitation. An advantage of the method is that the best-fitting polynomials might be updated always as new observations are made. This approach allows consideration of the non-stationary structure of precipitation time series and provides a better opportunity for forecasting record values. A worldwide increase is reported in extreme precipitation values with the influence of global warming causing increased temperatures and evapotranspiration even in locations with decreasing precipitation trends. Consequently, there is an increasing requirement for alternative methods of estimating precipitation extremes showing extensive increases in frequency.

5. Conclusions

The method presented in this paper uses polynomial regression to forecast the most probable future monthly total precipitation exceeding all the previously observed precipitations for each month of the year. The method is applied to observations of 66 precipitation stations in Turkey. The results show that polynomial regression applied for the first time in literature with an approach as

presented in this paper can estimate expected precipitation extremes with high accuracy at a 95% confidence level. This result was obtained by removing and estimating the highest observed precipitations for each month of year for all stations. It is anticipated that the presented methodology and software might contribute to the overall improvement in the skill of forecasting extreme precipitation and other variables with similar behavior. Knowing probable future extreme precipitation values and their locations will allow us to take precautions against hazards in areas likely to experience these extremes, and loss of lives and property will hopefully be prevented.

The polynomial regression software developed for implementing the method is provided freely together with this manuscript. The software is distributed under the terms of the GNU General Public License version 3, and a copyright notice is provided at the beginning of the code.

Data Availability Statement:
Due to confidentiality agreements, supporting data can only be made available to bona fide researchers subject to a non-disclosure agreement. Details of the data and how to request access are available at https://www.turkiye.gov.tr/devlet-su-isleri-hidrometrik-veri-talebi.

Link to the online supplement containing Figures S1-S12:
https://www.dropbox.com/scl/fi/9ka40g5fsfiliakszifdt/Forecasting-Extreme-Precipitations.-Supplement.docx

Link to the code of PolReg software:
https://www.dropbox.com/scl/fi/iq3t8y3we3tikq8nmps79/PolReg.m

References

Acock, M.C. and *Y.A. Pachepsky*, 2000: Estimating missing weather data for agricultural simulations using group method of data handling. *J. Appl. Meteorol. 39*, 1176–1184. https://doi.org/10.1175/1520-0450(2000)039<1176:EMWDFA>2.0.CO;2

Adnan, S., K. Ullah, and *G. Shouting*, 2016: Investigations into precipitation and drought climatologies in south central Asia with special focus on Pakistan over the period 1951-2010. *J. Climate 29*, 6019–6035. https://doi.org/10.1175/JCLI-D-15-0735.1

Baxevani, A. and *R. Wilson*, 2018: Prediction of catastrophes in space over time. *Extremes 21*, 601–628. https://doi.org/10.1007/s10687-018-0314-z

Beguería, S. and *S.M. Vicente-Serrano*, 2006: Mapping the hazard of extreme rainfall by peaks over threshold extreme value analysis and spatial regression techniques. *J. Appl. Meteorol. Climatol 45*, 108–124. https://doi.org/10.1175/JAM2324.1

Bhatia, N., V.P. Singh, and *K. Lee*, 2019: Variability of extreme precipitation over Texas and its relation with climatic cycles. *Theor. Appl. Climatol. 138,* 449–467. https://doi.org/10.1007/s00704-019-02840-w

Block, P. and *B. Rajagopalan*, 2007: Interannual variability and ensemble forecast of upper Blue Nile basin Kiremt season precipitation. *J. Hydrometeorol.8*, 327–343. https://doi.org/10.1175/JHM580.1

Dikbas, F., 2016a: Frequency Based Prediction of Buyuk Menderes Flows. *Teknik Dergi 27*, *1*, 7325–7343.

Dikbas, F., 2016b: Three-dimensional imputation of missing monthly river flow data. *Scientia Iranica 23*, *1*, 45–53. https://doi.org/10.24200/sci.2016.2096

Dikbas, F., 2017a: A novel two-dimensional correlation coefficient for assessing associations in time series data. *Int. J. Climatol. 37*, 4065–4076. https://doi.org/10.1002/joc.4998

Dikbas, F., 2017b: Frequency-based imputation of precipitation. *Stoch. Environ. Res. Risk Asses. 31*, 2415–2434. https://doi.org/10.1007/s00477-016-1356-x

Dikbas, F., 2018a: A New Two-Dimensional Rank Correlation Coefficient. *Water Resour. Manage. 32*, 1539–1553. https://doi.org/10.1007/s11269-017-1886-0

Dikbas, F., 2018b: Compositional Correlation for Detecting Real Associations Among Time Series. In (eds. *Z. Prof. Yildirim, PhD, Gece Kitaplığı*) Academic Researches in Mathematic and Sciences, 27–46.

Fowler, H.J., D. Cooley, S.R. Sain, and *M. Thurston*, 2010: Detecting change in UK extreme precipitation using results from the climateprediction.net BBC climate change experiment. *Extremes 13*, 241–267. https://doi.org/10.1007/s10687-010-0101-y

Gao, L., J. Huang, X. Chen, Y. Chen, and *M. Liu*, 2017: Risk of extreme precipitation under nonstationarity conditions during the second flood season in the Southeastern Coastal Region of China. *J. Hydrometeorol.18*, 669–681. https://doi.org/10.1175/JHM-D-16-0119.1

George, J., L. Janaki, and *J. Parameswaran Gomathy*, 2016: Statistical Downscaling Using Local Polynomial Regression for Rainfall Predictions – A Case Study. *Water Resour. Manage. 30*, 183–193. https://doi.org/10.1007/s11269-015-1154-0

Goodale, C.L., J.D. Aber, and *S. V. Ollinger*, 1998: Mapping monthly precipitation, temperature, and solar radiation for Ireland with polynomial regression and a digital elevation model. *Climate Res. 10*, 35–49. https://doi.org/10.3354/cr010035

Green, P.J., and *B.W. Silverman*, 1993: Nonparametric Regression and Generalized Linear Models: A roughness penalty approach*.* Taylor & Francis. https://doi.org/10.1201/b15710

Hou, A.Y. and *Coauthors*, 2014: The global precipitation measurement mission. *Bull. Amer. Meteorol. Soc. 95*, 701–722. https://doi.org/10.1175/BAMS-D-13-00164.1

Hwang, Y., M. Clark, B. Rajagopalan, and *G. Leavesley*, 2012: Spatial interpolation schemes of daily precipitation for hydrologic modeling. *Stoch. Environ. Res. Risk Asses. 26*, 295–320. https://doi.org/10.1007/s00477-011-0509-1

Ibrahim, M.N., 2019: Generalized distributions for modeling precipitation extremes based on the L moment approach for the Amman Zara Basin, Jordan. *Theor. Appl. Climatol*. 138, 1075–1093 https://doi.org/10.1007/s00704-019-02863-3

Kent, C., R. Chadwick, and *D.P. Rowell*, 2015: Understanding Uncertainties in Future Projections of Seasonal Tropical Precipitation. *J. Climate 28*, 4390–4413. https://doi.org/10.1175/JCLI-D-14-00613.1

Keupp, L., E. Hertig, I. Kaspar-Ott, F. Pollinger, C. Ring, H. Paeth, and *J. Jacobeit*, 2019: Weighted multi-model ensemble projection of extreme precipitation in the Mediterranean region using statistical downscaling. *Theor. Appl. Climatol*. *138*, 1269–1295. https://doi.org/10.1007/s00704-019-02851-7

Knox, J. C., 1993: Large increases in flood magnitude in response to modest changes in climate. *Nature 361*, *6411*, 430–432. https://doi.org/10.1038/361430a0

Kyselý, J., and *R. Beranová*, 2009: Climate-change effects on extreme precipitation in central Europe: uncertainties of scenarios based on regional climate models. *Theor. Appl. Climatol*. *95*, 361–374. https://doi.org/10.1007/s00704-008-0014-8

Lazoglou, G., C. Anagnostopoulou, K. Tolika, and *F. Kolyva-Machera*, 2019: A review of statistical methods to analyze extreme precipitation and temperature events in the Mediterranean region. *Theor. Appl. Climatol*. *136*, 99–117. https://doi.org/10.1007/s00704-018-2467-8

Leconte, J., F. Forget, B. Charnay, R. Wordsworth, and *A. Pottier*, 2013: Increased insolation threshold for runaway greenhouse processes on Earth-like planets. *Nature 504*, *7479*, 268–271. https://doi.org/10.1038/nature12827

Li, F., X. Ju, W. Lu, and *H. Li*, 2019: A comprehensive analysis of spatial and temporal variability of extreme precipitation in the Nenjiang River Basin, Northeast China. *Theor. Appl. Climatol*. *138*, 605-616. https://doi.org/10.1007/s00704-019-02846-4

Liu, X., and *P. Coulibaly*, 2011: Downscaling ensemble weather predictions for improved week-2 hydrologic forecasting. *J. Hydrometeorol. 12*, 1564–1580. https://doi.org/10.1175/2011JHM1366.1

McElroy, T., 2016: On the measurement and treatment of extremes in time series. *Extremes 19*, 467–490. https://doi.org/10.1007/s10687-016-0254-4

Meena, H.M., D. Machiwal, P. Santra, P.C. Moharana, and *D.V. Singh*, 2019: Trends and homogeneity of monthly, seasonal, and annual rainfall over arid region of Rajasthan, India. *Theor. Appl. Climatol. 136*, 795–811. https://doi.org/10.1007/s00704-018-2510-9

Porporato, A. and *L. Ridolfi*, 1998: Influence of weak trends on exceedance probability. *Stoch. Hydrol. Hydraul. 12*, 1–14. https://doi.org/10.1007/s004770050006

Rai, P., A. Choudhary, and *A.P. Dimri*, 2019: Future precipitation extremes over India from the CORDEX-South Asia experiments. *Theor. Appl. Climatol*. 137, 2961–2975. https://doi.org/10.1007/s00704-019-02784-1

Reager, J.T. and *J.S. Famiglietti*, 2009: Global terrestrial water storage capacity and flood potential using GRACE. *Geophys. Res. Lett. 36*, *23*. https://doi.org/10.1029/2009GL040826

Schliep, E.M., D. Cooley, S.R. Sain, and *J.A. Hoeting*, 2010: A comparison study of extreme precipitation from six different regional climate models via spatial hierarchical modeling. *Extremes 13*, 219–239. https://doi.org/10.1007/s10687-009-0098-2

Schönwiese, C.-D., J. Grieser, and *S. Trömel*, 2003: Secular change of extreme monthly precipitation in Europe. *Theor. Appl. Climatol. 75*, 245–250. https://doi.org/10.1007/s00704-003-0728-6

Sivakumar, B., 2000: Chaos theory in hydrology: Important issues and interpretations. *J. Hydrol. 227*, 1–20. https://doi.org/10.1016/S0022-1694(99)00186-9

Sivakumar, B., S.Y. Liong, C.Y. Liaw, and *K.K. Phoon*, 1999: Singapore rainfall behavior: Chaotic? *J. Hydrol. Engin.4*, 38–48. https://doi.org/10.1061/(ASCE)1084-0699(1999)4:1(38)

Stefanescu, V., S. Stefan, and *F. Georgescu*, 2014: Spatial distribution of heavy precipitation events in Romania between 1980 and 2009. *Meteorol. Appl. 21*, 684–694. https://doi.org/10.1002/met.1391

Su, B., Z.W. Kundzewicz, and *T. Jiang*, 2009: Simulation of extreme precipitation over the Yangtze River Basin using Wakeby distribution. *Theor. Appl. Climatol. 96*, 209–219. https://doi.org/10.1007/s00704-008-0025-5

Tian, D., C.J. Martinez, W.D. Graham, and *S. Hwang*, 2014: Statistical Downscaling Multimodel Forecasts for Seasonal Precipitation and Surface Temperature over the Southeastern United States. *J. Climate 27*, 8384–8411. https://doi.org/10.1175/JCLI-D-13-00481.1

Trömel, S. and *C.-D. Schönwiese*, 2007: Probability change of extreme precipitation observed from 1901 to 2000 in Germany. *Theor. Appl. Climatol. 87*, 29–39. https://doi.org/10.1007/s00704-005-0230-4

Unkašević, M., I. Tošić, and D. Vujović, 2004: Variability and probability of annual and extreme precipitation over Serbia and Montenegro. *Theor. Appl. Climatol. 79*, 103–109. https://doi.org/10.1007/s00704-004-0060-9

Wang, X. L., and A. Lin, 2015: An algorithm for integrating satellite precipitation estimates with in situ precipitation data on a pentad time scale. *J. Geophys. Res. Atmospheres 120*, 3728–3744. https://doi.org/10.1002/2014JD022788

Wilks, D. S., 2012: Projecting "Normals" in a Nonstationary Climate. *J. Appl Meteorol Climatol.52*, 289–302. https://doi.org/10.1175/JAMC-D-11-0267.1

Yuan, Z., Z. Yang, D. Yan, and J. Yin, 2017: Historical changes and future projection of extreme precipitation in China. *Theor. Appl. Climatol. 127*, *1*, 393-407. https://doi.org/10.1007/s00704-015-1643-3

Zhang, D., T. Wang, Y. Liu, S. Zhang, and X. Meng, 2021: Spatial and temporal characteristics of annual and seasonal precipitation variation in Shijiazhuang region, north China. *Environ. Earth Sci. 80*, *18*, 656. https://doi.org/10.1007/s12665-021-09949-0

Zhang, Q., J. Zhang, D. Yan, and Y. Wang, 2013: Extreme precipitation events identified using detrended fluctuation analysis (DFA) in Anhui, China. *Theor. Appl. Climatol. 117*, 169–174. https://doi.org/10.1007/s00704-013-0986-x

Zhang, Q., C.-Y. Xu, H. Tao, T. Jiang, and *Y.D. Chen*, 2009: Climate changes and their impacts on water resources in the arid regions: a case study of the Tarim River basin, China. *Stoch. Environ. Res. Risk Asses. 24*, 349–358. https://doi.org/10.1007/s00477-009-0324-0

Zhao, Y., X. Xu, W. Huang, Y. Wang, Y. Xu, H. Chen, and Z. Kang, 2019: Trends in observed mean and extreme precipitation within the Yellow River Basin, China. *Theor. Appl. Climatol. 136*, 1387–1396. https://doi.org/10.1007/s00704-018-2568-4

INSTRUCTIONS TO AUTHORS OF *IDŐJÁRÁS*

The purpose of the journal is to publish papers in any field of meteorology and atmosphere related scientific areas. These may be

- research papers on new results of scientific investigations,
- critical review articles summarizing the current state of art of a certain topic,
- short contributions dealing with a particular question.

Some issues contain "News" and "Book review", therefore, such contributions are also welcome. The papers must be in American English and should be checked by a native speaker if necessary.

Authors are requested to send their manuscripts to

Editor-in Chief of IDŐJÁRÁS
P.O. Box 38, H-1525 Budapest, Hungary
E-mail: journal.idojaras@met.hu

including all illustrations. MS Word format is preferred in electronic submission. Papers will then be reviewed normally by two independent referees, who remain unidentified for the author(s). The Editor-in-Chief will inform the author(s) whether or not the paper is acceptable for publication, and what modifications, if any, are necessary.

Please, follow the order given below when typing manuscripts.

Title page should consist of the title, the name(s) of the author(s), their affiliation(s) including full postal and e-mail address(es). In case of more than one author, the corresponding author must be identified.

Abstract: should contain the purpose, the applied data and methods as well as the basic conclusion(s) of the paper.

Key-words: must be included (from 5 to 10) to help to classify the topic.

Text: has to be typed in single spacing on an A4 size paper using 14 pt Times New Roman font if possible. Use of S.I. units are expected, and the use of negative exponent is preferred to fractional sign. Mathematical formulae are expected to be as simple as possible and numbered in parentheses at the right margin.

All publications cited in the text should be presented in the *list of references*, arranged in alphabetical order. For an article: name(s) of author(s) in Italics, year, title of article, name of journal, volume, number (the latter two in Italics) and pages. E.g., *Nathan, K.K.,* 1986: A note on the relationship between photosynthetically active radiation and cloud amount. *Időjárás 90,* 10–13. For a book: name(s) of author(s), year, title of the book (all in Italics except the year), publisher and place of publication. E.g., *Junge, C.E.,* 1963: *Air Chemistry and Radioactivity.* Academic Press, New York and London. Reference in the text should contain the name(s) of the author(s) in Italics and year of publication. E.g., in the case of one author: *Miller* (1989); in the case of two authors: *Gamov* and *Cleveland* (1973); and if there are more than two authors: *Smith et al.* (1990). If the name of the author cannot be fitted into the text: *(Miller,* 1989); etc. When referring papers published in the same year by the same author, letters a, b, c, etc. should follow the year of publication. DOI numbers of references should be provided if applicable.

Tables should be marked by Arabic numbers and printed in separate sheets with their numbers and legends given below them. Avoid too lengthy or complicated tables, or tables duplicating results given in other form in the manuscript (e.g., graphs). *Figures* should also be marked with Arabic numbers and printed in black and white or color (under special arrangement) in separate sheets with their numbers and captions given below them. JPG, TIF, GIF, BMP or PNG formats should be used for electronic artwork submission.

More information for authors is available: journal.idojaras@met.hu

Published by the HungaroMet Hungarian Meteorological Service

Budapest, Hungary

ISSN 0324-6329 (Print)

ISSN 2677-187X (Online)